THE CHEMISTRY OF MoS_2 AND RELATED COMPOUNDS AND THEIR APPLICATIONS IN ELECTROCATALYSIS AND PHOTOELECTROCHEMISTRY

by

QI DING

A dissertation submitted in partial fulfillment of

the requirements for the degree of

DOCTOR OF PHILOSOPHY

(CHEMISTRY)

at the

UNIVERSITY OF WISCONSIN–MADISON

2016

Date of final oral examination: May 17th, 2016

The dissertation is approved by the following members of the Final Oral Committee:

Song Jin, Professor – Chemistry
Robert J. Hamers, Professor – Chemistry
John C. Wright, Professor – Chemistry
Michael S. Arnold, Associate Professor – Materials Science and Engineering
Kyoung-Shin Choi, Professor – Chemistry

PREFACE

THE CHEMISTRY OF MoS_2 AND RELATED COMPOUNDS AND THEIR APPLICATIONS IN ELECTROCATALYSIS AND PHOTOELECTROCHEMISTRY

QI DING, PH. D.

UNIVERSITY OF WISCONSIN–MADISON

2016

The increasing energy demand in our society has stimulated intensive research in the development of sustainable and renewable energy sources to lessen our strong dependence on fossil fuels. Hydrogen is a clean, storable, and high-energy density energy carrier, and is a promising sustainable solution to achieve an environmentally friendly fuel economy. Electrochemical and solar-driven photoelectrochemical water splitting is regarded as one of the most promising approaches to utilize renewable energy to product hydrogen fuel, yet Pt and other noble metals remain the best electrocatalysts for hydrogen evolution reaction (HER), the high cost of which ultimately limit the scalability of such technologies.

Layered transition metal dichalcogenides (TMDCs) is a family of compounds that has attracted widespread attention due to their broad range of applications in electronic devices, optoelectronics, sensing, energy storage, and catalysis. Owing to its relatively low cost, earth abundance, and high catalytic activity and good stability towards HER, TMDCs are now being regarded as promising potential alternatives to Pt for HER catalysis. My research has primarily focused on understanding the chemistry of MoS_2 and related compounds, and developing rational approaches to enable these materials for efficient electrocatalytic and photoelectrochemical (PEC) hydrogen evolution.

Chapter 1 serves as a general introduction to the basic concepts of the electrocatalytic and photoelectrochemical hydrogen evolution reactions. I discuss various approaches to improve the catalytic activity of MoS_2 and related compounds for HER, and highlight the state-of-the-art experimental discoveries. I also review the development of integrated photoelectrochemical (PEC) systems where MoS_2 is combined with semiconductors to enable direct solar-to-fuel conversion, and offer perspective on how to design efficient integrated photoelectrochemical (PEC) systems, in hopes of lighting a path toward achieving performance competitive with their noble metal-containing analogues.

Chapter 2 follows up on the groundwork laid in Chapter 1 and demonstrates highly efficient and robust photocathodes based on heterostructures of chemically exfoliated metallic 1T-MoS_2 and planar *p*-type Si for solar-driven hydrogen production. Photocurrents up to 17.6 mA/cm^2 at 0 V *vs* reversible hydrogen electrode (RHE) were achieved under simulated 1 sun irradiation, and excellent stability was demonstrated over long-term operation. Electrochemical impedance spectroscopy revealed low charge transfer resistances at the semiconductor/catalyst and catalyst/electrolyte interfaces, and surface photoresponse measurements also demonstrated slow carrier recombination dynamics and consequently efficient charge carrier separation, providing further evidences for the superior performance. The results suggest that chemically exfoliated 1T-MoS_2/Si heterostructures are promising earth-abundant alternatives to photocathodes based on noble metal catalysts for solar-driven hydrogen production.

Building upon the 1T-MoS_2 groundwork, I seek to further enhance the PEC performance by understanding and improving the critical components in photocathode systems. In chapter 3, I replace p-type planar Si with n^+pp^+ Si micropyramids (MPs), which largely enhanced the photovoltage and the light harvesting ability. On the catalyst side, MoQ_xCl_y (Q = S, Se) catalysts are developed to be comparable catalysts to 1T-MoS_2, and the preparation of MoQ_xCl_y does not require chemical exfoliation and high temperature synthesis. Moreover, MoS_xCl_y is a catalyst that has little light absorption in the visible and near infrared range. This rather unusual characteristic, combined with its high electrocatalytic activity, make it a unique and highly competitive catalyst material for PEC-HER. By integrating MoQ_xCl_y catalysts with n^+pp^+ Si MPs, I successfully fabricated efficient photocathodes with significantly enhanced onset potential and fill factor, and most importantly, the highest current density ever reported for Si-based photocathodes.

After demonstrating the great potential of utilizing MoS_2 and related compounds for hydrogen evolution reaction, I seek to fully harness the potentials of MoS_2 and utilize it for a broader range of applications. Functionalization is an essential approach to further alter the electronic, optical and catalytic properties of MoS_2. Despite the general belief that the basal plane of 2H-MoS_2 monolayer is too inert for functionalization, in chapter 5, I demonstrate the basal plane can be covalently functionalized via thiol conjugation. Sulfur vacancies on MoS_2 ML basal plane are demonstrated to play a key role in the thiol conjugation. By controlling the amount of sulfur vacancies, the degree of MoS_2 functionalization can be effectively adjusted. This thiol conjugation also partially repairs or passivates sulfur vacancies, leading to enhanced photoluminescence response and decreased active sites for hydrogen evolution reaction catalysis. Moreover, such functionalization also offered possibilities for the formation of MoS_2-based heterostructures, an example of which used a dithiol molecule to link MoS_2 ML and PbSe quantum dots heterostructures, opening up opportunities for broader applications in solar and optoelectronic devices.

Lastly, I report a facile approach to synthesize epitaxial PbSe–TiO_2 quantum dot nanoscale heterostructures (QDH) for solar energy conversion. Quantum dot nanoscale heterostructures (QDHs) are a class of materials that are useful for both fundamental investigation of charge transfer and potentially useful for integration into solar energy conversion devices. I synthesized the heterostructure using a hot injection approach with a home-designed setup, yielding PbSe QDs with excellent coverage and narrow size distribution. High resolution transmission electron microscopy (HRTEM) confirmed the direct lattice connection between PbSe QDs and TiO_2 nanomaterials, and a supercell was designed to calculate the lattice mismatch across the interface. Moreover, I demonstrated this approach could be readily extended to TiO_2 with different morphologies (nanoparticles, nanosheets, nanorods), on different substrates (FTO, titanium foil, glass), and even on other metal oxide semiconductors, such as SnO_2. Enhanced absorption spectrum was observed due to the light absorption of PbSe QDs, and fast charge transfer kinetics from the donor to the acceptor materials is expected because of the direct lattice connection in the epitaxial heterostructure.

The body of work presented here represents substantial progress toward the understanding of MoS_2 chemistry and the development of utilizing it for renewable energy applications. By engineering the phase and developing ternary compounds, efficient electrocatalytic and photoelectrochemical HER systems have been successfully demonstrated, offering simple strategies for improving the performance of a wide variety of earth-abundant inorganic electrocatalyst materials. Additionally, I have shown successful covalent functionalization on

MoS_2 basal plane, opening up more opportunities in the development of electronic, optoelectronic and solar applications.

ACKNOWLEDGEMENTS

I would like to express my warmest gratitude to all those who helped me in the completion of this wonderful journey.

Most importantly, I must thank my parents Zeming Ding and Yanjing Wang for their unconditional love and support. You have created the most supportive and loving family that I could possibly ever ask for, and I am so happy and blessed to be your daughter. You are always there loving me and supporting me through the ups and downs in life, and give me the strength and encouragement to carry on whenever I needed it. I truly wouldn't be who I am today, if not for your love and encouragement. I also want to give special thanks to my cousin, Xiaolong Wang, for being the best sibling ever. Thank you for always believing in me and being endless sources of support in my life.

I want to express my deepest gratitude to my PhD advisor, Prof. Song Jin, a person who is always energetic, enthusiastic, curious, and never lacks creative ideas. You shaped me to who I am today as a scientist and I have learned tremendously from you. I greatly appreciate the freedom you provided to me in exploring various projects, which largely broadened my knowledge and skill sets and allowed me to find what I am mostly interested in, and also opened up more opportunities for me in different industry fields. You taught me to be independent and professional, and I feel I am well prepared to move on to the next chapter of my career because of your training.

I must also thank my undergraduate research advisors, Prof. Aixin Song, for getting me started on this scientific journey and preparing me for graduate school. I will forever be grateful for your guidance and kindness. I really appreciate and treasure everything you have taught me. I want to give my special thanks to Prof. Limin Qi, my advisor during my exchange in Peking University. I am so thankful for your support and how much you believed in my potential. You have inspired me to pursue my goals with hard work and dedication. Without your guidance and support, I wouldn’t be where I am here today. I also want to explicitly thank my high school math teacher, Mr. Ronghua Zhang. Your encouragement and belief in me had played a big part in my life.

I also owe an enormous amount of thanks to my wonderful supervisor at 3M during my internship in 2015 summer, Dr. Kari McGee. You have been an amazing supervisor and offered me tremendous amount of support, guidance and encouragement. You opened my eyes to new stage of opportunity and strength. I also owe an especially large debt of gratitude to Dr. Jeremy Higgins, who helped me get this internship position and provided enormous amount of help and guidance over the summer. Kari and Jeremy, you two set such excellent examples for me as successful and professional scientists in industry, and I have leant so much from you guys, more than you realize, both professionally and personally. Although three months passed by very fast, it was amazingly positive and influential. I cannot express how grateful I am for this wonderful opportunity to work together with you two.

I have always been very proud to be a member of the Jin Group, thanks to my current and former lab-mates who have made my time in UW-Madison so memorable. I give my special thanks to Dr. Fei Meng, who helped me extraordinarily during my PhD and helped me get started with my research project. I am grateful to have two awesome classmates, Leith Samad and Nick Kaiser, who are incredibly nice, supportive, and fun to be with. I want to thank Dr. Dong Liang for being a great mentor and great friend, thank Dr. Audrey Forticaux, Dr. Ankit Pokhrel for always encouraging me to be a strong and independent woman, and thank Dr. Steven Girard for always reminding me there is a lot more to life than just work. I want to thank the people I have collaborated with, Dr. Xingwang Zhang, Dr. Rachel Selinsky, Dr. Mark Lukowski, Dr. Matthew Faber, Dr. Caroline English, Dr. Miguel Caban-Acevedo, Melinda Shearer, Yongping Fu, Kyle Czech, Andrew Daniels, Linsen Li, Junqiao Zhuo, Hanfeng Liang for being great partners and being endless sources of inspiration through my graduate studies. I want to express my appreciation to other people in the Jin Group that I have been closely working with, Dr. Leekyoung, Dr. Marc Estruga, Dr. Tania Guardado, Salih Hacialioglu, Lichen Xiu, Matthew Stolt, Lianna Dang, Wenjie Li, Yuzhou Zhao, Matthew Haveman, Nitish Mathur, Jun Dai, Jie Chen, Yifan Dong, Xiaohua Yang, Yang Yang, Yi Zhang, Mickey Stone. Thank you for being wonderful friends and making this journey so much fun. I owe a special debt of gratitude to Professor Robert Hamers and Professor John Wright, who have both been amazing sources of fresh ideas and encouragement. I also want to express my gratitude to Dr. Rob McClain, Dr. Arrietta Clauss, Dr. Alex Kvit, who all keep this university running. While pursuing my PhD, I had the privilege of mentoring many students. I’d like to thank Cecilia Gentle, Sanghun Shin, Triston Abbott for working with me and being excellent undergraduate researchers. I would also like especially thank Jianyuan (Jackie) Zhai, an outstanding undergraduate who have worked with me for two of my publications, who I am sure will have a bright future ahead.

Finally, I thank my closest friends who have made my time in Wisconsin truly memorable. I want to thank fellow graduate students, Shuyu Fang, Qiyao Li, Daniel Kohler, Blaise Thompson and Kelly Hebert for going through the ups and downs with me in graduate school together. I wish you all the best luck in the future. I also wish to thank my closest friends in Madison, Bingqing Cai, Bozhao Qi, Yue Qiu, Haiyun Jin, Xiaomeng Lu, and every member in our “graduate soon” volleyball team, Xing Wang, Bin Guo, Zhewen Xu, Shuo Li, Jianqiao Zhu, Weiwei Hu, Kaiyue

Zheng, Xiaoping Bao, Yixuan Feng, Huilong Zhang, Nongyi Cheng and Dongrui Zhao. Some of the best memories of my time here were forged during our time spent together. You guys are, and always will be, family to me.

And lastly, I'd like to thank you, kind reader, for taking the time to recognize this list of people important to me.

– Qi Ding, 05/08/2016

TABLE OF CONTENTS

CHAPTER 1 EFFICIENT ELECTROCATALYTIC AND PHOTOELECTROCHEMICAL HYDROGEN GENERATION USING MOLYBDENUM SULFIDE AND RELATED COMPOUNDS

CHAPTER 2 EFFICIENT PHOTOELECTROCHEMICAL HYDROGEN GENERATION USING HETEROSTRUCTURES OF Si AND CHEMICALLY EXFOLIATED METALLIC MoS_2

CHAPTER 3 EFFICIENT SOLAR-DRIVEN HYDROGEN EVOLUTION PHOTOCATHODES USING SEMI-TRANSPARENT MoQ_XCl_Y (Q=S, Se) CATALYSTS ON Si MICROPYRAMIDS

CHAPTER 4 BASAL PLANE LIGAND FUNCTIONALIZATION ON SEMICONDUCTING 2H-MoS_2 MONOLAYERS

CHAPTER 5 SYNTHESIS AND PROPERTIES OF EPITAXIAL PbSe QD-TiO_2 NANOSCALE HETEROSTRUCTURES FOR SOLAR ENERGY CONVERSION

APPENDIX 1 SUPPORTING INFORMATION FOR CHAPTER 2

APPENDIX 2 SUPPORTING INFORMATION FOR CHAPTER 3

APPENDIX 3 SUPPORTING INFORMATION FOR CHAPTER 4

LIST OF FIGURES

LIST OF TABLES

Chapter 1

Efficient Electrocatalytic and Photoelectrochemical Hydrogen Generation Using Molybdenum Sulfide and Related Compounds

1.1 Introduction

The increasing energy demand in our society has stimulated intensive research in the development of sustainable and renewable energy sources to lessen our strong dependence on fossil fuels.[1] Hydrogen is a clean energy carrier that can be stored, distributed, and used on demand.[2,3] In comparison with carbon-based fossil fuels that produce greenhouse gases, the combustion of hydrogen produces water as the only byproduct. Today, hydrogen is mainly produced via steam methane reforming of natural gas, during which process, CO_2 is produced. In the pursuit of a secure and clean future of hydrogen economy, sustainable hydrogen production must be developed. Electrochemical and solar-driven photoelectrochemical water splitting is regarded as one of the most promising approaches to utilize renewable energy to product hydrogen fuel.[4-6]

To maximize the efficiency of such transformations, catalysts are commonly employed to facilitate both charge transfer and subsequent chemical reaction, accelerating their respective rates. However, Pt and other noble metals are still the best electrocatalysts for hydrogen evolution reaction (HER).[7] Their high cost and scarcity greatly limit their large scale deployment. Therefore, developing low-cost and earth-abundant catalysts that could demonstrate comparable performance with that of Pt group metals is highly desired. In the past decade, significant progress has been made in the exploration of new earth-abundant, inexpensive, and nontoxic catalysts for HER, including metal alloys, chalcogenides, nitrides, phosphides, borides, and carbides.[8-14] Among these materials, two-dimensional (2D) layered transition metal dichalcogenide materials have received great attention due to their unique crystal structures, unusual properties, and great promise in HER catalysis. Even though by now this family might not have the best HER performance than some other families of materials, such as metal phosphide and phosphosulphide,[14] this is perhaps the first earth-abundant compound studied for HER catalyst, and its mechanism is well understood and offers valuable insights for the development of new catalysts.

In this review, we will focus our attention on two-dimensional molybdenum disulfide and related compounds as potential replacements of Pt for HER catalysis and photoelectrochemical (PEC) water splitting. After introducing the background, we discuss several important approaches that have been demonstrated to improve the catalytic activity of MoS_2 for HER, and highlight the state-of-the-art experimental discoveries. We also review the development of combining MoS_2 with semiconductors for integrated PEC systems for direct solar-to-fuel conversion, and provide insights regarding how to design the most efficient PEC-HER system. Because of the rapid development in this emerging field, we cannot ensure that this review encompasses the full body of related work; instead, we seek to highlight the key discoveries that have improved the fundamental understanding and influenced the research direction of the field.

1.2 Electrocatalytic Hydrogen Evolution

1.2.1 Hydrogen evolution mechanism

The water splitting reaction can be divided into two half-reactions: the water oxidation reaction (or oxygen evolution reaction, OER) and the water reduction reaction (or hydrogen evolution reaction, HER).

$$H_2O \rightarrow H_2 + \frac{1}{2}O_2 \qquad (1)$$

Depending on the reaction condition, the reaction can be expressed in different ways.

a) In acidic solution:

Cathode

$$2H^+ + 2e^- \rightarrow H_2 \qquad (2)$$

Anode

$$H_2O \rightarrow 2H^+ + \frac{1}{2}O_2 + 2e^- \qquad (3)$$

b) In neutral and alkaline solutions:

Cathode

$$2H_2O + 2e^- \rightarrow H_2 + 2OH^- \qquad (4)$$

Anode

$$2OH^- \rightarrow H_2O + \frac{1}{2}O_2 + 2e^- \qquad (5)$$

At standard conditions, an energy input of $\Delta G = 237.1$ kJ/mol is required to achieve electrochemical water splitting, which corresponds to a thermodynamic electrochemical potential of 1.23 V. Ideally, an external potential of 1.23 V is sufficient to split water in an electrochemical cell. However, overpotentials are present because of the large kinetic barriers originated from the high activation energies required for the formation of reaction intermediates on electrode surface. Thus, in practice, potential much larger than 1.23 V is required for sufficient water splitting.

The voltage (E_{op}) for water splitting can be described as:[15]

$$E_{op} = 1.23\ V + \eta_a + \eta_c + \eta_{other} \quad (6)$$

Where 1.23 V is the thermodynamic potential value for water splitting, η_a and η_c represent the total overpotentials (the potential difference between thermodynamically determined potential and the experimental potential) at the anode and cathode side, respectively, and η_{other} is the voltage drop from other resistances in the electrochemical cell, including solution resistance, membrane resistance, and contact resistance, etc. In order to reduce the cell voltage, the overpotential at the electrodes and in the electrochemical cell should be reduced. The voltage drop in η_{other} can be reduced by carefully designing the electrochemical cell to reduce the solution and contact resistance. And the overpotential at the electrodes could be minimized by choosing efficient catalysts for hydrogen evolution and oxygen evolution.

The mechanism of hydrogen evolution reaction (HER)[16] in acidic environment is illustrated in Figure 1.1a. HER typically involves three steps shown in the arrows. The first one is called Volmer or discharge reaction step.

$$H^+(aq) + e^- + * \rightarrow H^*_{ads} \quad (7)$$

This is the reaction of a transferred electron reacting with a proton, generating an adsorbed hydrogen atom (H^*_{ads}) on the electrode surface. Then, the reaction could either proceed via the Tafel reaction or the Heyrovsky reaction. In the Tafel reaction, two absorbed hydrogen atoms combine to generate H_2 gas.

$$2H^*_{ads} \rightarrow H_2\ (g) + 2\, * \quad (8)$$

Whereas in the Heyrovsky reaction, another electron would react with adsorbed hydrogen atom and another proton from the solution to yield H_2.

$$H^*_{ads} + H^+(aq) + e^- \rightarrow H_2\ (g) + * \quad (9)$$

1.2.2 Important parameters in HER catalysis

Regardless of the reaction mechanism, adsorbed hydrogen intermediate is always generated in the first Volmer reaction and is often the rate limiting step for many non-precious metal catalysts. Thus, the Gibbs free energy for hydrogen adsorption (ΔG_{H*}) in Volmer reaction has been regarded as a good descriptor for HER catalytic activity.[17-19] Density functional theory (DFT) can be used to calculate the free energy of hydrogen binding in theoretical prediction, and provide insight about the catalytic activity of a material. Sabatier plot (so-called volcano plot) summarizes the relationship between the exchange current density and hydrogen adsorption energy (ΔG_{H*}) for most metals. As shown in Figure 1.1b, the most active catalysts for HER are at the summit of the volcano plot, with a nearly zero ΔG_{H*} and the highest exchange current density. Pt group metals have an ΔG_{H*} close to zero, therefore are the best hydrogen evolution catalysts. Metals on the left bind too strongly, making the initial Volmer step easy. But they also hold onto the adsorbed proton too strongly and affect the subsequent Tafel or Heyrovsky steps. Metals on the right bind too weakly, requiring a large driving force to initiate the Volmer reaction and limit the overall turnover rate. Therefore, a nearly zero ΔG_{H*} is desired for choosing non-Pt HER catalysts.

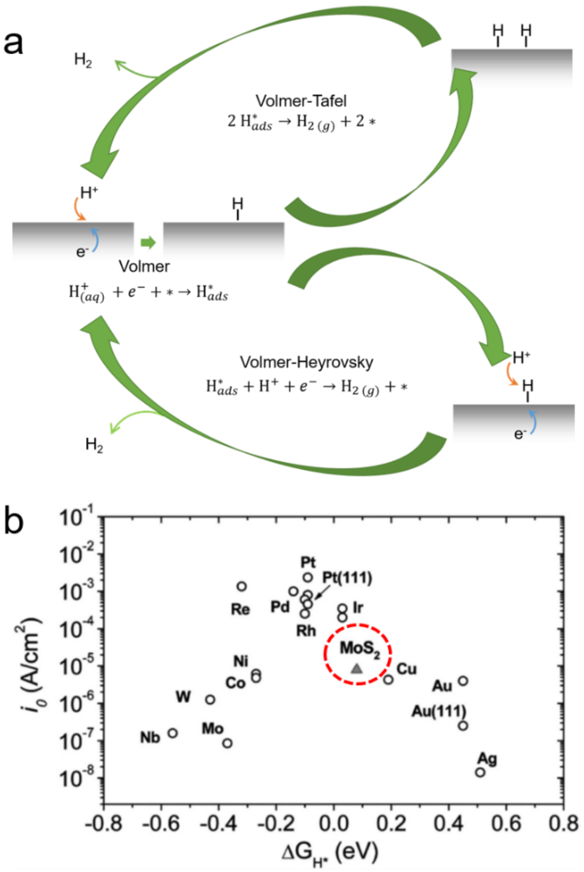

Figure 1.1. (a) The mechanism of hydrogen evolution on the surface of an electrode in acidic solutions. (b) The Sabatier plot for HER catalysts showing the exchange current densities plotted against the free energy of hydrogen adsorption. Materials near the top of the volcano curve are expected to be most active in HER.[20]

Tafel slope is another parameter that is characteristic of the HER catalytic activity. It reveals the relationship between the current density (j) and the overpotential (η). Exchange current density (j_0) is a parameter that is correlated to the electron transfer rate of the catalyst under reversible conditions, with a larger j_0 reflecting faster kinetics toward the redox reaction. As shown in equation (10), j is the current density, j_0 is the exchange current density, R is the ideal gas constant, T is the absolute temperature, a is the electrochemical transfer coefficient, n is the number of electrons involved in the electrode reaction, and F is the Faraday constant. Tafel slope is defined using $b = \frac{2.3RT}{\alpha nF}$, in the unit of mV decade^{-1}.

$$|\eta| = \frac{2.3RT}{\alpha nF} log \frac{J}{J_0} \qquad (10)$$

The linear part of the Tafel plot is fit to the equation, where both the Tafel slope (b) and the exchange current density (j_0) can be derived. Both values are important parameters in electrocatalysis. The value of b indicates the catalytic mechanism of the electrode reaction, and exchange current density j_0 reflects the intrinsic catalytic activity of the electrode material under equilibrium conditions. In order to minimize the value of overpotential, ideal catalysts should have a high exchange current densities (j_0) and a small Tafel slope (b). Other parameters that are commonly used to compare between different catalysts include onset potential, the potential at which HER activity begins, and the potential required to reach 10mA/cm^2.

1.3 Utilizing MoS_2 and Related Compounds as HER Catalysts

Layered transition metal dichalcogenides (TMDCs) is a family of compounds that has attracted widespread attention due to their broad range of applications in electronic devices, optoelectronics, sensing, energy storage, and catalysis.[21-24] They are traditionally used as industrial hydrodesulfurization catalysts,[3] and recently have been explored as exciting HER catalysts that exhibit excellent catalytic activity. Due to their relatively low cost, earth abundance, high catalytic activity and good stability, they are regarded as promising potential alternatives to Pt for HER catalysis.

1.3.1 Crystal structures of MX_2 materials

The layered transition metal dichalcogenides have the general formula of MX_2, where M is a transition metal (Ti, Zr, Hf, V, Nb, Ta, Mo, W, Re, etc.), and X is a chalcogen (S, Se, Te). Individual sandwiched X-M-X layers are held together by weak van der Waals interactions to form hexagonal structures. MoS_2 has been one of the most well studied TMDCs and acts as an excellent model system to explore the chemistry of 2D TMDCs. It exhibits three polymorphs, 2H, 3R and 1T (Figure 1.2), and subtle structural changes can dramatically affect electrical properties. Natural MoS_2 is found to be the thermodynamically favored 2H phase with S-Mo-S layers built from edge-sharing MoS_6 trigonal prisms. It has two layers per unit cell stacked in the hexagonal symmetry. 3R-MoS_2 shares the same crystal structure with 2H in each single layer, but has three layers per cell stacked in the rhombohedral symmetry. 1T is not naturally found in bulk, and could be obtained by chemical exfoliation from 2H via n-Butyl lithium treatment. It has one layer per unit cell, in which the coordination of Mo atoms becomes octahedral instead of the trigonal prisms shown in 2H and 3R. Unlike the semiconducting nature of 2H, 1T-MoS_2 is found to be metallic. Because of the metastable nature of 1T-MoS_2, it could readily transform back to 2H phase under high-temperature annealing.

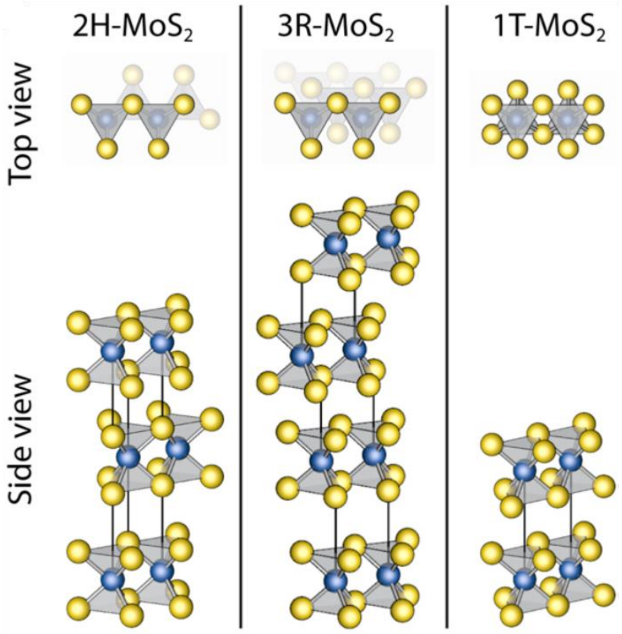

Figure 1.2. Crystal structure of the 2H, 3R, and 1T polytypes of MoS_2.[10]

Semiconducting MoS_2 also has unique layer-dependent properties. Generally, each layer has a thickness of ~0.65 nm. Unusual optical and electronic properties emerge when bulk MoS_2 is thinned to a single layer, making MoS_2 monolayers (MLs) particularly attractive. Photoluminescence (PL) is observed in MoS_2 monolayers due to the transition from indirect band gap (1.3 eV) to direct band gap (1.8 eV),[25] which generates possibilities for many optoelectronic applications such as light-emitting diodes and photodetectors.[26-29] Field effect transistors (FETs) based on MoS_2 monolayers were demonstrated to have high mobilities and on−off current ratios up to 1×10^8.[30]

1.3.2 Approaches to enhance MoS_2 catalytic activity and performance

Early work on bulk MoS_2 suggested that this material is not a particularly active HER catalyst.[31] Nevertheless, since the early theoretical work,[18] various approaches have been developed in recent years to significantly enhance its HER catalytic activity, making it a promising HER catalyst. Here we will describe the approaches that have been demonstrated to be effective in improving the catalytic activity and overall HER performance of MoS_2: (1) increase active sites, (2) phase engineering, (3) coupling with conductive scaffolds, (4) amorphous molybdenum sulfide, and (5) amorphous ternary compounds.

1.3.2.1 Increase active sites

a) Increase edge sites

Both experimental[20] and computational[18] studies have demonstrated that the edge sites of MoS_2 possess very different chemical reactivity with the basal plane. DFT calculations showed the theoretical free energy of adsorption of hydrogen on the edge sites of MoS_2 is close to that of Pt, raising the possibility of MoS_2 as a promising HER electrocatalyst.[18] Direct measurement using scanning tunneling microscopy (STM) also showed the edges of MoS_2 nanoplatelets appear as bright rims, suggesting their more catalytically active nature (Figure 1.3). Moreover, electrocatalytic activity measurements showed that the catalytic performance of MoS_2 nanoparticles is proportional to the edge state length, rather than the area coverage, directly establishing the relationship between MoS_2 edges and the catalytic active sites.[20]

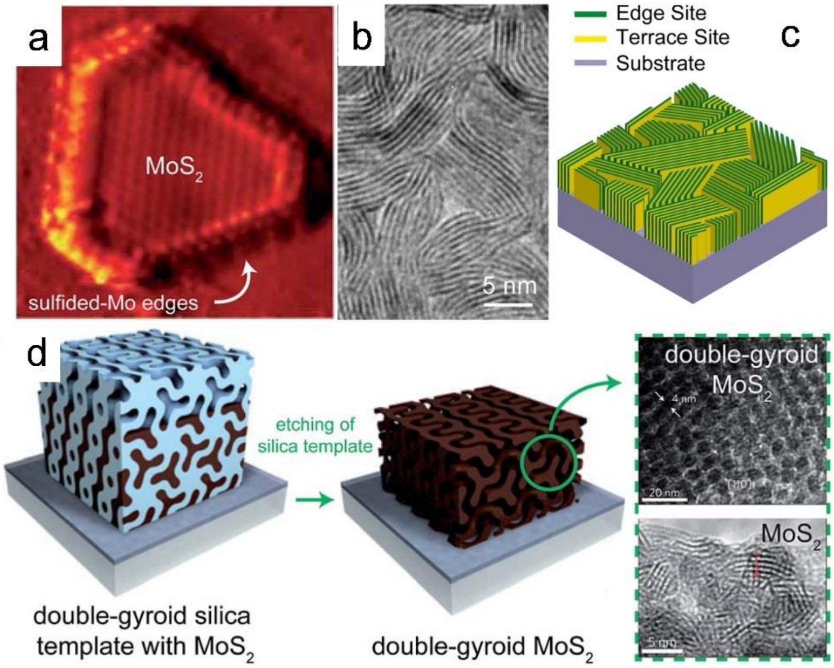

Figure 1.3. (a) Atomically-resolved scanning tunneling microscopy (STM) image of a MoS_2 nanoplates on Au [111] showing the bright rim around the edges, corresponding to the catalytically active edge sites.[20] (b) TEM image of a MoS_2 film produced by rapid sulfurization. (c) Idealized structure of edge-terminated molybdenum chalcogenide films with the layers aligned perpendicular to the substrate, maximally exposing the edges of the layers.[32] (d) Abbreviated scheme for the synthesis of double-gyroid mesoporous MoS_2 engineered to preferentially expose edge sites for enhanced HER activity.[33]

Motivated by the higher catalytic activity along the edge sites of MoS_2, nanostructured MoS_2 has been actively pursued to maximally expose energetic active sites, such as nanoparticles, vertical nanoflakes, nanowires, defect-rich films, and mesoporous films. Kong et al. presented a synthesis process to grow MoS_2 and $MoSe_2$ thin films with vertically aligned layers, maximally exposing the edges on the film surface, and correlated the HER catalytic activity directly with the density of exposed edge sites (Figure 1.3b, c).[32] Similarly, single-crystal MoS_2 nanobelts with basal plane vertical to the substrate and edge sites covering the top surface were synthesized, exhibiting high electrocatalytic hydrogen evolution efficiency.[34] Kibsgaard et al used an elaborate scheme to engineer the surface structure of MoS_2 to preferentially expose edge sites to improve its activity.[33] They synthesized contiguous large-area thin films of a highly ordered double-gyroid MoS_2 bicontinuous network with nanoscaled pores (Figure 1.3d). This high surface area material preferentially exposed a large fraction of edge sites, leading to improved HER catalytic performance. However, in the meantime, increased electron transport resistance was also observed at thicker films due to the semiconducting nature of MoS_2, limiting the overall electrochemical performance at higher current densities. Xie et al reported synthesizing ultrathin MoS_2 nanosheets with rich defects, which resulted in partial cracking of the catalytically inert basal planes, exposing additional active edge sites and leading to largely improved catalytic activity.[35] In another study, Chung et al. prepared edge-exposed MoS_2 nanosheet-assembled structures and revealed the linear relationship between exchange current density and the number of sulfur edges, demonstrating that the active site for HER was the sulfur edge of MoS_2 nanosheets.[36] Saadi et al. also demonstrated an operando synthesis of $MoSe_2$ thin films for HER catalysis. During voltammetric cycling, catalytically inactive components of a $MoSe_3/MoO_3$ film were reductively converted to $MoSe_2$, generating an amorphous, macroporous $MoSe_2$ framework that exhibits enhanced HER catalytic activity.[37]

b) *Increase defects on basal plane*

The basal plane of 2H-MoS_2 is generally believed to be inert towards HER, but its coordination is not perfect. Both experimental and computational studies have shown that a wide range of defect types are present and high densities of sulfur vacancies are observed on the basal plane of CVD grown or exfoliated 2H-MoS_2.[38-40] While many research has been focused on maximizing and optimizing the active edge sites, there are also reports exploring the activation and optimization of MoS_2 basal plane. First principles calculations were used to investigate the basal plane of defected two-dimensional materials MoX_2 (X = O, S, Se) for HER, and showed that the defected MoX_2 can adsorb hydrogen atoms at defect sites, with appropriate adsorption energies for hydrogen evolution. Adatoms (several first-row transition metals, B, C, N, O) were further used to tune the reaction and it was found that C and O adatoms can make defected MoX_2 ideal for HER at higher defect levels.[41]

Li et al. reported activating the basal plane of monolayer 2H-MoS_2 by introducing sulfur vacancies and strain (Figure 1.4).[42] Their theoretical and experimental results show that the S-vacancies are catalytic sites in the basal plane, where gap states around the Fermi level allow hydrogen to bind directly to exposed Mo atoms. By manipulating the combination of S-vacancy and strain, the hydrogen adsorption free energy and catalytic activity of MoS_2 could be effectively fine-tuned. To understand the HER kinetics of those S vacancies and the additional effects from elastic tensile strain, scanning electrochemical microscopy was used to compare between unstrained S vacancies and strained S vacancies on the basal plane of MoS_2 monolayers. As a result, 4 times enhancement in the electron-transfer rate was revealed for strained S vacancies.[43]

Along the same line, Xie et al. reported using controllable disorder engineering and simultaneous oxygen incorporation in MoS_2 catalysts to enhance HER activity.[44] The disordered structure can offer abundant unsaturated sulfur atoms as active sites for HER, while the oxygen incorporation can effectively regulate the electronic structure and further improve the intrinsic conductivity. As a result, an optimized MoS_2 catalyst with an onset overpotential of 120 mV and good stability was demonstrated.

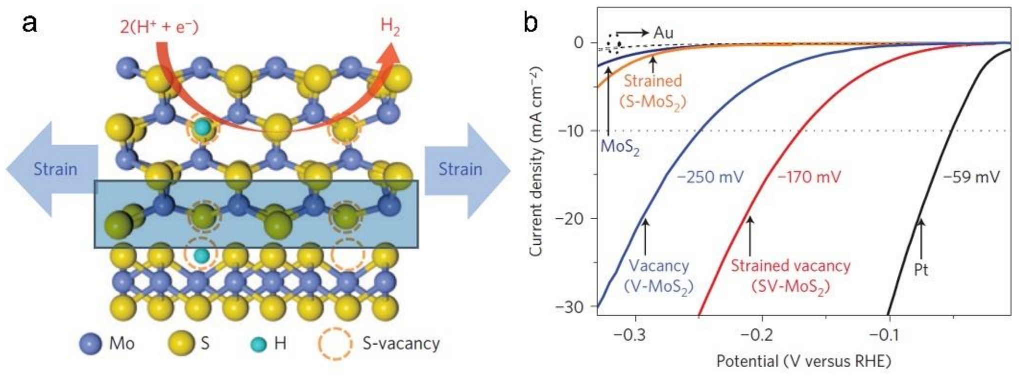

Figure 1.4. (a) Schematic of the top (upper panel) and side (lower panel) views of MoS_2 with strained S-vacancies on the basal plane, where S-vacancies serve as the active sites for hydrogen evolution and applied strain further tunes the HER activity. (b) LSV curves for the Au substrate, Pt electrode, and MoS_2 with different amount of strain and S-vacancies.[42]

1.3.2.2 Phase engineering

Besides increasing the number of active sites in MoS_2, enhanced HER catalytic activity could also be achieved via phase engineering. The as-grown 2H-MoS_2 could be converted to 1T-MoS_2 via chemical exfoliation using n-Butyl lithium, with lithium intercalated to form Li_xMoS_2 first and then exfoliated through hydration to form 1T-MoS_2. Lukowski et al. reported dramatically enhanced HER catalysis from metallic nanosheets of 1T-MoS_2 chemically exfoliated from semiconducting 2H-MoS_2 nanostructures grown directly on graphite (Figure 1.5a, b).[45] An electrocatalytic current density of 10 mA/cm^2 was achieved at an overpotential of –187 mV vs. RHE with a small Tafel slope of 43 mV/decade. Structural characterization and electrochemical studies confirmed that the metallic 1T-MoS_2 nanosheets exhibit facile electrode kinetics, low-loss electrical transport, and possess a proliferated density of catalytic active sites, which result in such dramatic enhancement in performance.[45] Voiry et al. further showed that the active sites of 1T-MoS_2 are no longer limited to the edges like in 2H phase, but mainly located in the basal plane.[46] By utilizing different organolithium compounds for intercalation, Ambrosi et al also demonstrated the degrees of exfoliation and HER catalytic activity are also affected by the intercalator, with n-butyllithium and tert-butyllithium providing higher degrees of exfoliation and better HER catalytic properties than methyllithium.[47] Moreover, Wang et al demonstrated the continuous tuning of vertically aligned MoS_2 nanofilms through electrochemical intercalation of Li^+ ions, which enabled continuous tuning of the oxidation state of Mo, the transition of semiconducting 2H to metallic 1T phase, and also demonstrated significantly improved HER catalytic activity (Figure 1.5c).[48] These distinct and previously unexploited features of 1T-MoS_2 make these metallic nanosheets a highly competitive earth-abundant HER catalyst.

Similar to 1T-MoS_2, 1T-WS_2 nanosheets have also been reported to display excellent catalytic activity for hydrogen evolution reaction (HER). Metallic 1T-WS_2 nanosheets can be prepared from CVD grown 2H-WS_2 using microwave-assisted n-butyl lithium intercalation method. Structural and electrochemical studies confirm that the simultaneous conversion and exfoliation of semiconducting 2H-WS_2 into nanosheets of its metallic 1T polymorph result in facile electrode kinetics, excellent electrical transport, and proliferation of catalytically active sites.[49] Pumera's group further examined the inherent electroactivities of other chemically exfoliated $MoSe_2$, WS_2, WSe_2, and their catalytic activity towards hydrogen evolution and oxygen reduction reactions, and demonstrated strong dependence of catalytic activity on the chemical exfoliation route and metal-to-chalcogen composition.[50,51]

Density functional theory (DFT) has been utilized to provide deeper understanding of the catalytic activity of 1T- and 2H-MoS_2.[52-54] Gao et al. reported that the negative charges on 1T-MoS_2 helped to reduce the kinetic energy barrier for the transition from 2H to 1T, and the 1T phase would transform into the distorted structure (1T′ phase) spontaneously. The catalytic activity for 1T′-MoS_2 is comparable to that of 2H, but the faster charge transfer kinetics helped to provide the superior performance.[52]

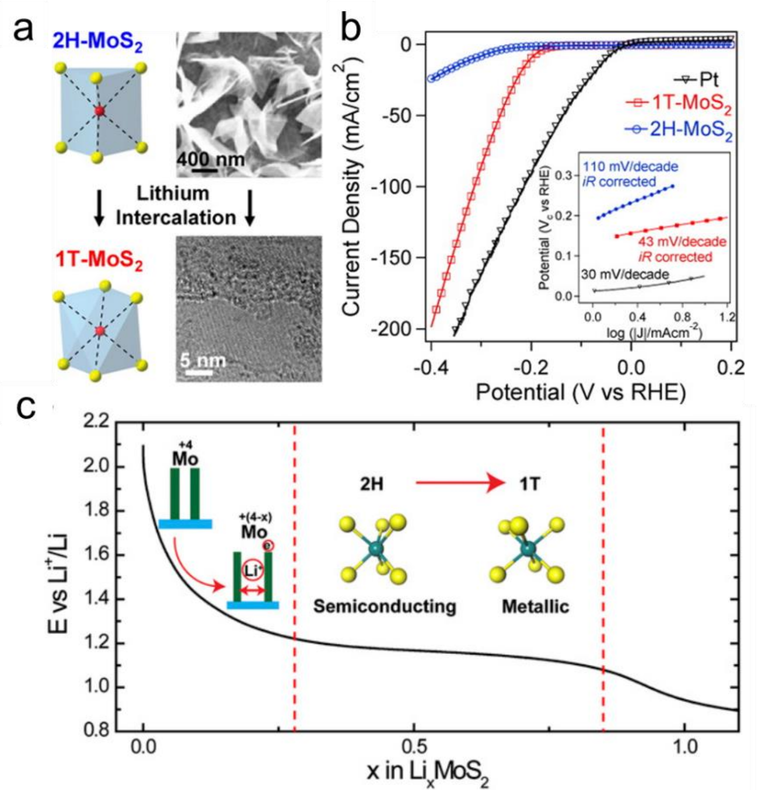

Figure 1.5. (a) Phase conversion from semiconducting 2H-MoS$_2$ to 1T-MoS$_2$ after lithium intercalation. (b) Polarization curves showing enhancement of the electrocatalytic activity toward HER through chemical exfoliation and phase transitions.[45] (c) Galvanostatic discharge curve representing the lithiation process. Li intercalates into the van der Waals gaps of MoS$_2$ to donate electrons to the slabs and expand the layer spacing. The voltage monotonically drops to 1.2 V vs. Li+/Li to reach a Li content of 0.28, after which the system undergoes a 2H to 1T MoS$_2$ first-order phase transition. The atomic structure is changed from trigonal prismatic to octahedral, along with the electronic semiconducting to metallic transition.[48]

1.3.2.3 Coupling with conductive scaffolds

Coupling MoS_2 with conductive scaffolds is an effective method to improve its electronic conductibility and increase the effective surface area, thereby enhancing the overall HER catalytic performance. Li et al. developed a selective solvothermal synthesis of MoS_2 nanoparticles on reduced graphene oxide (RGO) sheets suspended in solution (Figure 1.6a, b).[55] Superior electrocatalytic activity of the MoS_2/RGO hybrid was demonstrated with a Tafel slope of ∼41 mV/decade, which is significantly improved relative to other MoS_2 catalysts. The improved performance is attributed to the abundance of catalytic edge sites on the MoS_2 nanoparticles and the excellent electrical coupling to the underlying graphene network. The conducting graphene network provided the internal electron transport channels from the less-conducting MoS_2 nanosheets to the electrodes, and also prevented MoS_2 from aggregating. Similarly, a graphene deposited 3D Ni foam was also utilized as a solid support to load MoS_x catalysts for HER. Besides serving as conductive support, the graphene sheets grown on Ni foams also provide robust protection and efficiently increase its stability in acid (Figure 1.6c).[56] Mesoporous graphene foam (MGF), carbon nanotube, and carbon nanofiber were also employed to synthesize MoS_2–based nanocomposites that exhibit enhanced catalytic activity due to the electrical coupling to the conductive substrate network.[57,58] Usually, the increase of the surface area leads to increasing overall catalytic performance which could be accounted for by normalizing these electrochemical surface area, but not the enhancement of "intrinsic" catalytic activity of the catalyst.

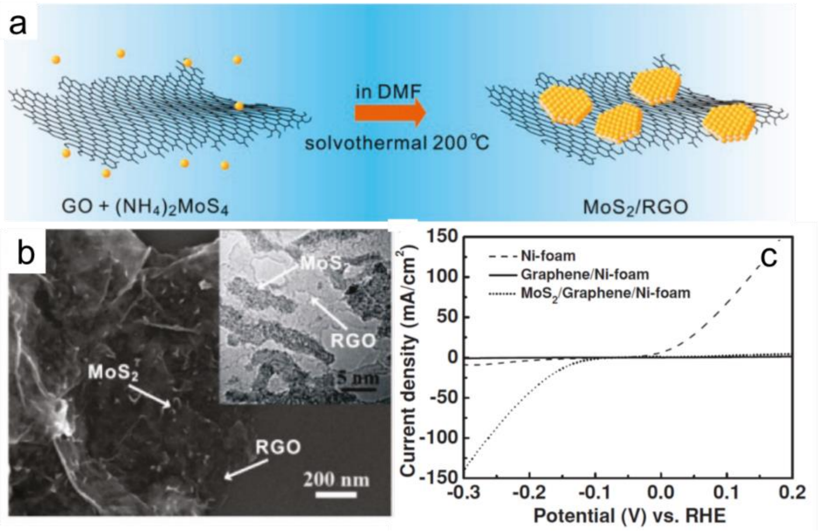

Figure 1.6. (a, b) Solvothermal synthesis of a MoS_2–graphene nanocomposite.[55] (c) The polarization curves of the as-obtained Ni foam electrode (dotted line), the graphene-protected Ni foam electrode (solid line), and the graphene-protected Ni foam electrode with MoS_x grown at 120 ˚C (dotted line).[56]

1.3.2.4 Amorphous MoS_x

Different from crystalline MoS_2, amorphous MoS_x has short-range ordered atomic arrangements and significant structural disorder, thus may possess more catalytic active sites for HER (Figure 1.7a). The amorphous catalysts can be synthesized using electrodeposition or wet chemical reactions with no thermal sulfidization treatment, and have demonstrated excellent catalytic activity.

Kibsgaard et al. reported utilizing supported thiomolybdate $[Mo_3S_{13}]^{2-}$ nanoclusters as a molecular HER catalyst (Figure 1.7b, c). The clusters can be viewed as molybdenum sulfide with a significant fraction of active sites, as most sulfur atoms in the structure exhibit a structural motif similar to that observed at MoS_2 edges, demonstrating high HER activity and stability in acid.[59] Vrubel et al showed that amorphous molybdenum sulfide catalyst could deliver a current density of 10 mA/cm^2 at an overpotential of 160 mV at a loading of 0.2 mg/cm^2.[60] While the initial compositions produced from different electrochemical deposition methods might be different, the active catalysts are the same and are identified as a "MoS_{2+x}" species.[60] The activity of the film catalysts can be further promoted when suitably doped with heteroatoms. Merki et al. investigated the promotion effect of first-row transition metal ions (Mn, Fe, Ni, Co, Cu and Zn) on the HER activity of MoS_x, and showed Fe, Co, and Ni ions were effective promoters to enhance its catalytic performance.[61] A Mo^{IV}-disulfide complex, which is a well-defined molecular analog of the proposed MoS_2 edge structure, was synthesized and structurally characterized by Karunadasa et al. After electrochemical reduction, hydrogen can be catalytically generated from acidic organic media as well as from acidic water.[62]

Due to the uncertain structure and atomic-scale heterogeneity, it is difficult to identify the catalytic active sites on amorphous MoS_x and reveal the precise catalytic mechanism. Several studies are conducted to provide a better understanding of the reaction mechanism.[10,63-67] The unsaturated S atoms in amorphous molybdenum sulfide have been shown to be similar to the edges of crystalline MoS_2 in terms of the catalytic function, and thus have been suspected to be the catalytically active sites for HER.[10,63-65] Tran et al. showed that the amorphous MoS_x is a molecular-based coordination polymer consisting of discrete $[Mo_3S_{13}]^{2-}$ building blocks. Two of the three terminal disulfide (S_2^{2-}) ligands within the cluster are shared to form the polymer chain, leaving the third one free and generates molybdenum hydride moieties as the active site under H_2 evolution conditions (Figure 1.7 b and c).[67] In situ X-ray absorption spectroscopy has also been utilized to provide insight into the reaction mechanism of amorphous molybdenum sulfide (MoS_x) under functional conditions. Structural model for the catalyst film as prepared and under functional conditions were proposed, and terminal disulfide units were shown to be present and involved in the HER catalytic cycle.[68]

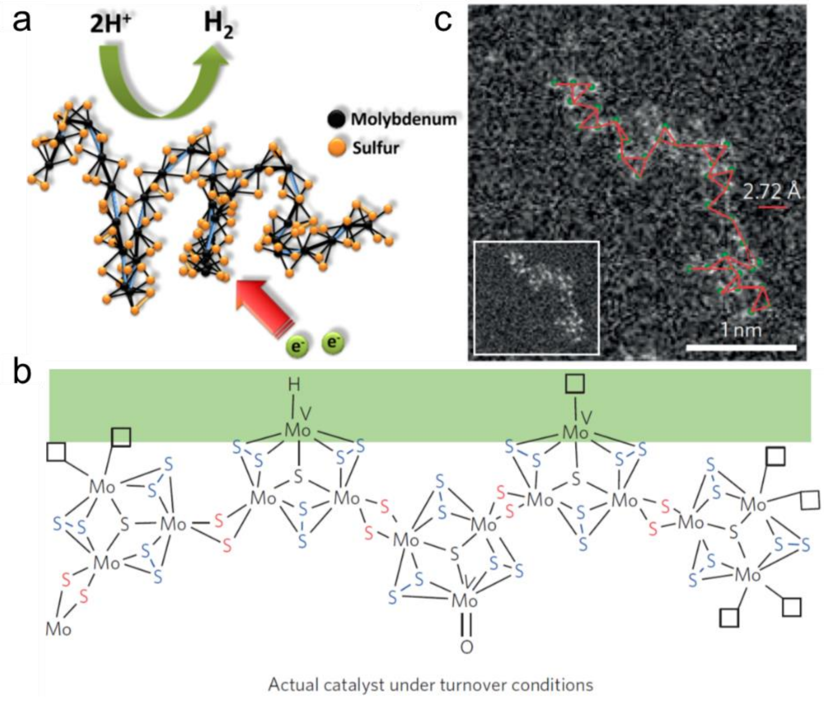

Figure 1.7. (a) Hydrogen evolution on amorphous MoS_x.[12] (b) Structures of *a*-MoS_x catalyst under catalytic H_2 evolution turnover conditions. (c) HAADF-STEM analysis revealing the arrangement of [Mo_3] cluster units in a one-dimensional unfolding chain.[67]

1.3.2.5 Amorphous ternary compounds

Besides amorphous MoS_x, ternary amorphous compounds have also been investigated and demonstrated to be superior HER catalysis. Jin's group developed novel high performance amorphous MoS_xCl_y and $MoSe_xCl_y$ HER electrocatalysts synthesized using low temperature chemical vapor deposition syntheses (Figure 1.8).[69,70] The obtained MoS_xCl_y exhibited stable and high catalytic activity toward the hydrogen evolution reaction, as evidenced by the large cathodic current densities at low overpotentials and low Tafel slopes (ca. 50 mV decade^{-1}). It is hypothesized that Cl further tunes the electronic structure of the amorphous samples to improve the catalytic activity. Furthermore, directly depositing MoS_xCl_y electrocatalyst on conducting vertical graphene further enhanced the highly competitive HER performance as compared to other state-of-the-art amorphous MoS_x or exfoliated metallic MoS_2 electrocatalysts, due to the synergistic effects of high intrinsic activity and large electrochemically active surface area.

Compared to MoS_x, CoS_x materials are more active but less stable. Staszak-Jirkovský et al designed a catalyst by combining the higher activity of CoS_x building blocks with the higher stability of MoS_x units into a compact and robust $CoMoS_x$ chalcogel structure, and demonstrated it could effectively catalyze HER in both alkaline and acidic environments.[71]

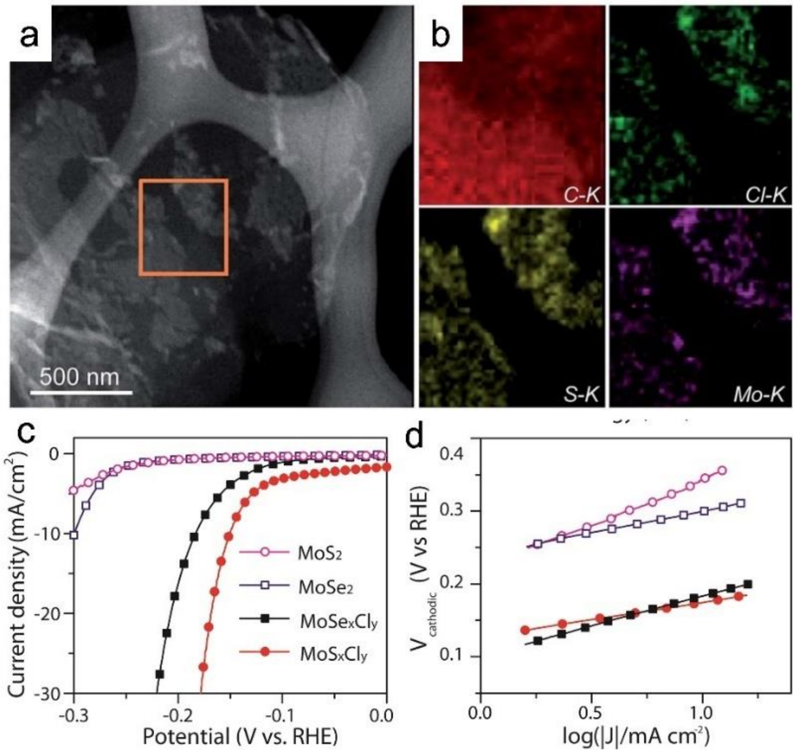

Figure 1.8. (a) Electron microscopy characterization of an amorphous MoS_xCl_y–vertical graphene (VG) sample grown at 275 ˚C. STEM-EDS mapping of a piece of graphene sheet partially covered by MoS_xCl_y. The orange box indicates the region where EDS elemental mapping (b) was performed for C, Cl, S, and Mo.[69] Electrochemical characterization of amorphous MoS_xCl_y (solid circles) and $MoSe_xCl_y$ (solid squares) thin films deposited on graphite substrates in comparison with crystalline MoS_2 (open circles) and $MoSe_2$ (open squares): (c) Polarization curves, (d) Tafel analysis.[72]

1.4 Photoelectrochemical Hydrogen Generation

Solar-driven photoelectrochemical water splitting combines solar light conversion with water splitting, and is regarded as one of the most promising approaches to store solar energy directly in the form of hydrogen fuel.[2,3] The solar-to-fuel conversion can be achieved by using either a photovoltaics-electrolyzer system or an integrated photoelectrochemical (PEC) system that couples the light harvesting system with the water splitting system in a single device.[4,6] It is much more economical and attractive to utilize integrated PEC systems to directly split water at the semiconductor interface.

1.4.1 Components in PEC

Two essential components are required in a PEC system, a light absorber/semiconductor that generates electron−hole pairs upon illumination, and an electrocatalyst that facilitates charge transfer and reduces the overpotential for fuel production. Solar-driven water splitting could be achieved either using one single semiconductor with a large bandgap (> 1.7 eV), or combining two or more semiconductors in a tandem PEC cell that consists of an integrated oxygen-evolving photoanode and a hydrogen-evolving photocathode. Compared with using a single semiconductor, the tandem configuration allows the utilization of semiconductors with much smaller bandgaps and enabled access to a larger part of the solar spectrum. As illustrated in Figure 1.9, the blue part of the solar spectrum is absorbed by a photoanode, where water is oxidized to release oxygen and protons. The red part of the spectrum, passes through to be absorbed by the photocathode, where protons are reduced to evolve hydrogen.[18] Here, we will focus on developing efficient photocathodes based on MoS_2 and related HER electrocatalysts for photoelectrochemical hydrogen evolution reaction (PEC-HER).

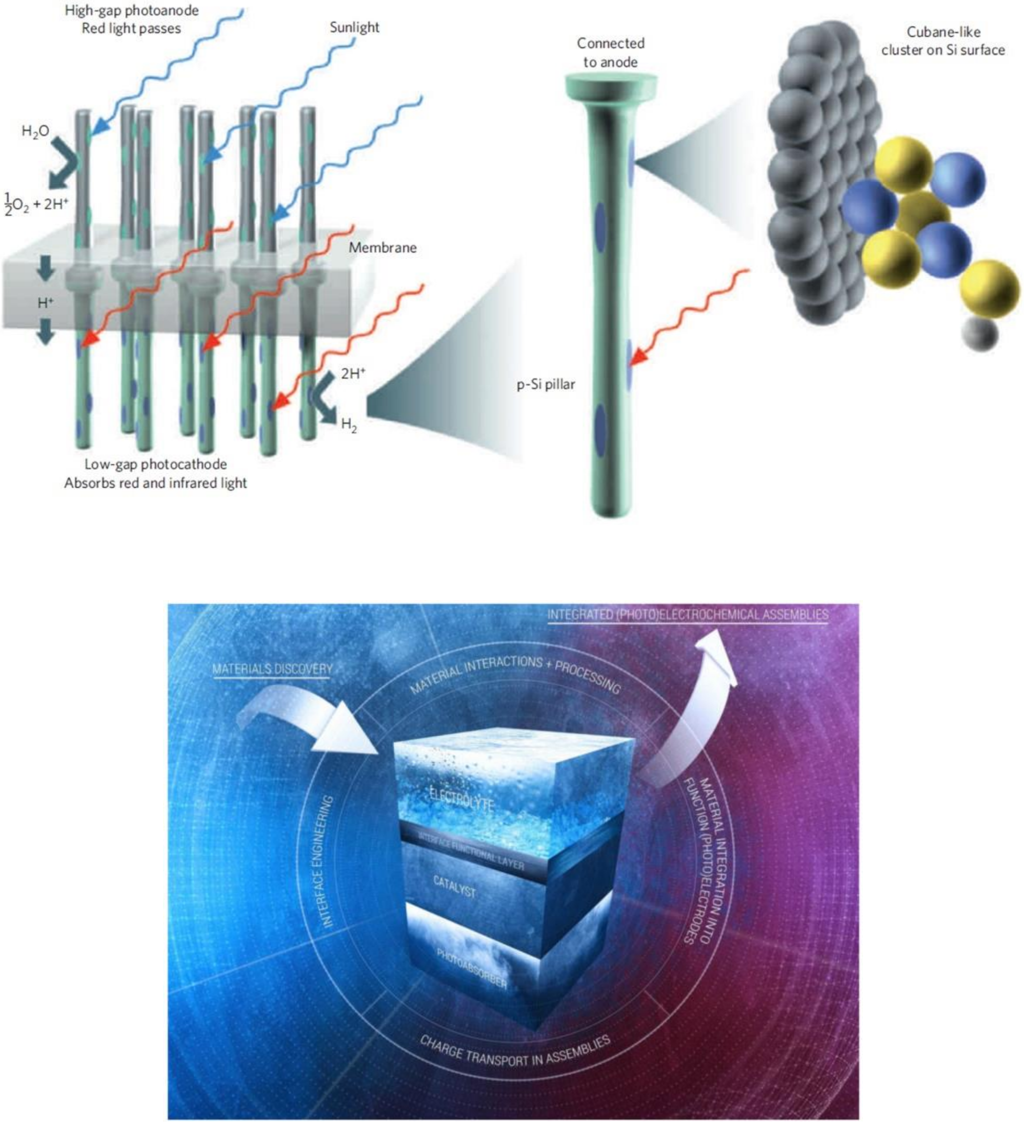

Figure 1.9. Schematic of the tandem ‘chemical solar cell’. Left, the entire system. Pillars are embedded in a proton-conducting membrane. The solar light is incident from above and the blue part of the spectrum is absorbed by the anode used for oxidizing water into molecular oxygen and protons. The protons migrate through the membrane and are reduced at the cathode side, which are excited by the red part of the spectrum. Right, hydrogen evolution on the Si pillars modified by the adsorbed Mo_3S_4 clusters.[73]

1.4.2 Important parameters in PEC systems

The performance of photoelectrodes towards PEC-HER can be calculated from current-voltage data obtained using a potentiostat in an illuminated three-electrode cell. The important parameters for describing and comparing the PEC performance include open-circuit voltage (V_{oc}), short-circuit current density (J_{sc}), fill factor (FF), and the saturation current density.

Open-circuit voltage (V_{oc}) represents the electrical potential when the photoelectrode passed zero current during the experiments. This V_{oc} is the photovoltage that would be produced in a regenerative two-electrode cell in which the counter electrode was performing the oxidation of H_2 to H^+. Short-circuit current density (J_{sc}) is the current density measured at 0 V vs. RHE. The fill factor (FF) can be calculated from the open-circuit potential V_{oc} and short circuit current density J_{sc} using equation (11), where J_{mp} is the current density at the maximum power point and V_{mp} is the voltage at the maximum power point. Saturation current density is the maximum current density achieved in a photoelectrode system, and usually reflects the light harvesting ability of the semiconductor.

$$FF = \frac{I_{mp}V_{mp}}{I_{sc}V_{OC}} \tag{11}$$

To develop efficient PEC-HER system, catalyst needs to be integrated with the semiconductor to effectively convert solar light to hydrogen fuel. Despite significant progress in the development of new earth-abundant, inexpensive, and nontoxic catalysts for HER, most of these new materials have only been investigated as stand-alone electrocatalysts, and only some of them have been integrated into photocathodes. Partially because MoS_2 is one of the early developed HER earth-abundant catalysts, the study of MoS_2 in integrated PEC is perhaps the most developed. Many challenges remain present in the development of efficient photocathodes, including the difficulty in effectively integrating the electrocatalysts with the light absorbers due to the semiconductor/catalyst chemical incompatibility and stability issues, induced interfacial defect states and recombination sites, synthetic difficulties, suitable band alignment requirement, and ensuring efficient charge transfer across multiple interface, etc. In 1998, Khaselev et al demonstrated a photoelectrochemical cell biased with an integrated photovoltaic device could split water directly upon illumination utilizing an integrated, monolithic photoelectrochemical-photovoltaic design. The solid-state tandem cell consists of a GaAs bottom cell and a $GaInP_2$ top cell. Utilizing Pt as the HER catalyst, a hydrogen production efficiency of 12.4 percent was demonstrated.[7] Recently, several photocathodes based on non-noble metal catalysts for solar-driven HER have been reported;[11] but there is still room for their chemical stability and PEC performance to be improved. Herein, we highlight some of the well-developed photocathode systems based on MoS_2 and related compounds for solar-driven HER, and offer our perspectives on how to design the most efficient PEC-HER photocathode in hopes of lighting a path toward achieving performance competitive with their noble metal-containing analogues.

1.5 Incorporating MoS_2 HER Catalysts in Photoelectrochemical Water Splitting

To design efficient photocathodes, three major aspects need to be considered: (1) the semiconductor; (2) the catalyst and (3) the interface.

1.5.1 Design silicon semiconductor

The study of utilizing silicon as the photocathode material is the most developed. P-type silicon (p-Si) is an earth-abundant and inexpensive semiconductor with a suitable band gap (1.1

eV) and is excellent for capturing photons in the red part of the solar spectrum.[74,75] It has been widely utilized as a light absorber in photocathodes and demonstrated high efficiency. Chorkendorff's group utilized p-Si as the semiconductor material and integrated it with incomplete cubane-like clusters (Mo_3S_4).[73] Under illumination, the integrated photocathode could successfully catalyze HER, yielding a V_{oc} of 0.15 V and a J_{sc} of 8 mA/cm^2. However, one challenge of utilizing p-type silicon for PEC-HER is its intrinsic low photovoltage, which is limited by the Si/liquid junction. Depositing an n^+ layer on top of p-Si can effectively replace the Si/liquid junction with a built-in p-n junction, therefore significantly boosts the photovoltage of the PEC system, as shown in the band bending scheme in Figure 1.10. In cases where the band alignment is influenced by the catalyst, the built-in p-n junction also remove the constraints placed on the catalysts used in this system. Using Pt film as the catalyst layer, Boettcher et al. have demonstrated both Si wire array photoelectrodes and planar Si photoelectrodes exhibited significant enhancement in V_{oc}, J_{sc}, and fill factor when utilizing n^+p Si.[75,76] In the case of Ni-Mo catalyzed photocathodes, the V_{oc} also improved from 0.14 V in Ni-Mo/p-Si MW to 0.46 V in Ni-Mo/n^+p Si MW.[75,76]

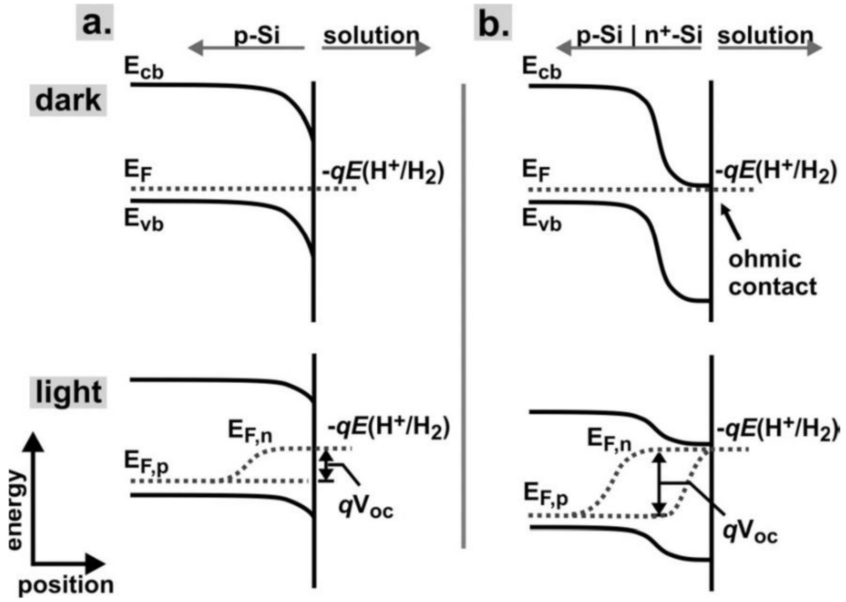

Figure 1.10. Band bending in (a) p-Si and (b) n^+p-Si photocathodes in contact with the H^+/H_2 redox couple in solution. The top diagrams show the interfaces in the dark, whereas the bottom diagrams show the interfaces under illumination. E_{cb} is the conduction band edge, E_{vb} the valence band edge, and E_F the Fermi level. $E_{F,p}$ and $E_{F,n}$ are the hole and electron quasi-Fermi levels, respectively, under illumination. The photovoltage (V_{oc}) is larger for n^+p-Si samples due to increased band bending at the n^+/p interface relative to the aqueous solution/p-Si interface.[76]

Besides large photovoltage, high photocurrent is another prerequisite for highly efficient PEC devices. The light harvesting and carrier collection of the semiconductor plays the most important role in the achievable photocurrent. To further improve the light trapping ability of planar Si, nano- and microstructuring of Si have been investigated.[75] Si wire arrays exhibited enhanced absorption due to its large surface area and reduced light scattering.[77] In addition, in the nanowire or microwire geometry, the length scales for light absorption and carrier separation are decoupled into two orthogonal direction, leading to enhanced carrier collection. Besides those examples using Pt catalyst, Hou et al. showed an enhancement in the achieved photocurrent for Si pillars based photocathodes compared to Si planar based photocathodes.[73] Nevertheless, higher density of surface states and faster recombination rates were simultaneously observed with increased surface area in Si nano- and microwire-based photocathodes, limiting the potential gains in efficiency.[75,76,78,79] Alternatively, Si micropyramids (MPs)-based solar cells have been shown to exhibit high efficiency because of the omnidirectional broadband light-trapping ability.[80] Since MP structured Si surface is etched along the (111) direction with the least dangling bonds, it has the lowest surface state density as compared to structures such as silicon nanowires, cones or tubes, making them uniquely suited for PEC-HER light absorbers. Ding et al. have incorporated MoQ_xCl_y (Q=S, Se) catalysts on these Si MPs for photocathodes, and achieved the highest current density reported for Si based photocathode systems owing to its dramatically increased light harvesting ability of Si MPs.

1.5.2 Enhance the catalytic activity

The choice of catalysts also plays a key role in the PEC-HER performance. Two criteria need to be considered when choosing a PEC-HER catalyst: high HER catalytic activity, and good optical transparency. More active HER catalysts usually lead to better overall PEC performance especially with better onset potential. Seger et al. electrodeposited MoS_x on Ti-protected n^+p-silicon electrode, and demonstrated largely enhanced PEC performance compared to bare Si electrode with good V_{oc} and FF.[81] The thin layer of Ti on Si acts as a conductive protection layer on Si, drastically enhancing the stability of the photocathode. While Ti layer can help to protect Si from oxidation, it also blocks Si from absorbing light. The Ti thickness must be thick enough so that pinholes in the surface do not lead to oxidation, but thin enough to allow light to pass through. As a result, a decrease in the saturation current density was observed from the Ti-coated samples. In another case, Benck et al. showed that a conformal layer of MoS_2 on the Si photoelectrode surface can serve as both catalytic material and protection layer,[82] showing no loss in performance after 100 h operation. But the lack of active sites for the flat MoS_2 layer required the addition of $[Mo_3S_{13}]^{2-}$ clusters to further enhance its PEC-HER catalytic performance. Because of the light absorption in the MoS_2 layers blocks the light from passing through, the photocurrent density achieved in the system is limited. Amorphous $CoMoS_x$ catalyst has been reported as a HER catalyst and has also been deposited on Si via a photoassisted electrodeposition process and utilized as PEC-HER photocathode. In pH 4.25 phosphate solution, an onset potential of 0.25 V vs RHE and photocurrent jsc of 17.5 mA/cm^2 at 0 V vs RHE were achieved under simulated 1 sun irradiation.

Compared to 2H-MoS_2, 1T-MoS_2 has been shown to exhibit significantly enhanced HER catalytic activity.[45] When incorporating into PEC systems using planar p-type Si as the semiconductor, Ding et al. demonstrated 1T-MoS_2/Si heterostructure serves as efficient and robust photocathodes for PEC hydrogen generation (Figure 1.11). For as-grown 2H-MoS_2/Si photocathode, the onset potential and J_{sc} were measured to be 0.23 V vs RHE and 4.2 mA/cm^2, respectively. After phase conversion to 1T-MoS_2/Si, both the onset potential and J_{sc} improved significantly, reaching 0.25 V vs RHE and 17.6 mA/cm^2, respectively. Electrochemical impedance spectroscopy revealed low charge-transfer resistances at the semiconductor/catalyst and catalyst/electrolyte interfaces, confirming the facile electrode kinetics of 1T-MoS_2/Si and further proving that the 1T-MoS_2 is indeed much more catalytically active toward HER than 2H. Although 1T-MoS_2 is the thermodynamically metastable phase, these 1T-MoS_2/Si photocathodes remain stable and catalytically active over long-term operation.

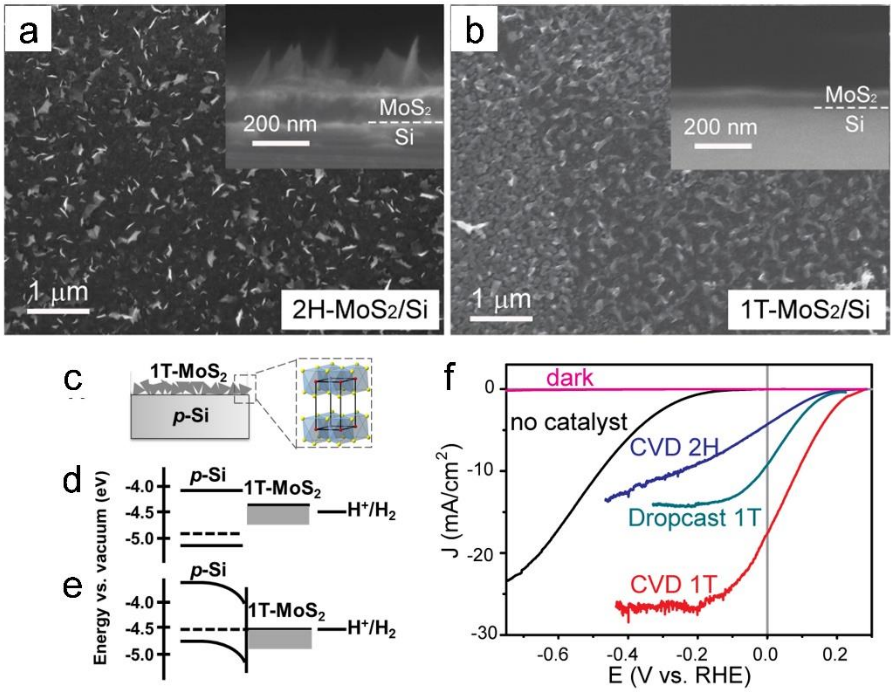

Figure 1.11. Comparison of top-down and cross-sectional (insets) SEM images of (a) 2H- and (b) 1T-MoS_2/Si. (c) Illustration of 1T-MoS_2 on p-Si. Schematic band energy diagram of p-Si, 1T-MoS_2, and H^+/H_2 redox couple at 0 V vs RHE in the dark before (d) and after (e) equilibrium. (f) J−E curves of a CVD grown 2H-MoS_2/Si photocathode (CVD 2H), a CVD grown 1T-MoS_2/Si photocathode (CVD 1T), and a dropcasted 1T-MoS_2/Si photocathode (dropcast 1T) measured in 0.5M H_2SO_4 under simulated 1 sun irradiation. The J−E curve of a bare Si photocathode is also shown as a comparison.[70]

1.5.3 Optimize the optical transparency

Currently, catalysts are primarily evaluated based on their electrocatalytic activity. However, as discussed before, optical transparency of catalysts also plays a crucial role in the overall PEC performance. Despite good electrocatalytic activity, most reported HER catalysts suffer from strong light absorption or high reflection, which consequently reduces the light reaching the absorbers and decreases the generated photocurrent. Hence, in those cases, balancing high catalyst loading and good optical transparency becomes one of the major challenges.[6,14] Therefore, catalysts with good optical transparency would present particular advantages.

MoS_xCl_y is an efficient catalyst for HER, exhibiting catalytic activity comparable to that of 1T-MoS_2 (Figure 1.7).[69] Simply depositing a thin film of amorphous MoS_xCl_y on p-type Si led to a competitive V_{oc} and J_{sc}, even slightly better than that achieved by 1T-MoS_2 on p-Si (Figure 1.12b). Moreover, unlike 1T-MoS_2 and most other HER catalysts, MoS_xCl_y is a semi-transparent catalyst with little light absorption in visible and near-infrared (IR) range due to its large band-gap. By integrating MoS_xCl_y catalyst with n^+pp^+Si micropyramids (MPs), Ding et al. report the highest photocurrent density reported for Si-based PEC-HER photocathodes using non-noble metal catalysts (Figure 1.12). A J_{sc} of 43 mA/cm^2 was achieved for MoS_xCl_y/Si MP photocathode, which even surpasses the current density achieved by Pt/n^+pp^+ Si MPs, due to the synergistic effects of the high-transparency of the catalyst and the efficient light-trapping property of the Si micropyramid structure. The further increased V_{oc} is because of the p-n junction in n^+pp^+ Si MPs, similar to the enhancement seen for the previous examples.

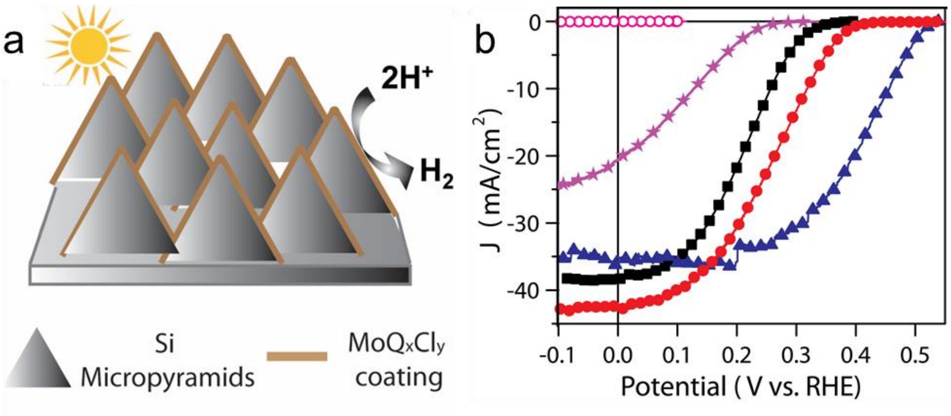

Figure 1.12. (a) Schematic of MoQ_xCl_y catalysts coated on n^+pp^+ Si MPs. (b) *J*–*E* curves for amorphous MoS_xCl_y/planar p-Si (purple stars), MoS_xCl_y/Si MPs (red circles), $MoSe_xCl_y$/Si MPs (black squares) and Pt/Si MPs (blue triangles) photocathodes measured under simulated 1 sun irradiation in 0.5 M H_2SO_4.[69,72]

1.5.4 Improve the catalyst/semiconductor junction/interface

The efficiency of electrochemical water splitting is determined not only by the semiconductor and catalyst themselves, but also their compatibility and interface. The junction between the semiconductor and catalyst significantly affects the V_{oc} achievable in the system. A large junction barrier is desirable in order to maximize the V_{oc}, but in cases where the two materials forming an ohmic junction, a built-in junction (such as n^+p Si) could be utilized to decouple the semiconductor/liquid junction and replace it with the built-in junction. Moreover, the quality of the interface also needs to be improved in order to design the most efficient PEC system. Ding et al. compared two types of 1T-MoS_2/Si heterostructures prepared using different approaches, one via simple dropcasting experiment, the other via CVD. As shown in Figure 1.11, the CVD grown 1T-MoS_2/Si demonstrate higher V_{oc}, higher J_{sc}, as well as higher saturation current density. The direct CVD grown 1T-MoS_2/Si heterostructure exhibits a much lower charge-transfer resistance across Si/MoS_2 interface than the dropcasted 1T-MoS_2/Si as revealed in the electrochemical impedance spectroscopy, which confirms that the CVD grown MoS_2/Si heterostructure indeed has a higher quality interface between the light absorber and catalyst. This is in good agreement with the observed superior performance of the CVD 1T-MoS_2/Si and highlights the benefits of direct CVD growth of catalysts on photocathodes for effective PEC system integration.

1.5.5 PEC-HER using other semiconductor photocathodes

Previous discussion has been focused on Si based photoelectrodes, but the photocathode in the tandem system is not limited to Si. Other p-type semiconductors potentially have large bandgaps and more favorable band positions that could theoretically allow higher V_{oc} than silicon, even though for larger band gap semiconductors, the theoretically maximum J_{sc} could be limited.

Morales-Guio et al. demonstrated PEC-HER by integrating amorphous MoS_{2+x} electrocatalysts onto copper(I) oxide (Figure 1.13a).[83] Copper(I) oxide is a low-cost solar materials with a band gap suitable for capturing a large portion of the visible spectrum. Ultrathin layers of aluminum-doped zinc oxide (AZO, 20 nm) were deposited to form a buried Cu_2O/AZO photovoltaic junction to enable the photovoltage, and titanium dioxide (TiO_2: 100 nm) film were deposited by atomic layer deposition (ALD) to protect the buried junction from the aqueous environment and transports the photogenerated electrons to the electrolyte where water reduction takes place. This TiO_2 protection layer is an important and necessary step since Cu_2O is not stable in either acid or base. An onset potential of 0.45 V vs RHE and photocurrents up to 5.7 mA/cm^2 at 0 V vs RHE (pH 1.0) were achieved under simulated AM 1.5 solar illumination. Moreover, compared using platinum nanoparticles as catalysts, the MoS_{2+x} based photocathode exhibits enhanced stability under acidic environments. In another study, amorphous MoS_x and a Ni-Mo catalyst are integrated on TiO_2 protected Cu_2O photocathodes, and active and stable hydrogen evolution is being demonstrated in alkaline solutions.[84]

Gao et al also reported using vertically aligned p-type InP nanowire arrays coated with MoS_3 nanoparticles as the photocathode for photoelectrochemical hydrogen production (Figure 1.13b).[85] The p-type indium phosphide (p-InP) is an attractive photocathode for HER due to its small band gap, appropriate band-edge potential, and low surface-recombination velocity. A V_{oc} of 0.60 V and FF of 0.44 were achieved under Air Mass 1.5G illumination, generating a photocathode efficiency of 6.4%. However, the large-scale application of InP-based photocathodes might be limited by the scarcity of indium element. P-type wurtzite gallium phosphide nanowires were also utilized as photocathode materials. Standing et al. deposited MoS_x on an electrochemically produced oxide (EPO) passivated GaP photocathode, and achieved a V_{OC} of

0.71V (versus RHE) and a J_{sc} of 6.4mA/cm^2.[86] Gallium indium phosphide ($GaInP_2$) is another semiconductor with promising optical and electronic properties for solar water splitting. Thin layer of molybdenum disulfide (MoS_2) nanomaterials were coated on $GaInP_2$ photocathodes, leading to significantly improved activity and stability, with no loss in performance after 60 h of operation.[87]

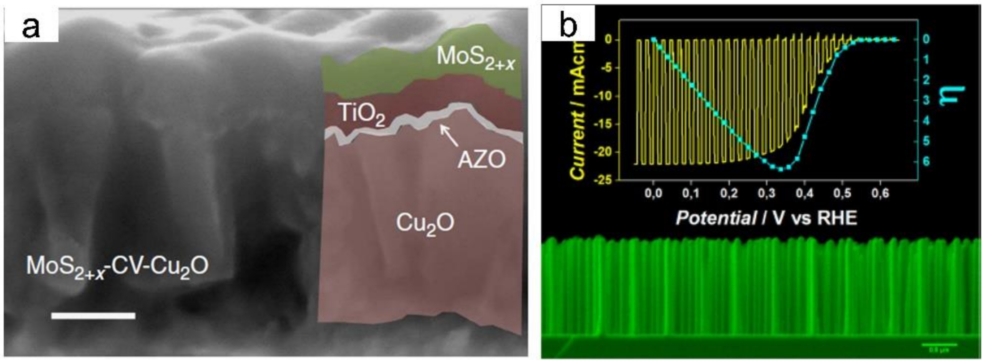

Figure 1.13. (a) Cross-sectional SEM image of the protective layers (20nm AZO and 100nm TiO_2) on Cu_2O and (right) a ca. 100nm of MoS_{2+x} film on top of the TiO_2 protected Cu_2O electrode.[83] Scale bars, 200 nm. (b) Current−potential curves (black solid line) and photocathode conversion efficiencies (blue squares) of as-grown InP nanowire arrays with MoS_3 in 1 M $HClO_4$ under chopped AM1.5G illumination.[85]

1.6 Summary and Outlooks

We have discussed various approaches to enable MoS_2 and related compounds as efficient electrocatalysts for HER, and highlighted the current state-of-the-art discoveries. We also reviewed the development of combining MoS_2 with semiconductors for integrated photoelectrochemical (PEC) systems to enable direct solar-driven hydrogen generation, and offered perspectives on how to design efficient integrated PEC systems.

Although HER catalytic activity by molybdenum sulfide and related compounds has been significantly improved, the efficiency remains lower than Pt. In order to make further progress, several aspects need to be considered in future research, besides the exploratory investigation necessary.

a) Mechanism investigation

Despite the rapid expansion of new materials being utilized for HER catalysis, many of them lack in-depth understanding of the catalytic mechanism on an atomic level. Investigation of origin or fundamental nature of their activity not only can provide scientific guidance regarding how to optimize the materials' performances, but could also provide guideline for the development of future related materials.

b) Better coupling between theoretical with experimental studies

Theoretical and computational studies should be better integrated with experimental work in order to enable more targeted and rational material development. Theoretical calculations have been shown to be successful in predicting some of the promising HER catalysts[14,18,20] and the knowledge learnt from these studies should be more widely utilized to guide the experimental design. MoS_2 family has been perhaps the most systematically studied and understood family. Experimental discoveries have stimulated additional theoretical works. The successful feedback loop between theory and experiments would accelerate the understanding and new discoveries.

c) Development of PEC-HER systems

The development of catalysts towards electrochemical hydrogen evolution has been undergoing rapid expansion, whereas the advance in PEC-HER has been relatively slow. In order to realize direct solar-to-fuel conversion using earth-abundant materials, more effort is needed to overcome the many challenges in this area. Efficient and inexpensive semiconductor materials should be developed, either via exploring new materials, or via improving on currently available materials. Despite some progress,[81,82] the stability of photoelectrode continues to be a major challenge and should be further improved to maintain high efficiency under long-time operation. With the large number of efficient catalysts that have been developed, more effort should be spent on incorporating them into PEC systems to design appropriate junctions and interfaces. Photocathodes also need to be incorporated with photoanode materials to complete the tandem configuration for solar fuel production. Partially because MoS_2 is one of the earliest earth-abundant catalysts investigated for HER, its development for electrochemical and photoelectrochemical HER can serve as a model for other newly developed HER catalysts. With further progress in MoS_2 catalysts and other new catalysts, some of which, have surpass MoS_2 in terms of electrocatalytic activity, there are significant promises in realizing highly efficient photoelectrochemical hydrogen generation using all earth-abundant systems.

1.7 References

(1) Chu, S.; Majumdar, A. *Nature* **2012**, *488*, 294.

(2) Turner, J. A. *Science* **2004**, *305*, 972.

(3) Lewis, N. S.; Nocera, D. G. *P. Natl. Acad. Sci. USA.* **2006**, *103*, 15729.

(4) Walter, M. G.; Warren, E. L.; McKone, J. R.; Boettcher, S. W.; Mi, Q. X.; Santori, E. A.; Lewis, N. S. *Chem. Rev.* **2010**, *110*, 6446.

(5) Bard, A. J.; Fox, M. A. *Accounts Chem. Res.* **1995**, *28*, 141.

(6) McKone, J. R.; Lewis, N. S.; Gray, H. B. *Chem. Mater.* **2014**, *26*, 407.

(7) Khaselev, O.; Turner, J. A. *Science* **1998**, *280*, 425.

(8) Faber, M. S.; Jin, S. *Energ. Environ. Sci.* **2014**, *7*, 3519.

(9) Zeng, M.; Li, Y. G. *J. Mater. Chem. A* **2015**, *3*, 14942.

(10) Benck, J. D.; Hellstern, T. R.; Kibsgaard, J.; Chakthranont, P.; Jaramillo, T. F. *ACS Catal.* **2014**, *4*, 3957.

(11) Laursen, A. B.; Kegnaes, S.; Dahl, S.; Chorkendorff, I. *Energ. Environ. Sci.* **2012**, *5*, 5577.

(12) Morales-Guio, C. G.; Hu, X. L. *Accounts Chem. Res.* **2014**, *47*, 2671.

(13) Faber, M. S.; Dziedzic, R.; Lukowski, M. A.; Kaiser, N. S.; Ding, Q.; Jin, S. *J. Am. Chem. Soc.* **2014**, *136*, 10053.

(14) Caban-Acevedo, M.; Stone, M. L.; Schmidt, J. R.; Thomas, J. G.; Ding, Q.; Chang, H. C.; Tsai, M. L.; He, J. H.; Jin, S. *Nat. Mater.* **2015**, *14*, 1245.

(15) Cook, T. R.; Dogutan, D. K.; Reece, S. Y.; Surendranath, Y.; Teets, T. S.; Nocera, D. G. *Chem. Rev.* **2010**, *110*, 6474.

(16) Bockris, J. O. M.; Potter, E. C. *J. Electrochem. Soc.* **1952**, *99*, 169.

(17) Norskov, J. K.; Bligaard, T.; Logadottir, A.; Kitchin, J. R.; Chen, J. G.; Pandelov, S.; Norskov, J. K. *J. Electrochem. Soc.* **2005**, *152*, J23.

(18) Hinnemann, B.; Moses, P. G.; Bonde, J.; Jorgensen, K. P.; Nielsen, J. H.; Horch, S.; Chorkendorff, I.; Norskov, J. K. *J. Am. Chem. Soc.* **2005**, *127*, 5308.

(19) Greeley, J.; Jaramillo, T. F.; Bonde, J.; Chorkendorff, I. B.; Norskov, J. K. *Nat. Mater.* **2006**, *5*, 909.

(20) Jaramillo, T. F.; Jorgensen, K. P.; Bonde, J.; Nielsen, J. H.; Horch, S.; Chorkendorff, I. *Science* **2007**, *317*, 100.

(21) Chhowalla, M.; Shin, H. S.; Eda, G.; Li, L. J.; Loh, K. P.; Zhang, H. *Nat. Chem.* **2013**, *5*, 263.

(22) Xu, M. S.; Liang, T.; Shi, M. M.; Chen, H. Z. *Chem. Rev.* **2013**, *113*, 3766.

(23) Butler, S. Z.; Hollen, S. M.; Cao, L. Y.; Cui, Y.; Gupta, J. A.; Gutierrez, H. R.; Heinz, T. F.; Hong, S. S.; Huang, J. X.; Ismach, A. F.; Johnston-Halperin, E.; Kuno, M.; Plashnitsa, V. V.; Robinson, R. D.; Ruoff, R. S.; Salahuddin, S.; Shan, J.; Shi, L.; Spencer, M. G.; Terrones, M.; Windl, W.; Goldberger, J. E. *ACS Nano* **2013**, *7*, 2898.

(24) Nicolosi, V.; Chhowalla, M.; Kanatzidis, M. G.; Strano, M. S.; Coleman, J. N. *Science* **2013**, *340*, 1420.

(25) Mak, K. F.; Lee, C.; Hone, J.; Shan, J.; Heinz, T. F. *Phys. Rev. Lett.* **2010**, *105*, 136805.

(26) Mouri, S.; Miyauchi, Y.; Matsuda, K. *Nano. Lett.* **2013**, *13*, 5944.

(27) Yin, Z. Y.; Li, H.; Li, H.; Jiang, L.; Shi, Y. M.; Sun, Y. H.; Lu, G.; Zhang, Q.; Chen, X. D.; Zhang, H. *ACS Nano* **2012**, *6*, 74.

(28) Lee, H. S.; Min, S. W.; Chang, Y. G.; Park, M. K.; Nam, T.; Kim, H.; Kim, J. H.; Ryu, S.; Im, S. *Nano. Lett.* **2012**, *12*, 3695.

(29) Wu, S. F.; Buckley, S.; Schaibley, J. R.; Feng, L. F.; Yan, J. Q.; Mandrus, D. G.; Hatami, F.; Yao, W.; Vuckovic, J.; Majumdar, A.; Xu, X. D. *Nature* **2015**, *520*, 69.

(30) Radisavljevic, B.; Radenovic, A.; Brivio, J.; Giacometti, V.; Kis, A. *Nat. Nanotechnol.* **2011**, *6*, 147.

(31) Tributsch, H.; Bennett, J. C. *J. Electroanal. Chem.* **1977**, *81*, 97.

(32) Kong, D. S.; Wang, H. T.; Cha, J. J.; Pasta, M.; Koski, K. J.; Yao, J.; Cui, Y. *Nano Lett.* **2013**, *13*, 1341.

(33) Kibsgaard, J.; Chen, Z. B.; Reinecke, B. N.; Jaramillo, T. F. *Nat. Mater.* **2012**, *11*, 963.

(34) Yang, L.; Hong, H.; Fu, Q.; Huang, Y. F.; Zhang, J. Y.; Cui, X. D.; Fan, Z. Y.; Liu, K. H.; Xiang, B. *ACS Nano* **2015**, *9*, 6478.

(35) Xie, J. F.; Zhang, H.; Li, S.; Wang, R. X.; Sun, X.; Zhou, M.; Zhou, J. F.; Lou, X. W.; Xie, Y. *Adv. Mater.* **2013**, *25*, 5807.

(36) Chung, D. Y.; Park, S. K.; Chung, Y. H.; Yu, S. H.; Lim, D. H.; Jung, N.; Ham, H. C.; Park, H. Y.; Piao, Y.; Yoo, S. J.; Sung, Y. E. *Nanoscale* **2014**, *6*, 2131.

(37) Saadi, F. H.; Carim, A. I.; Velazquez, J. M.; Baricuatro, J. H.; McCrory, C. C. L.; Soriaga, M. P.; Lewis, N. S. *ACS Catal.* **2014**, *4*, 2866.

(38) Hong, J. H.; Hu, Z. X.; Probert, M.; Li, K.; Lv, D. H.; Yang, X. N.; Gu, L.; Mao, N. N.; Feng, Q. L.; Xie, L. M.; Zhang, J.; Wu, D. Z.; Zhang, Z. Y.; Jin, C. H.; Ji, W.; Zhang, X. X.; Yuan, J.; Zhang, Z. *Nat. Commun.* **2015**, *6*, 6293.

(39) Qiu, H.; Xu, T.; Wang, Z. L.; Ren, W.; Nan, H. Y.; Ni, Z. H.; Chen, Q.; Yuan, S. J.; Miao, F.; Song, F. Q.; Long, G.; Shi, Y.; Sun, L. T.; Wang, J. L.; Wang, X. R. *Nat. Commun.* **2013**, *4*, 2642.

(40) Yu, Z. H.; Pan, Y. M.; Shen, Y. T.; Wang, Z. L.; Ong, Z. Y.; Xu, T.; Xin, R.; Pan, L. J.; Wang, B. G.; Sun, L. T.; Wang, J. L.; Zhang, G.; Zhang, Y. W.; Shi, Y.; Wang, X. R. *Nat. Commun.* **2014**, *5*, 5290.

(41) Lin, S. H.; Kuo, J. L. *Phys. Chem. Chem. Phys.* **2015**, *17*, 29305.

(42) Li, H.; Tsai, C.; Koh, A. L.; Cai, L. L.; Contryman, A. W.; Fragapane, A. H.; Zhao, J. H.; Han, H. S.; Manoharan, H. C.; Abild-Pedersen, F.; Norskov, J. K.; Zheng, X. L. *Nat. Mater.* **2016**, *15*, 48.

(43) Li, H.; Du, M.; Mleczko, M. J.; Koh, A. L.; Nishi, Y.; Pop, E.; Bard, A. J.; Zheng, X. L. *J. Am. Chem. Soc.* **2016**, *138*, 5123.

(44) Xie, J. F.; Zhang, J. J.; Li, S.; Grote, F.; Zhang, X. D.; Zhang, H.; Wang, R. X.; Lei, Y.; Pan, B. C.; Xie, Y. *J. Am. Chem. Soc.* **2013**, *135*, 17881.

(45) Lukowski, M. A.; Daniel, A. S.; Meng, F.; Forticaux, A.; Li, L. S.; Jin, S. *J. Am. Chem. Soc.* **2013**, *135*, 10274.

(46) Voiry, D.; Salehi, M.; Silva, R.; Fujita, T.; Chen, M. W.; Asefa, T.; Shenoy, V. B.; Eda, G.; Chhowalla, M. *Nano Lett.* **2013**, *13*, 6222.

(47) Ambrosi, A.; Sofer, Z.; Pumera, M. *Small* **2015**, *11*, 605.

(48) Wang, H. T.; Lu, Z. Y.; Xu, S. C.; Kong, D. S.; Cha, J. J.; Zheng, G. Y.; Hsu, P. C.; Yan, K.; Bradshaw, D.; Prinz, F. B.; Cui, Y. *P. Natl. Acad. Sci. USA.* **2013**, *110*, 19701.

(49) Lukowski, M. A.; Daniel, A. S.; English, C. R.; Meng, F.; Forticaux, A.; Hamers, R. J.; Jin, S. *Energ. Environ. Sci.* **2014**, *7*, 2608.

(50) Eng, A. Y. S.; Ambrosi, A.; Sofer, Z.; Simek, P.; Pumera, M. *ACS Nano* **2014**, *8*, 12185.

(51) Ambrosi, A.; Sofer, Z.; Pumera, M. *Chem. Commun.* **2015**, *51*, 8450.

(52) Gao, G. P.; Jiao, Y.; Ma, F. X.; Jiao, Y. L.; Wacawik, E.; Du, A. J. *J. Phys. Chem. C* **2015**, *119*, 13124.

(53) Putungan, D. B.; Lin, S. H.; Kuo, J. L. *Phys. Chem. Chem. Phys.* **2015**, *17*, 21702.

(54) Tsai, C.; Chan, K. R.; Norskov, J. K.; Abild-Pedersen, F. *Surf. Sci.* **2015**, *640*, 133.

(55) Li, Y. G.; Wang, H. L.; Xie, L. M.; Liang, Y. Y.; Hong, G. S.; Dai, H. J. *J. Am. Chem. Soc.* **2011**, *133*, 7296.

(56) Chang, Y. H.; Lin, C. T.; Chen, T. Y.; Hsu, C. L.; Lee, Y. H.; Zhang, W. J.; Wei, K. H.; Li, L. J. *Adv. Mater.* **2013**, *25*, 756.

(57) Liao, L.; Zhu, J.; Bian, X. J.; Zhu, L. N.; Scanlon, M. D.; Girault, H. H.; Liu, B. H. *Adv. Funct. Mater.* **2013**, *23*, 5326.

(58) Yan, Y.; Ge, X. M.; Liu, Z. L.; Wang, J. Y.; Lee, J. M.; Wang, X. *Nanoscale* **2013**, *5*, 7768.

(59) Kibsgaard, J.; Jaramillo, T. F.; Besenbacher, F. *Nat. Chem.* **2014**, *6*, 248.

(60) Vrubel, H.; Hu, X. L. *ACS Catal.* **2013**, *3*, 2002.

(61) Merki, D.; Vrubel, H.; Rovelli, L.; Fierro, S.; Hu, X. L. *Chem. Sci.* **2012**, *3*, 2515.

(62) Karunadasa, H. I.; Montalvo, E.; Sun, Y. J.; Majda, M.; Long, J. R.; Chang, C. J. *Science* **2012**, *335*, 698.

(63) Benck, J. D.; Chen, Z. B.; Kuritzky, L. Y.; Forman, A. J.; Jaramillo, T. F. *ACS Catal.* **2012**, *2*, 1916.

(64) Merki, D.; Fierro, S.; Vrubel, H.; Hu, X. L. *Chem. Sci.* **2011**, *2*, 1262.

(65) Vrubel, H.; Merki, D.; Hu, X. L. *Energ. Environ. Sci.* **2012**, *5*, 6136.

(66) Huang, Y. F.; Nielsen, R. J.; Goddard, W. A.; Soriaga, M. P. *J. Am. Chem. Soc.* **2015**, *137*, 6692.

(67) Tran, P. D.; Tran, T. V.; Orio, M.; Torelli, S.; Truong, Q. D.; Nayuki, K.; Sasaki, Y.; Chiam, S. Y.; Yi, R.; Honma, I.; Barber, J.; Artero, V. *Nat. Mater.* **2016**, *15*, 640.

(68) Lassalle-Kaiser, B.; Merki, D.; Vrubel, H.; Gul, S.; Yachandra, V. K.; Hu, X. L.; Yano, J. *J. Am. Chem. Soc.* **2015**, *137*, 314.

(69) Zhang, X. W.; Meng, F.; Mao, S.; Ding, Q.; Shearer, M. J.; Faber, M. S.; Chen, J. H.; Hamers, R. J.; Jin, S. *Energ. Environ. Sci.* **2015**, *8*, 862.

(70) Ding, Q.; Meng, F.; English, C. R.; Caban-Acevedo, M.; Shearer, M. J.; Liang, D.; Daniel, A. S.; Hamers, R. J.; Jin, S. *J. Am. Chem. Soc.* **2014**, *136*, 8504.

(71) Staszak-Jirkovsky, J.; Malliakas, C. D.; Lopes, P. P.; Danilovic, N.; Kota, S. S.; Chang, K. C.; Genorio, B.; Strmcnik, D.; Stamenkovic, V. R.; Kanatzidis, M. G.; Markovic, N. M. *Nat. Mater.* **2016**, *15*, 197.

(72) Ding, Q.; Zhai, J. Y.; Caban-Acevedo, M.; Shearer, M. J.; Li, L. S.; Chang, H. C.; Tsai, M. L.; Ma, D. W.; Zhang, X. W.; Hamers, R. J.; He, H.; Jin, S. *Adv. Mater.* **2015**, *27*, 6511.

(73) Hou, Y. D.; Abrams, B. L.; Vesborg, P. C. K.; Bjorketun, M. E.; Herbst, K.; Bech, L.; Setti, A. M.; Damsgaard, C. D.; Pedersen, T.; Hansen, O.; Rossmeisl, J.; Dahl, S.; Norskov, J. K.; Chorkendorff, I. *Nat. Mater.* **2011**, *10*, 434.

(74) Reece, S. Y.; Hamel, J. A.; Sung, K.; Jarvi, T. D.; Esswein, A. J.; Pijpers, J. J. H.; Nocera, D. G. *Science* **2011**, *334*, 645.

(75) Boettcher, S. W.; Spurgeon, J. M.; Putnam, M. C.; Warren, E. L.; Turner-Evans, D. B.; Kelzenberg, M. D.; Maiolo, J. R.; Atwater, H. A.; Lewis, N. S. *Science* **2010**, *327*, 185.

(76) Boettcher, S. W.; Warren, E. L.; Putnam, M. C.; Santori, E. A.; Turner-Evans, D.; Kelzenberg, M. D.; Walter, M. G.; McKone, J. R.; Brunschwig, B. S.; Atwater, H. A.; Lewis, N. S. *J. Am. Chem. Soc.* **2011**, *133*, 1216.

(77) Kelzenberg, M. D.; Boettcher, S. W.; Petykiewicz, J. A.; Turner-Evans, D. B.; Putnam, M. C.; Warren, E. L.; Spurgeon, J. M.; Briggs, R. M.; Lewis, N. S.; Atwater, H. A. *Nat. Mater.* **2010**, *9*, 368.

(78) McKone, J. R.; Warren, E. L.; Bierman, M. J.; Boettcher, S. W.; Brunschwig, B. S.; Lewis, N. S.; Gray, H. B. *Energ. Environ. Sci.* **2011**, *4*, 3573.

(79) Warren, E. L.; McKone, J. R.; Atwater, H. A.; Gray, H. B.; Lewis, N. S. *Energ. Environ. Sci.* **2012**, *5*, 9653.

(80) Wang, H. P.; Lin, T. Y.; Hsu, C. W.; Tsai, M. L.; Huang, C. H.; Wei, W. R.; Huang, M. Y.; Chien, Y. J.; Yang, P. C.; Liu, C. W.; Chou, L. J.; He, J. H. *ACS Nano* **2013**, *7*, 9325.

(81) Seger, B.; Laursen, A. B.; Vesborg, P. C. K.; Pedersen, T.; Hansen, O.; Dahl, S.; Chorkendorff, I. *Angew. Chem. Int. Edit.* **2012**, *51*, 9128.

(82) Benck, J. D.; Lee, S. C.; Fong, K. D.; Kibsgaard, J.; Sinclair, R.; Jaramillo, T. F. *Adv. Energy Mater.* **2014**, *4*, 1400739.

(83) Morales-Guio, C. G.; Tilley, S. D.; Vrubel, H.; Gratzel, M.; Hu, X. L. *Nat. Commun.* **2014**, *5*, 3059.

(84) Morales-Guio, C. G.; Liardet, L.; Mayer, M. T.; Tilley, S. D.; Gratzel, M.; Hu, X. L. *Angew. Chem. Int. Edit.* **2015**, *54*, 664.

(85) Gao, L.; Cui, Y. C.; Wang, J.; Cavalli, A.; Standing, A.; Vu, T. T. T.; Verheijen, M. A.; Haverkort, J. E. M.; Bakkers, E. P. A. M.; Notten, P. H. L. *Nano Lett.* **2014**, *14*, 3715.

(86) Standing, A.; Assali, S.; Gao, L.; Verheijen, M. A.; van Dam, D.; Cui, Y. C.; Notten, P. H. L.; Haverkort, J. E. M.; Bakkers, E. P. A. M. *Nat. Commun.* **2015**, *6*, 7824.

(87) Britto, R. J.; Benck, J. D.; Young, J. L.; Hahn, C.; Deutsch, T. G.; Jaramillo, T. F. *J. Phys. Chem. Lett.* **2016**, *7*, 2044.

Chapter 2

Efficient Photoelectrochemical Hydrogen Generation Using Heterostructures of Si and Chemically Exfoliated Metallic MoS_2[*]

2.1 Abstract

We report the preparation and characterization of highly efficient and robust photocathodes based on heterostructures of chemically exfoliated metallic 1T-MoS_2 and planar *p*-type Si for solar-driven hydrogen production. Photocurrents up to 17.6 mA/cm^2 at 0 V *vs* reversible hydrogen electrode were achieved under simulated 1 sun irradiation, and excellent stability was demonstrated over long-term operation. Electrochemical impedance spectroscopy revealed low charge transfer resistances at the semiconductor/catalyst and catalyst/electrolyte interfaces, and surface photoresponse measurements also demonstrated slow carrier recombination dynamics and consequently efficient charge carrier separation, providing further evidences for the superior performance. Our results suggest that chemically exfoliated 1T-MoS_2/Si heterostructures are promising earth-abundant alternatives to photocathodes based on noble metal catalysts for solar-driven hydrogen production.

---

[*] This chapter was originally published in *J. Am. Chem. Soc.* **2014**, *136*, 8504. It was prepared in collaboration with Fei Meng, Caroline R. English, Miguel Cabán-Acevedo, Melinda J. Shearer, Dong Liang, Andrew S. Daniel, Robert J. Hamers, and Song Jin* before being adapted here.

2.2 Introduction

Hydrogen, a clean, storable, and high energy density energy carrier, is a promising sustainable alternative for meeting the global energy demand and achieving an environmentally-friendly fuel economy.[1] In the pursuit of utilizing renewable energy to produce hydrogen fuel, solar-driven water-splitting is one of the most promising approaches.[2] This can be achieved by using either a photovoltaics-electrolyzer system or an integrated photoelectrochemical (PEC) system that couples the light harvesting and solar fuel production and enables direct solar-to-hydrogen production.[2] A PEC system has two essential components: a light absorber that generates electron-hole pairs upon illumination and an electrocatalyst that facilitates charge transfer and reduces the overpotential for fuel production. *P*-type silicon (*p*-Si) is an earth-abundant and inexpensive semiconductor with a suitable band gap (1.1 eV) and has been widely utilized as a light absorber in photocathodes.[3] Even though platinum and other noble metals remain the best electrocatalysts for hydrogen evolution reaction (HER),[4] the high cost and scarcity greatly limit their large scale deployment.[1a] The intensive search for earth-abundant, inexpensive and non-toxic catalysts with comparable performance in HER has led to significant progress in the development of new catalysts recently, such as metal alloys,[5] chalcogenides,[6] nitrides,[7] phosphides,[8] borides,[9] carbides.[10] Despite significant progress, most of these new materials have only been investigated as standalone electrocatalysts, and only a few have been integrated into photocathodes. The effective integration of electrocatalysts with light absorbers could potentially be quite challenging because of the semiconductor/catalyst chemical incompatibility and stability issues, induced interfacial defects states and recombination sites, or synthetic difficulties such as control over morphology, coverage and thickness when growing the catalyst directly on the light absorber.[2b] One must also consider suitable band alignment and ensure efficient charge transfer across multiple interfaces. Several photocathodes based on non-noble metal catalysts for solar-driven HER have been recently reported;[5, 11] however, their chemical stability and PEC performance still need to be improved. Developing low-cost photocathodes that could provide high efficiency as well as long-term stability for practical applications remains a significant challenge.

Among the earth-abundant HER catalysts, MoS_2 with a layered crystal structure has shown great promise.[6a-j] Recent report showed that chemically exfoliated metallic 1T-MoS_2 nanosheets display dramatically enhanced catalytic activity compared to as-grown 2H-MoS_2.[6a] A simple *n*-butyl lithium (*n*-BuLi) treatment results in the phase conversion from semiconducting 2H-MoS_2 to metallic 1T-MoS_2, which has more facile electrode kinetics, proliferated active edge sites, and metallic transport.[6a] Built on these advantages, here we demonstrate integrated heterostructures of chemically exfoliated 1T-MoS_2 and planar *p*-Si as efficient and robust photocathodes for PEC hydrogen generation. A high current density of 17.6 mA/cm^2 at 0 V *vs* reversible hydrogen electrode (RHE) and an excellent onset of photocurrent are achieved together with good stability. Electrochemical impedance spectroscopy (EIS) and surface photoresponse (SPR) measurements further explain the superior performance of these 1T-MoS_2/Si photocathodes, making them promising earth-abundant alternatives to noble metal-based systems for solar-driven HER.

2.3 Materials and Methods

2.3.1 *Direct CVD growth of MoS_2 nanostructures onto Si wafers.*

Si wafers with resistivity of 1-2.5 Ω-cm (p-type, B doped, (100) orientation, prime grade, 525 µm thickness, 100 mm diameter, native silicon oxide) were obtained from Silicon Inc. The Si wafers were cut into 7×7 mm^2 pieces for photocathode fabrication and MoS_2 growth. All chemical vapor deposition (CVD) syntheses of MoS_2 were conducted in a home-built CVD setup that consists of a quartz tube (1 inch O.D.) connected to an Ar gas inlet and a vacuum pump with pressure and gas flow controllers, and placed in a tube furnace (Thermal Fisher, Linderberg Blue). In a typical CVD synthesis, alumina combustion boats containing 15 mg molybdenum (V) chloride ($MoCl_5$, 95%) and 60 mg elemental sulfur (99.5 %) were used as reaction precursors and placed outside of the tube furnace, with the $MoCl_5$ boat at more upstream location. Si substrates were first etched with aqueous buffered HF solution (Buffer HF Improved, Transene Inc.) for 30 s to remove the native oxide layer and subsequently rinsed with deionized water and dried with a stream of N_2, and then placed at the center of the tube furnace. The reactor was immediately evacuated and flushed with Ar carrier gas (99.999%) several times. After flushing, the pressure was set to 770 Torr under a steady flow of Ar gas at 125 sccm and the tube furnace was heated to 475 ^oC. The precursor boats were then pushed into the mouth of the furnace (1.5 cm for $MoCl_5$ boat, 4.5 cm for sulfur boat from the edge of the furnace) using a magnet, and the reaction was kept for 3 min before the tube furnace was opened to allow natural cooling of samples under Ar flow.

2.3.2 Synthesis of MoS_2 nanostructures for dropcasting.

The CVD synthesis of MoS_2 nanostructures for dropcasting followed a procedure previously reported by our group.[S1] Slightly different from the aforementioned direct growth of MoS_2 on Si wafers, larger amount of precursors, higher temperature, and longer reaction time were used. In a typical synthesis, 50 mg molybdenum (V) chloride ($MoCl_5$, 95%) and 200 mg elemental sulfur (99.5 %) were used as the precursors, which were then heated to 525 ^oC for 20 min in the same CVD setup to deposit directly on molybdenum foil substrates with other reaction conditions kept the same.

2.3.3 n-Butyl lithium exfoliation treatment.

The Si or Mo foil substrates covered with MoS_2 nanostructures were soaked in 2 mL *n*-butyl lithium (2.7 M in heptane) inside 10 mL vials in the glovebox filled with inert gas, which were then sealed and brought out of the glovebox and heated in an oven to 60 ^oC for 12 h. Dry heptane was used to rinse excess *n*-butyl lithium off the substrates, and the substrates were then soaked in 5 mL deionized water for 10 min for exfoliation. During exfoliation, the MoS_2 nanostructures grown on Mo foil substrates readily delaminated from the substrates into deionized water, and the delaminated materials could then be readily harvested into a water suspension for later use in the dropcasting experiment. For MoS_2 nanostructures grown on Si substrate, in order to prevent delamination and use the integrated MoS_2-Si heterostructures directly for photoelectrode fabrication, the substrates were instead soaked in 5 mL isopropanol with drops of deionized water gradually added to allow mild and controlled exfoliation for 10 min. Finally, the substrates were gently rinsed with deionized water to ensure complete exfoliation. In this way, the MoS_2 film could be well preserved on the Si substrate while successful 2H to 1T phase conversion was still achieved, as confirmed by Raman and X-ray photoelectron spectroscopy (XPS) discussed in the main text (Figure 2.2).

2.3.4 Preparation of MoS_2 suspensions.

The as-grown 2H-MoS_2 nanostructures were first lithiated and exfoliated using the *n*-butyl lithium treatment as discussed above. Then the exfoliated MoS_2 nanosheets water suspension was centrifuged in a tabletop centrifuge (Eppendorf 5415D) at 13,200 rpm for 5 min. After removing the supernatant, the product was resuspended in 2 mL of a mixed solution of isopropanol and deionized water (1:1 volume ratio), and this washing procedure was repeated twice before the exfoliated MoS_2 nanosheets were suspended in 1 mL of isopropanol. The final concentration of MoS_2 in these suspensions harvested from a ~0.2 cm^2 Mo foil substrate was determined by inductively coupled plasma atomic emission spectroscopy (ICP-AES) to be around 1.48×10^{-4} M.

2.3.5 Structural characterization.

Scanning electron microscopy (SEM) was performed using a LEO Supra55 VP microscope operating at 3 kV. Raman spectra were taken using a Thermo Scientific DXR confocal Raman microscope using a 532 nm excitation laser. ICP-AES was measured on Optima 2000 DV (PerkinElmer Inc.) to estimate the loading density of MoS_2 deposited or grown on silicon substrates. A calibration curve of emission intensity as a function of the concentration of the Mo standard solutions was first prepared (Figure A1.3), which was then used for calculating concentration of unknown samples. The samples for ICP-AES analysis were prepared by stripping off the MoS_2 from substrates and sonicating for 30 min. X-ray photoelectron spectroscopy (XPS) was taken on a custom-built XPS system (Phi Electronics, Eden Prairie, MN), that included a model 10-610 Al K_α x-ray source (1486.6 eV photon energy) and a model 10-420 toroidal monochromator. A model 10-360 hemispherical analyzer with a 16-channel detector array was used, which under effective operating conditions had an analyzer resolution of 0.4 eV. Electrons were collected at an emission angle of 45° from the surface normal of the sample. High resolution data was collected for Mo3*d*, S2*p*, O1*s*, and C1*s*. All X-ray photoelectron spectra are shifted so that the adventitious carbon C1*s* peak is at 284.8 eV to make sure the data across samples are aligned and that the samples are not experiencing differential charging effects that may convolute the data.

2.3.6 Electrochemical and photoelectrochemical characterization.

The photoelectrochemical characteristics of various Si and MoS_2/Si photocathodes were measured in a three-electrode configuration under simulated 1 sun irradiation (100 mW/cm^2) supplied by 1 kW Xe short arc lamp solar simulator (Newport Corp., Model 91191; AM1.5G filter) using a Bio-Logic SP-200 potentiostat. The light intensity was calibrated with a Si photodiode (Thorlabs) to generate a photocurrent equal to that at 100 mW/cm^2 light intensity. All measurements were performed in 0.5 M H_2SO_4 electrolyte, using a graphite rod (National Carbon Co., AGKSP Spectroscopic Electrode) as the counter electrode, and Ag/AgCl/1 M KCl (Basi) as the reference electrode, which was calibrated against the reversible hydrogen electrode (RHE) in hydrogen saturated electrolyte with a platinum wire (Kurt J. Lesker, 99.99%; 0.50 mm diameter) as the working electrode. The electrolyte was rapidly stirred to minimize mass transport limitations and remove accumulated hydrogen gas bubbles on the electrode surface, and constantly purged with research-grade H_2 gas (99.999%) to maintain a constant Nernst potential for H^+/H_2 redox couple.

The current density vs potential (J–E) data were measured with a scan rate of 10 mV/s unless otherwise noted, and were not corrected for any uncompensated resistance losses or any other extrinsic losses. Electrochemical impedance spectroscopy (EIS) was performed when the working electrode was biased at a constant potential of +0.235 V vs RHE while sweeping the frequency from 350 kHz to 1 Hz with a 10 mV AC dither. In order to reduce possible complexities at applied bias and large passing currents, we performed the EIS measurements at a bias close to the open circuit voltage. We chose 0.235 V for the Nyquist impedance plots as a bias close to the open circuit voltage for the three photocathodes (taking into account small variation between different photocathodes). We also measured Nyquist impedance plots at several more negative potentials, from which we obtained the same qualitative results. The impedance data were modeled using an equivalent circuit shown in the inset of Figure 2.3B of the main text to yield the fitting parameters shown in Table 2.2. Note that a constant phase element (CPE) was used in the EIS fittings to account for non-ideal behavior in the space charge region. Such non-ideal behavior is likely to be caused by the presence of surface states/interfacial states which results in heterogeneity in time response (i.e. frequency dispersion). This effect could manifest as a surface state capacitance (C_{ss}) or shunting resistance (R_{ss}) which will result in a depression of the semicircle related to silicon. In our study we focus on the analysis of the charge transfer resistances across interfaces, thus we utilized a CPE as a simplification of the complex capacitive response introduced by surface states/interfacial states. The impedance of a CPE element has the form:

$$Z(w) = 1 / (Q\ (wi)\alpha), \text{ where } 0 \leq \alpha \leq 1$$

When $\alpha = 0$ the impedance is that of a pure resistor, while when $\alpha = 1$ the impedance is that of a pure capacitor. Thus, this element can account for the observed frequency dispersion caused by the convoluted effect of competing elements. Surface states/interfacial states on the silicon photocathodes could originate from the presence of silicon oxides before catalyst coating or after exposure to the acidic electrolyte. Silicon is well known to have surface oxides in acidic electrolytes, thus is not uncommon to see reports with circuit fittings containing Csc, Rsc, Css and Rss, or simplified models using a CPE instead. The study of the space charge and surface state capacitance will require more extensive work which is outside of the scope of this manuscript.

2.4 Results and Discussion

The simplest approach to assess the viability of 1T-MoS_2/Si heterostructures for PEC hydrogen generation is directly dropcasting 1T-MoS_2 nanosheets suspensions onto Si. We prepared 1T-MoS_2 suspensions by chemically exfoliating MoS_2 nanoflakes synthesized following the chemical vapor deposition (CVD) method we previously reported[6a] and harvesting the delaminated 1T-MoS_2 nanosheets, then dropcasting them onto pre-assembled planar *p*-Si photocathodes (resistivity 1-2.5 Ω-cm) that were freshly etched in buffered HF (see Figure A1.1 and A1.2 for SEM and Raman characterization). The photocurrent density-potential (J-E) data were collected using a three-electrode configuration in 0.5 M H_2SO_4 under simulated 1 sun irradiation (100 mW/cm^2) on Si photocathodes with increasing amount of 1T-MoS_2 suspension. Figure 2.1A shows that application of as little as 2 μL of 1T-MoS_2 suspension could already significantly improve both the onset of photocurrent as well as the current density from those of bare *p*-Si. Gradually increasing the amount of the 1T-MoS_2 suspensions further shifted the onset of photocurrent to an even more positive value of +0.23 V *vs* RHE (compared to –0.14 V *vs* RHE for bare Si), and improved the current density at 0 V *vs* RHE to 8.5 mA/cm^2, before it reached a plateau and started to slightly decrease (Figure 2.1B, blue trace). While the catalytic activity improves with increasing catalyst loading, the overall performance can be reduced due to more light being blocked by MoS_2, as reflected in the decreasing limiting current density (red curve in Figure 2.1B). The optimal volume of MoS_2 suspension was shown to be 14 μL, corresponding to a loading density of ~2.76 μg/cm^2 estimated by inductively coupled plasma atomic emission spectroscopy (ICP-AES) (Figure A1.3 and Table A2.1). As a comparison, the best current density at 0 V *vs* RHE obtained for Si photocathodes dropcasted with 2H-MoS_2 suspension was only 2.3 mA/cm^2, much lower than that of 1T-MoS_2 (the highest observed was 9.2 mA/cm^2). Nevertheless, the same trend of peaking performance was observed as well (Figure A1.4).

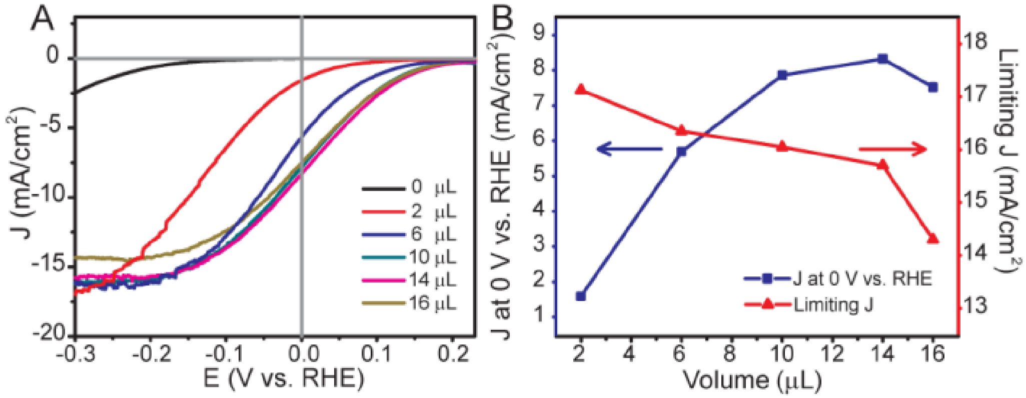

Figure 2.1. (A) J−E curve of *p*-Si photocathodes with different volume of dropcasted 1T-MoS_2 suspensions measured under simulated 1 sun irradiation. (B) Current density at 0 V *vs* RHE and limiting current density as a function of 1T-MoS_2 suspensions volume.

With the promising result obtained from the simple dropcasting approach, we expect to further improve the PEC performance by directly growing MoS_2 onto Si to form a higher-quality interface between MoS_2 and Si. We developed a modified CVD synthesis, in which less precursors, lower temperature and shorter reaction time (see SI for details) were employed than our previous protocol.[6a] This yielded a thin film of MoS_2 (40-80 nm thick) uniformly covering the Si substrate with sparse MoS_2 flakes standing out of the film (Figure 2.2A and inset). The amount of MoS_2 grown on Si was estimated to be ~2.64 $\mu g/cm^2$ by ICP-AES (Table 2.1). The as-grown 2H-MoS_2 was then converted to metallic 1T-MoS_2 by *n*-BuLi treatment, and the phase change was confirmed by Raman and X-ray photoelectron spectroscopy (XPS). Characteristic Raman shifts at 387, 412, and 456 cm^{-1} were observed for as-grown 2H-MoS_2 samples, which correspond to in-plane E^1_{2g}, out-of plane A_{1g} and longitudinal acoustic phonon modes, respectively.[12] After the *n*-BuLi treatment, three new shifts at 150, 219, and 327 cm^{-1} associated with the new vibration modes J_1, J_2 and J_3 of 1T-MoS_2 were observed.[6a, b, 12] The significantly reduced intensity of 387 and 412 cm^{-1} shifts indicates that the content of 2H polymorph has been largely reduced (Figure 2.2C). We will simply use 1T-MoS_2 to refer to these chemically exfoliated samples thereafter. High-resolution XPS further revealed the lower binding energy of the Mo3*d* (Figure 2.2D) and S2*p* (Figure 2.2E) edges for the 1T-MoS_2. The $Mo3d_{5/2}$ and $Mo3d_{3/2}$ peaks shifted from ~229.5 eV and ~232.2 eV for the 2H-MoS_2 to ~228.1 eV and ~231.1 eV for the 1T-MoS_2, consistent with previous reports.[6b] Scanning electron microscopy (SEM) images of 1T-MoS_2/Si (Figure 2.2B) revealed that the MoS_2 thin film maintained after the *n*-BuLi treatment became much more disordered and compressed compared to the as-grown 2H-MoS_2. The *n*-BuLi treatment was also performed on bare Si as a control experiment, and no noticeable change was detected either by SEM or in its PEC performance (Figure A1.5).

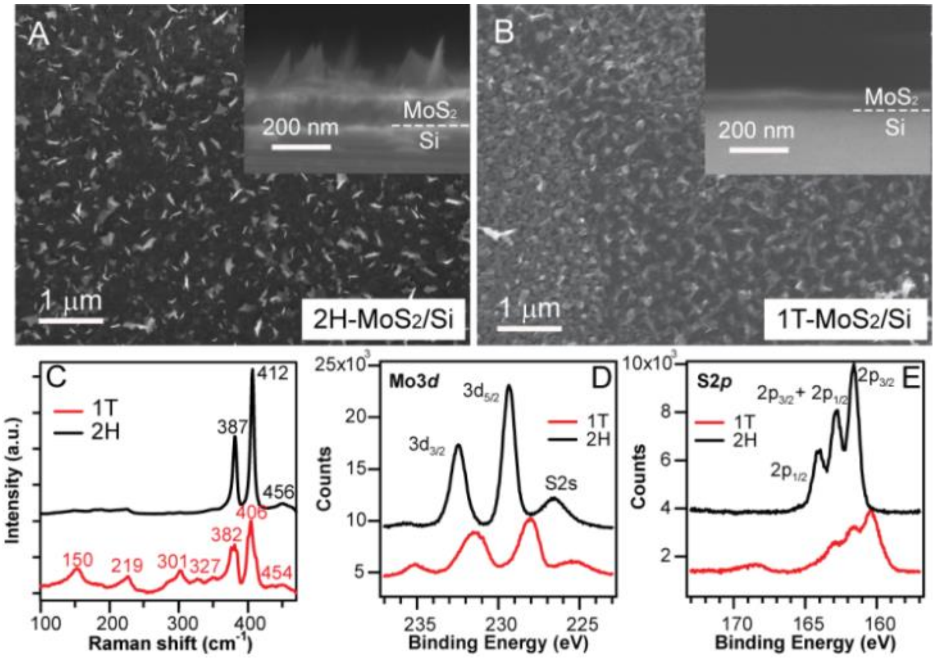

Figure 2.2. Comparison of top-down and cross-sectional (insets) SEM images of (A) 2H- and (B) 1T-MoS_2/Si, Raman spectra (C), high resolution XPS of Mo3*d* (D) and S2*p* (E) regions for 2H- (black) and 1T- (red) MoS_2 on Si substrates.

Table A2.1. The amount of MoS_2 loading on representative CVD 2H-MoS_2/Si, CVD 1T-MoS_2/Si, and dropcasted 1T-MoS_2/Si photocathodes determined by ICP-AES.

Photoelectrode	Dropcast 1T	CVD 1T	CVD 2H
Concentration (μg/cm^2)	2.76 (for 14 μL)	2.18	2.64

The PEC performance of as-grown 2H-MoS_2/Si and exfoliated 1T-MoS_2/Si heterostructures measured in 0.5 M H_2SO_4 under simulated 1 sun irradiation were compared in Figure 2.3A. Compared with bare Si photocathode which has an onset of photocurrent at –0.14 V *vs* RHE, the as-grown 2H-MoS_2/Si photocathode showed a shift in the onset of photocurrent to around +0.23 V *vs* RHE with a current density of 4.2 mA/cm^2 at 0 V *vs* RHE. The band bending of Si caused by 2H-MoS_2 is also shown by a solid-state diode measurement (Figure 2.4). A further substantial enhancement was observed for the 1T-MoS_2/Si. The onset of photocurrent shifted to +0.25 V *vs* RHE and the current density at 0 V *vs* RHE increased to 17.6 mA/cm^2, which is to our knowledge the highest reported photocurrent density for non-noble metal catalysts on planar *p*-Si photocathodes. Recently reported amorphous MoS_x on n^+p Si[11d] and Cu_2O[11e] photocathodes showed higher onset of photocurrent because of the buried junction and high built-in potential. However, the onset of photocurrent achieved here is already comparable to that of previously reported Pt on *p*-Si photocathode,[11f] and the current density achieved in the 1T-MoS_2 heterostructures is also higher than the amorphous MoS_x heterostructures. The observed fill factor is likely still hindered by non-optimal MoS_2/Si interface, but comparable to other reported *p*-Si photocathodes with non-noble metal catalysts.[5a, 11a, b, 11f] Gas chromatography was used to measure generated hydrogen and a Faradaic efficiency close to 100% was obtained, confirming that the generated photocurrent is indeed due to hydrogen evolution (Figure 2.5). Compared with dropcasted 1T-MoS_2/Si, the direct CVD grown 1T-MoS_2/Si photocathode had a more positive onset of photocurrent (0.25 V *vs* 0.23 V, both relative to RHE), a higher current density at 0 V *vs.* RHE (17.6 mA/cm^2 *vs* 9.2 mA/cm^2), and a higher limiting current density (26.7 mA/cm^2 *vs* 14.3 mA/cm^2).

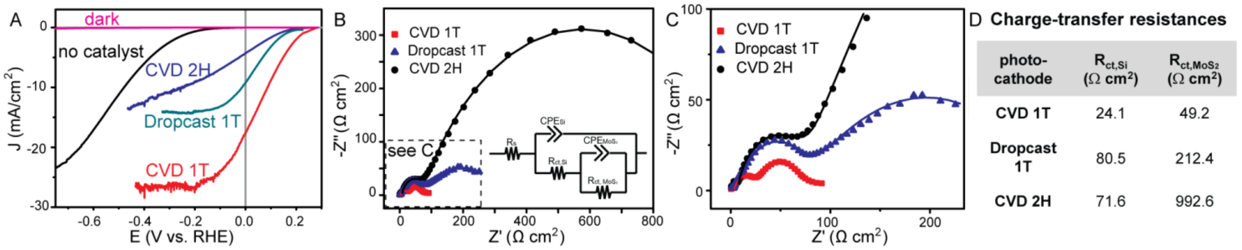

Charge-transfer resistances

photo-cathode	$R_{ct,Si}$ (Ω cm²)	R_{ct,MoS_2} (Ω cm²)
CVD 1T	24.1	49.2
Dropcast 1T	80.5	212.4
CVD 2H	71.6	992.6

Figure 2.3. (A) J-E curves, (B, C) Nyquist impedance plots and (D) the fitted charge-transfer resistance values of a CVD grown 2H-MoS_2/Si photocathode (CVD 2H), a CVD grown 1T-MoS_2/Si photocathode (CVD 1T), and a dropcasted 1T-MoS_2/Si photocathode (dropcast 1T) measured in 0.5 M H_2SO_4 under simulated 1 sun irradiation. The J-E curve of a bare Si photocathode is also shown in A as a comparison. The dashed box in panel B is magnified in C. The solid line traces correspond to the fitting using the equivalent circuit in the inset of panel B.

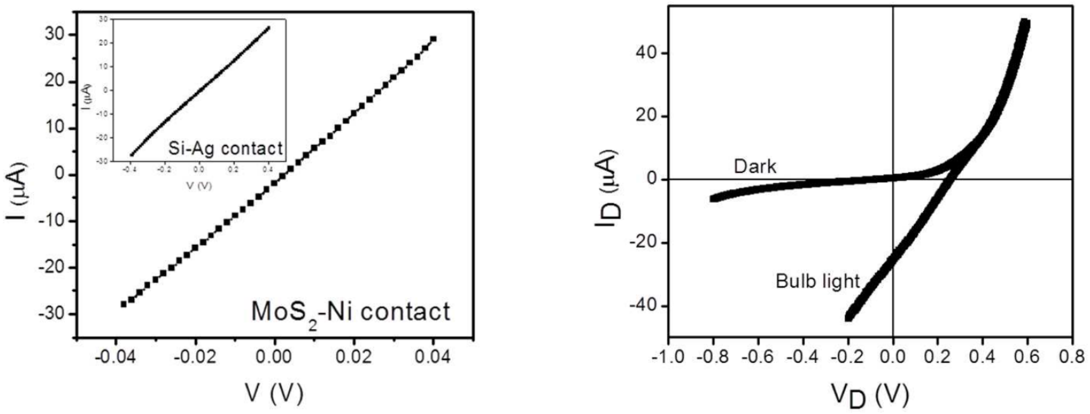

Figure 2.4. Characterization of the solid-state diode made from CVD grown MoS_2/Si heterostructure. I-V curves between two front Ni contacts and between two back Ag contacts both show a linear relationship, indicating the formation of ohmic contacts in both cases. We observed a diode behavior with a junction barrier of ~0.26 V from the I-V curve measured in dark, and a V_{oc} of the similar voltage when illuminated under weak bulb light. Note that no HF etching was performed when measuring the diode, therefore there might still be native silicon oxide layer formed at the interface between Si and MoS_2, making the measured junction barrier smaller than the actual value. On the other hand, for the solid state diode there is no overpotential associated with evolution of hydrogen, therefore the observed V_{oc} here appears to be similar to the onset of photocurrent in photoelectrochemical measurements.

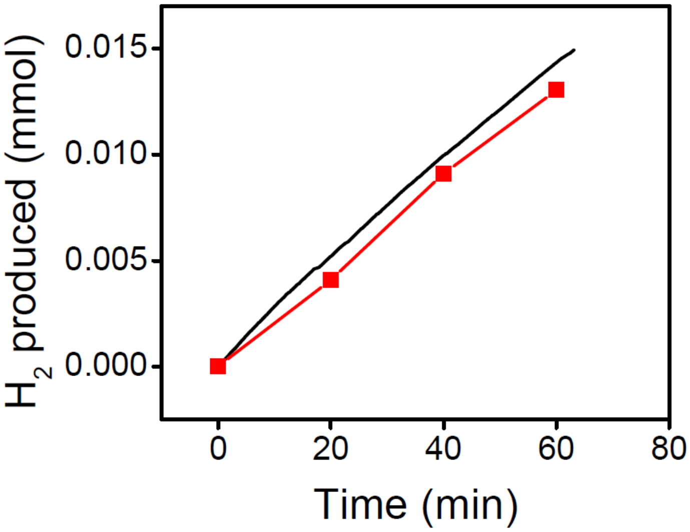

Figure 2.5. Theoretical (black curve) and experimental (red data points) amount of generated H_2, showing a Faradaic efficiency close to 100%. The initial induction time is attributed to the initially produced H_2 dissolving in the air-saturated electrolyte.

To better understand the PEC performance, we performed EIS to elucidate the charge transfer resistances in different photocathodes. Nyquist impedance plots for these photocathodes measured under illumination at 0.235 V *vs* RHE all display two distinguishable semicircles (Figure 2.3B, 2.3C). Following a reported example of catalyst-semiconductor system,[13] the data can be fitted to an equivalent circuit (Figure 2.3B inset) consisting of constant phase elements (CPE) associated with the semiconductor Si (CPE_{Si}) and the catalyst MoS_2 (CPE_{MoS2}), and charge transfer resistances from Si to MoS_2 ($R_{ct,Si}$) and from MoS_2 to the redox couple in electrolyte ($R_{ct, MoS2}$). The first semicircle on the left in the Nyquist plot yields $R_{ct,Si}$, which is a good indicator of the coupling between the light absorber (Si) and the catalyst (MoS_2); whereas the second semicircle on the right leads to $R_{ct, MoS2}$, which usually reflects the catalytic activity of the material.

The charge transfer resistances obtained from the fittings are summarized in Figure 2.3D with other parameters shown in Table A2.2. The charge transfer resistance from MoS_2 to electrolyte ($R_{ct,MoS2}$) of the CVD 1T-MoS_2/Si (49.2 Ω cm^2) is dramatically lower than that of the CVD 2H-MoS_2/Si (992.6 Ω cm^2), confirming the facile electrode kinetics of 1T-MoS_2/Si and further proving that the 1T phase is indeed much more catalytically active towards HER. The charge transfer resistance from Si to MoS_2 ($R_{ct,Si}$) of the CVD 1T-MoS_2/Si (24.1 Ω cm^2) is also smaller than that of the CVD 2H-MoS_2/Si (71.6 Ω cm^2), likely due to more available electronic states in the metallic 1T phase relative to the semiconducting 2H phase.

Table A2.2. Fitted values of all elements in the equivalent circuit for the Nyquist impedance plots of CVD 2H-MoS_2/Si, CVD 1T-MoS_2/Si, and dropcasted 1T-MoS_2/Si photoelectrodes.

Photoelectrode	Rs (Ω cm^2)	Q1 (F $S^{\alpha-1}$)	α1	Q2 (F $S^{\alpha-1}$)	α2
CVD 1T/Si	3.2	2.8×10^{-6}	0.74	8.8×10^{-5}	0.70
Dropcast 1T/Si	5.2	3.4×10^{-6}	0.72	3.2×10^{-4}	0.56
CVD 2H/Si	6.3	2.2×10^{-7}	0.85	1.3×10^{-5}	0.70

Furthermore, the direct CVD grown 1T-MoS_2/Si heterostructure exhibits a much lower charge transfer resistance from Si to MoS_2 (24.1 Ω cm^2) than the dropcasted 1T-MoS_2/Si (80.5 Ω cm^2), which confirms that the CVD grown MoS_2/Si heterostructure has a higher quality interface between the light absorber and catalyst. This is in good agreement with the observed superior performance of the CVD 1T-MoS_2/Si and highlights the benefits of direct CVD growth of catalysts on photocathodes for effective PEC system integration. Additionally, the impeded charge transfer from Si to MoS_2 as well as unoptimized MoS_2 morphology in the dropcasted 1T-MoS_2/Si result in larger $R_{ct, MoS2}$ (212.4 Ω cm^2) than that of the CVD 1T-MoS_2/Si (49.2 Ω cm^2). Overall, the CVD 1T-MoS_2/Si has the smallest $R_{ct, MoS2}$, followed by dropcasted 1T-MoS_2/Si and then CVD 2H-MoS_2/Si, which agrees with the trend of their J-E performance.

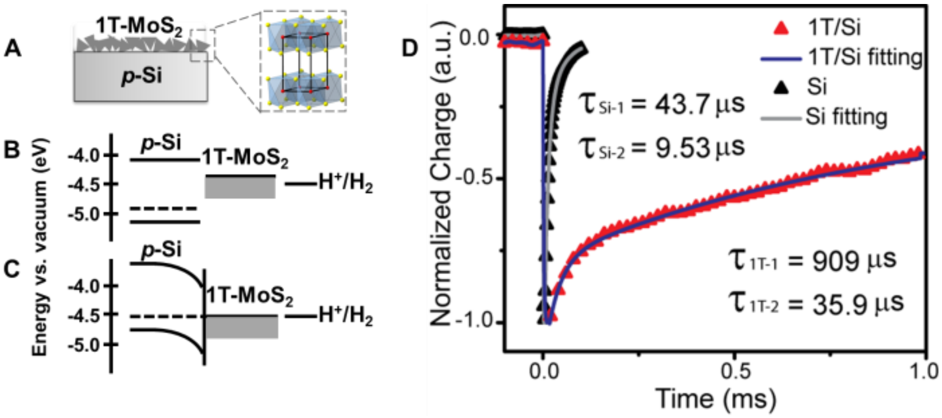

Figure 2.6. (A) Illustration of 1T-MoS2 on *p*-Si. Schematic band energy diagram of *p*-Si, 1T-MoS2 and H^+/H_2 redox couple at 0 V *vs* RHE in the dark before (B) and after (C) equilibrium. (D) Integrated TR-SPR spectra and corresponding biexponential fittings of 1T-MoS2/Si (red and blue) and Si (black and gray).

We further used time-resolved SPR spectroscopy to investigate the dynamics of the photo-generated charge carriers at the surface of the best performing CVD grown 1T-MoS_2/Si heterostructure. SPR can reveal information about the number of generated charges, charge separation at the interface as well as carrier lifetime.[14] Both bare *p*-Si and 1T-MoS_2/Si were measured in 0.5 M H_2SO_4 in a capacitor-like arrangement after illuminated with a brief laser pulse. The recorded transient photocurrents (Figure 2.7) as well as integrated charges (Figure 2.6D) both show a rise of signal followed by a decay that can be fit to a multiple exponential function. For bare Si, negative signal was observed, indicating electrons accumulating at the surface, which is typical for a *p*-type material with downward band bending.[15] A biexponential fitting for the Si sample measured at 750 nm revealed time constants of τ_1 and τ_2 to be 9.53 μs and 43.7 μs, respectively, consistent with the reported value for *p*-Si at this doping level.[16] The 1T-MoS_2/Si heterostructure also exhibited negative signal implying similar downward band bending with *p*-Si, which is consistent with the band position[17] and band alignment between *p*-Si and 1T-MoS_2 (Figure 2.6B, 2.6C). A similar biexponential fitting yielded time constants of 35.9 μs and 909 μs, which shows that the 1T-MoS_2 layer dramatically increases the charge carrier lifetime of Si. This is likely due to the fast and irreversible electron transfer from Si to 1T-MoS_2, leaving holes behind in Si. This fast charge separation and slow charge recombination across the MoS_2/Si interface likely contribute to the efficient utilization of electrons for hydrogen evolution, and enable the superior PEC performance. Moreover, time-resolved microwave conductivity was also used to provide further insight to the carrier dynamics (Figure 2.8).

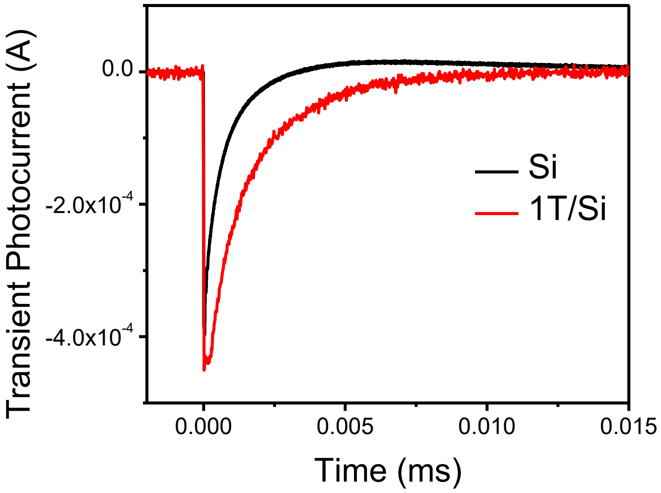

Figure 2.7. Transient photocurrent spectra of a CVD 1T-MoS_2/Si (red) and a Si (black) photocathodes measured in 0.5 M sulfuric acid at 750 nm.

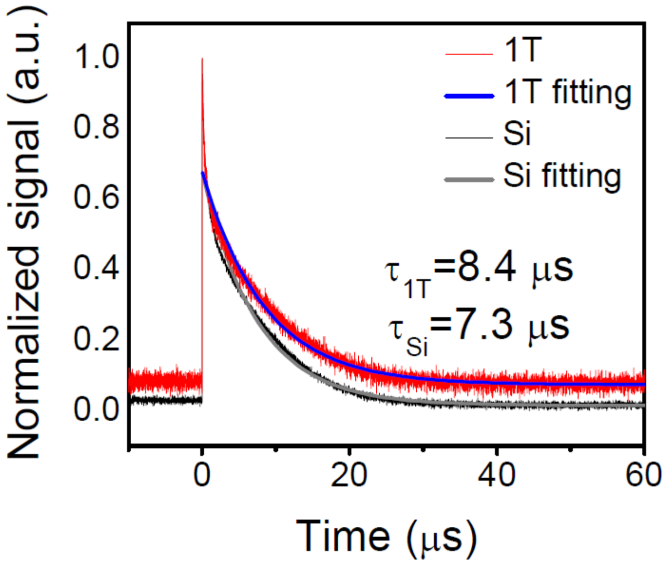

Figure 2.8. Time-resolved microwave conductivity measurements of Si (black and gray) and CVD grown 1T-MoS_2/Si heterostructure (red and blue) and the fittings to determine the carrier lifetime.

The TRMC and TR-SPR results can be understood based on the nature of these methods and the samples probed. Microwave conductivity measurements probe the change in the conductivity of the sample by measuring the change of reflected microwave power. TRMC effectively measures the dynamics of the bulk carriers. In contrast, SPR measures the transient change in potential at the outermost surface of the sample. The SPR measurements show that the 1T-MoS_2 sample traps electrons. The electron transfer from Si to MoS_2 leads to accumulation of electrons in 1T-MoS_2, and because of the electron-hole separation, the charge recombination across the MoS_2/Si interface is slowed down, and therefore the decay of electrons is much slower compared to that of bare Si surface. These data from both measurements are consistent with a model in which photo-excitation of Si induces excess electrons and holes, with some of the electrons transferring to the 1T-MoS_2 catalyst and being trapped at the surface.

Although 1T-MoS_2 is the thermodynamically metastable phase, these 1T-MoS_2/Si photocathodes remain stable and catalytically active over long-term operation. A chronoamperometry test of one CVD 1T-MoS_2/Si photocathode was performed at 0 V *vs* RHE over 3 h (Figure 2.9), and a 23% decrease in current density was observed, which is attributed to *p*-Si being oxidized during measurement as the current density could be readily recovered to its initial value after a buffered HF etch. Compared to a bare Si photocathode measured at the same condition,[11f] the degradation here has already been largely suppressed, suggesting that the MoS_2 coating might help to alleviate Si oxidation. Repeated scans of a CVD 1T-MoS_2/Si photocathode (Figure 2.10) and a dropcasted 1T-MoS_2/Si photocathode (Figure 2.11) also showed negligible decrease in performance. Furthermore, the current density at 0 V *vs* RHE of a CVD 1T-MoS_2/Si photocathode was monitored periodically over 70 days and no noticeable decrease in performance was observed (Figure 2.12).

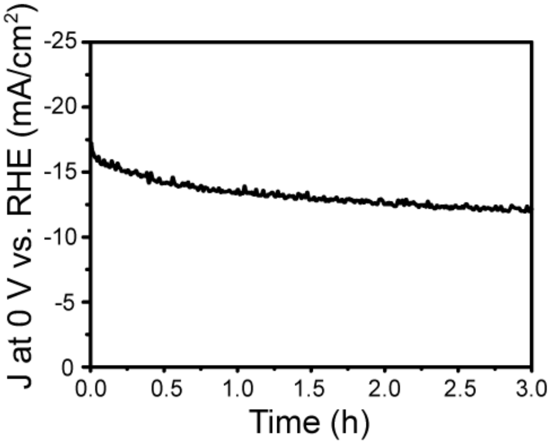

Figure 2.9. Chronoamperometry measurement of a CVD 1T-MoS$_2$/Si photocathode measured at 0 V *vs* RHE under illumination over 7200 s.

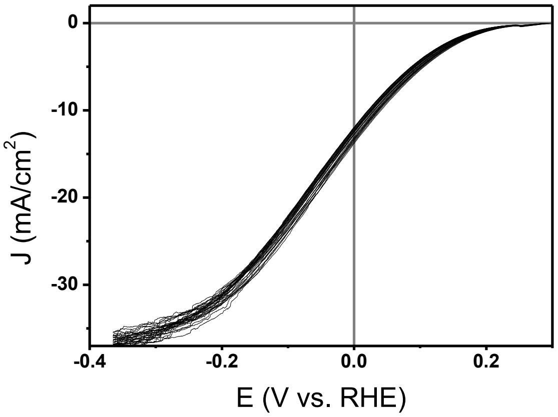

Figure 2.10. Thirty repeated J-E scans of a CVD grown 1T-MoS$_2$/Si photocathode measured with a scan rate of 50 mV/s under simulated 1 sun irradiation in 0.5 M sulfuric acid.

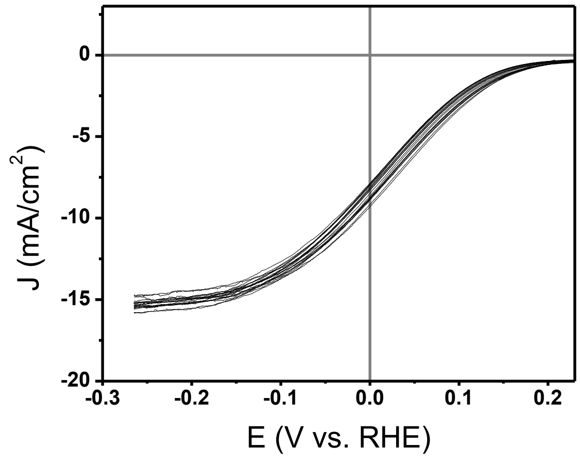

Figure 2.11. Twenty repeated scans of a dropcasted 1T-MoS_2/Si photocathode measured with a scan rate of 50 mV/s under simulated 1 sun irradiation in 0.5 M sulfuric acid.

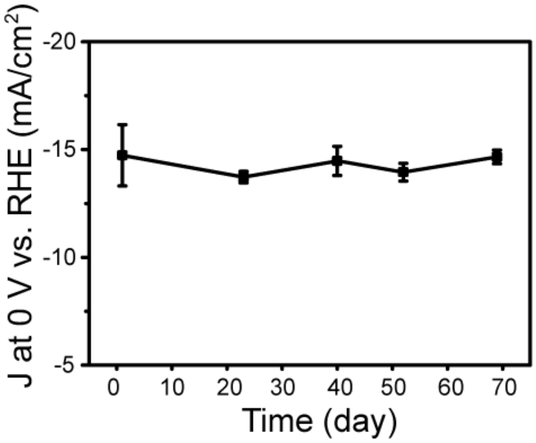

Figure 2.12. The current density at 0 V *vs* RHE for a representative CVD grown 1T-MoS_2/Si photocathode periodically monitored over seventy days.

2.5 Conclusions

In summary, we have demonstrated that heterostructures of chemically exfoliated 1T-MoS_2 on planar *p*-Si behave as efficient and robust photocathodes for solar-driven HER, exhibiting an excellent onset of photocurrent, and the highest current density at 0 V *vs* RHE for planar *p*-Si photocathodes with non-noble metal catalysts. EIS measurements demonstrated that the excellent performance of the CVD grown 1T-MoS_2/*p*-Si photocathodes can be attributed to small charge transfer resistances across the semiconductor/catalyst and catalyst/electrolyte interfaces. SPR measurement also showed slow carrier recombination dynamics and efficient charge carrier separation. The excellent performance and stability make 1T-MoS_2/Si heterostructures promising alternatives to noble metal catalyst-based photocathodes for solar-driven hydrogen production, and will stimulate further explorations of analogous metallic 1T polymorphs of layered metal chalcogenides for PEC solar energy conversion.

2.6 References

(1) (a) Lewis, N. S.; Nocera, D. G. *Proc. Natl. Acad. Sci. U.S.A.* **2006,** *103*, 15729.

(b) Turner, J. A. *Science* **2004,** *305,* 972.

(2) (a) Walter, M. G.; Warren, E. L.; McKone, J. R.; Boettcher, S. W.; Mi, Q. X.; Santori, E. A.; Lewis, N. S. *Chem. Rev.* **2010,** *110,* 6446.

(b) McKone, J. R.; Lewis, N. S.; Gray, H. B. *Chem. Mater.* **2014,** 26, 407.

(3) (a) Reece, S. Y.; Hamel, J. A.; Sung, K.; Jarvi, T. D.; Esswein, A. J.; Pijpers, J. J. H.; Nocera, D. G. *Science* **2011,** *334,* 645.

(b) Boettcher, S. W.; Spurgeon, J. M.; Putnam, M. C.; Warren, E. L.; Turner-Evans, D. B.; Kelzenberg, M. D.; Maiolo, J. R.; Atwater, H. A.; Lewis, N. S. *Science* **2010,** *327,* 185.

(c) Boettcher, S. W.; Warren, E. L.; Putnam, M. C.; Santori, E. A.; Turner-Evans, D.; Kelzenberg, M. D.; Walter, M. G.; McKone, J. R.; Brunschwig, B. S.; Atwater, H. A.; Lewis, N. S. *J. Am. Chem. Soc.* **2011,** *133,* 1216.

(4) Khaselev, O.; Turner, J. A. *Science* **1998,** *280,* 425.

(5) (a) McKone, J. R.; Warren, E. L.; Bierman, M. J.; Boettcher, S. W.; Brunschwig, B. S.; Lewis, N. S.; Gray, H. B. *Energy Environ. Sci.* **2011,** *4,* 3573.

(b) Warren, E. L.; McKone, J. R.; Atwater, H. A.; Gray, H. B.; Lewis, N. S. *Energy Environ. Sci.* **2012,** *5,* 9653.

(6) (a) Lukowski, M. A.; Daniel, A. S.; Meng, F.; Forticaux, A.; Li, L. S.; Jin, S. *J. Am. Chem. Soc.* **2013,** *135,* 10274.

(b) Voiry, D.; Salehi, M.; Silva, R.; Fujita, T.; Chen, M. W.; Asefa, T.; Shenoy, V. B.; Eda, G.; Chhowalla, M. *Nano Lett.* **2013,** *13,* 6222.

(c) Wang, H.; Lu, Z.; Xu, S.; Kong, D. S.; Cha, J. J.; Zheng, G.; Hsu, P.; Yan, K.; Bradshaw, D.; Prinz, F. B.; Cui, Y. *Proc. Natl. Acad. Sci. U.S.A.* **2013,** *110,* 19701.

(d) Li, Y. G.; Wang, H. L.; Xie, L. M.; Liang, Y. Y.; Hong, G. S.; Dai, H. J. *J. Am. Chem. Soc.* **2011,** *133,* 7296.

(e) Kibsgaard, J.; Chen, Z. B.; Reinecke, B. N.; Jaramillo, T. F. *Nat. Mater.* **2012,** *11,* 963.

(f) Laursen, A. B.; Kegnaes, S.; Dahl, S.; Chorkendorff, I. *Energy Environ. Sci.* **2012,** *5,* 5577.

(g) Voiry, D.; Yamaguchi, H.; Li, J. W.; Silva, R.; Alves, D. C. B.; Fujita, T.; Chen, M. W.; Asefa, T.; Shenoy, V. B.; Eda, G.; Chhowalla, M. *Nat. Mater.* **2013,** *12,* 850.

(h) Merki, D.; Fierro, S.; Vrubel, H.; Hu, X. L. *Chem. Sci.* **2011,** *2,* 1262.

(i) Merki, D.; Hu, X. L. *Energy Environ. Sci.* **2011,** *4,* 3878.

(j) Merki, D.; Vrubel, H.; Rovelli, L.; Fierro, S.; Hu, X. L. *Chem. Sci.* **2012,** *3,* 2515.

(k) Lukowski, M. A.; Daniel, A. S.; English, C. R.; Meng, F.; Forticaux, A.; Hamers, R. J.; Jin, S. *Energy Environ. Sci.* **2014,** *7,* 2608.

(7) (a) Chen, W. F.; Sasaki, K.; Ma, C.; Frenkel, A. I.; Marinkovic, N.; Muckerman, J. T.; Zhu, Y. M.; Adzic, R. R. *Angew. Chem., Int. Ed.* **2012,** *51,* 6131.

(b) Cao, B.; Veith, G. M.; Neuefeind, J. C.; Adzic, R. R.; Khalifah, P. G. *J. Am. Chem. Soc.* **2013,** *135,* 19186.

(8) Popczun, E. J.; McKone, J. R.; Read, C. G.; Biacchi, A. J.; Wiltrout, A. M.; Lewis, N. S.; Schaak, R. E. *J. Am. Chem. Soc.* **2013,** *135,* 9267.

(9) Vrubel, H.; Hu, X. L. *Angew. Chem., Int. Ed.* **2012,** *51,* 12703.

(10) Chen, W. F.; Wang, C. H.; Sasaki, K.; Marinkovic, N.; Xu, W.; Muckerman, J. T.; Zhu, Y.; Adzic, R. R. *Energy Environ. Sci.* **2013,** *6,* 943.

(11) (a) Hou, Y. D.; Abrams, B. L.; Vesborg, P. C. K.; Bjorketun, M. E.; Herbst, K.; Bech, L.; Setti, A. M.; Damsgaard, C. D.; Pedersen, T.; Hansen, O.; Rossmeisl, J.; Dahl, S.; Norskov, J. K.; Chorkendorff, I. *Nat. Mater.* **2011,** *10,* 434.

(b) Berglund, S. P.; He, H.; Chemelewski, W. D.; Celio, H.; Dolocan, A.; Mullins, C. B. *J. Am. Chem. Soc.* **2014,** *136,* 1535.

(c) Tran, P. D.; Pramana, S. S.; Kale, V. S.; Nguyen, M.; Chiam, S. Y.; Batabyal, S. K.; Wong, L. H.; Barber, J.; Loo, *J. Chem.-Eur. J.* **2012,** *18,* 13994.

(d) Seger, B.; Laursen, A. B.; Vesborg, P. C. K.; Pedersen, T.; Hansen, O.; Dahl, S.; Chorkendorff, I. *Angew. Chem., Int. Ed.* **2012,** *51,* 9128.

(e) Morales-Guio, C. G.; Tilley, S. D.; Vrubel, H.; Gratzel, M.; Hu, X. L. *Nat. Commun.* **2014,** *5*, 3059.

(f) Sim, U.; Yang, T. Y.; Moon, J.; An, J.; Hwang, J.; Seo, J. H.; Lee, J.; Kim, K. Y.; Lee, J.; Han, S.; Hong, B. H.; Nam, K. T. *Energy Environ. Sci.* **2013,** *6,* 3658.

(g) Sun, Y.; Liu, C.; Grauer, D. C.; Yano, J.; Long, J. R.; Yang, P.; Chang, C. J. *J. Am. Chem. Soc.* **2013,** *135*, 17699.

(12) Sandoval, S. J.; Yang, D.; Frindt, R. F.; Irwin, *J. C. Phys. Rev. B* **1991,** *44,* 3955.

(13) Klahr, B.; Gimenez, S.; Fabregat-Santiago, F.; Bisquert, J.; Hamann, T. W. *J. Am. Chem. Soc.* **2012,** *134*, 16693.

(14) Kronik, L.; Shapira, Y. *Surf. Sci. Rep.* **1999,** *37,* 1.

(15) (a) Mahrov, B.; Boschloo, G.; Hagfeldt, A.; Dloczik, L.; Dittrich, T. *Appl. Phys. Lett.* **2004,** *84,* 5455.

(b) Li, L. S.; Yu, Y. H.; Meng, F.; Tan, Y. Z.; Hamers, R. J.; Jin, S. *Nano Lett.* **2012,** *12*, 724.

(c) Caban-Acevedo, M.; Faber, M. S.; Tan, Y. Z.; Hamers, R. J.; Jin, S. *Nano Lett.* **2012,** *12*, 1977.

(16) Tyagi, M. S.; Vanoverstraeten, R. *Solid-State Electron.* **1983,** *26,* 577.

(17) Yun, J. M.; Noh, Y. J.; Yeo, J. S.; Go, Y. J.; Na, S. I.; Jeong, H. G.; Kim, J.; Lee, S.; Kim, S. S.; Koo, H. Y.; Kim, T. W.; Kim, D. Y. *J. Mater. Chem. C* **2013,** *1,* 3777.

Chapter 3

Designing Efficient Solar-Driven Hydrogen Evolution Photocathodes Using Semi-Transparent MoQ_xCl_y (Q=S, Se) Catalysts on Si Micropyramids[*]

3.1 Abstract

Silicon micropyramids with n^+pp^+ junctions are demonstrated as efficient absorbers for integrated solar-driven photoelectrochemical hydrogen production systems, enabling significant improvements in both photocurrent and onset potential. When conformally coated with MoS_xCl_y – a catalyst that has excellent catalytic activity toward hydrogen evolution reaction and high optical transparency – the highest photocurrent density for Si-based photocathodes with earth-abundant catalysts is achieved.

---

[*] This chapter was originally published in *Advanced Materials* **2015**, *27*, 6511. It was prepared in collaboration with Jianyuan Zhai, Miguel Cabán-Acevedo, Melinda J. Shearer, Linsen Li, Hung-Chih Chang, Meng-Lin Tsai, Dewei Ma, Xingwang Zhang, Robert J. Hamers, Jr-Hau He, Song Jin* before being adapted here.

3.2 Introduction

To meet the growing global demand for renewable energy, water splitting using photoelectrochemical (PEC) devices is a promising approach to store solar energy in the form of a sustainable energy carrier such as hydrogen.[1-4] Two components are essential in a water splitting PEC device to achieve efficient solar-to-chemical fuel production:[4, 5] a semiconductor (light absorber) that absorbs solar light and a catayst that enhances the reaction kinetics.[6] P-type Si has been widely employed in tandem PEC systems as the photocathode for hydrogen evolution reaction (HER) because of its earth abundance and suitable bandgap.[7-10] However, one challenge of utilizing p-type silicon for PEC-HER is its intrinsic low photovoltage, which is limited by the Si/liquid junction.[10] N^+p Si can boost the photovoltage by replacing the Si/liquid junction with a built-in p-n junction.[9, 10] In cases where the band alignment is influenced by the catalyst, the built-in p-n junction could also remove the constraints placed on the catalysts used in this system.[10] Studies have further shown that adding an additional p^+ layer on the back of n^+p Si could facilitate majority carrier collection and lead to improved fill factor and device performance.[11]

Besides large photovoltage, high photocurrent is another prerequisite for highly efficient PEC devices. Both the light harvesting properties of absorber and the optical transparency of catalysts deposited on absorber have significant impacts on the photocurrent.[5, 12, 13] To improve the insufficient light trapping ability of planar Si, nano- and microstructuring of Si have been investigated.[9, 14-16] However, higher density of surface states and faster recombination rates simultaneously observed with increased surface area in Si nano- and microwire-based photocathodes prevented significant gains in efficiency so far.[9, 10, 17, 18] Alternatively, Si micropyramid (MP)-based solar cells have been shown to exhibit high efficiency because of the omnidirectional broad band light-trapping ability with little recombination loss,[19] which makes them uniquely suited for PEC-HER light absorbers. Herein we specifically design Si MPs with a favorable built-in n^+pp^+ junction as novel light absorbers for PEC-HER photocathodes, combining both improved light-harvesting ability and favorable band bending to maximize the overall solar conversion efficiency.

Another important factor for designing efficient PEC-HER photocathodes is the optimization of the HER electrocatalysts. Despite the wide variety of earth-abundant HER catalysts that have recently been investigated to replace noble metals,[6, 20-31] only a few of them have been integrated into PEC systems.[13, 17, 18, 32-39] Many problems need to be addressed in integrated PEC systems, such as the semiconductor/catalyst chemical incompatibility and stability issues, synthesis and controllability difficulties, induced interfacial defect states and recombination sites, and inefficient charge transfer across interfaces. Currently, catalysts are primarily evaluated based on their electrocatalytic activity. However, optical transparency of catalysts also plays a crucial role in the overall PEC performance. Despite good electrocatalytic activity, most reported HER catalysts suffer from strong light absorption or high reflection, which consequently reduces the light reaching the absorbers and decreases the generated photocurrent.[5, 12, 13] Hence, in those cases, balancing high catalyst loading and good optical transparency becomes one of the most challenging tasks. In this regard, catalysts with good optical transparency would present particular advantages. Nevertheless, the optical properties of HER electrocatalysts have rarely been systematically investigated to demonstrate the significance of good transparency in enabling high current density and high efficiency.

3.3 Materials and Methods

All chemicals were purchased from Sigma-Aldrich and used as received unless otherwise noted.

3.3.1 Fabrication of n^+pp^+ Si micropyramids (MPs).

Micropyramid arrays were fabricated on both sides of 150 µm-thick p-type (100) Si wafers (dopant concentration of 5×10^{15} cm^{-3}) by chemical etching in a solution of potassium hydroxide (KOH, 45 vol%) and isopropyl alcohol (IPA). 300 nm of n^+ emitter layer (dopant concentration of 9×10^{19} cm^{-3}) was formed by thermal diffusion of $POCl_4$ at 1000 °C. 300 nm of p^+ back surface field layer (dopant concentration of 3×10^{20} cm^{-3}) was fabricated by screen printing Al and annealing at 500 °C.

3.3.2 Direct CVD growth of MoQ_xCl_y onto graphite, fused silica, and Si substrates.

Graphite disk substrates (6.0 mm diameter; < 1 mm thick) were prepared by cutting and mechanically thinning slices of graphite rods (Ultra Carbon Corp., Ultra “F” Purity), followed by sequential sonication in acetone, isopropanol, ethanol and deionized water, and drying in an oven at 120 °C. Planar p-type Si wafers (B doped, resistivity of 1-2.5 Ω-cm, (100) orientation, prime grade, 525 µm thickness, 100 mm diameter, native silicon oxide) were obtained from Silicon Inc. Graphite disk substrates were used for electrocatalytic activity measurement, and planar or micropyramid Si wafers were cut into small pieces for photocathode fabrication. Prior to growth on Si substrates, the native oxide layer on Si was removed via etching in aqueous buffered HF solution (Buffer HF Improved, Transene Inc.) for 15 s. The home-built CVD consists of a quartz tube (1 inch O.D.) connected with an Ar gas inlet and a vacuum pump, and equipped with pressure and gas flow controllers placed in a tube furnace (Lindberg/Blue M). The graphite disks and Si substrates were placed at the center of the tube furnace. Two alumina combustion boats containing 30-40 mg molybdenum (V) chloride ($MoCl_5$, 95%) and 500-700 mg elemental sulfur or selenium powders (99.5 %), respectively, were initially placed outside of the tube furnace. Note $MoCl_5$ must be stored and weighed in a glovebox filled with inert gas, and when taken out of the glovebox must be sealed properly and quickly transferred into the CVD tube to avoid hydrolysis in air. The tube was evacuated to a base pressure of 10 mTorr and flushed three times with Ar carrier gas (99.999%) before the pressure was set to 780 Torr with Ar gas flowing at a rate of 125 sccm. For the synthesis of MoS_xCl_y, the furnace was heated to 225-375 °C with no H_2 gas flow, whereas for $MoSe_xCl_y$, the furnace was heated to 275-425 °C with 0-3 sccm H_2 flow. For making the best electrocatalysts and the best photocathodes, the optimal growth temperature for depositing MoS_xCl_y was 275 °C, and the optimal condition for depositing $MoSe_xCl_y$ was 400 °C with a 0.75 sccm H_2 gas flow. Once the temperature was stabilized, the two precursor boats were pushed into the mouth of the furnace (1.5 cm for $MoCl_5$ boat and 4.5 cm for S or Se boat) to initiate the reaction. The reaction was kept at the designated temperature for 10 min before the tube furnace was opened to allow natural cooling to room temperature under Ar flow.

3.3.3 Structural characterization.

Scanning electron microscopy (SEM) was performed using a LEO Supra55 VP microscope operating at 3 kV. Raman spectra were taken using a Thermo Scientific DXR confocal Raman microscope using a 532 nm excitation laser. X-ray photoelectron spectroscopy (XPS) was taken on a custom-built XPS system (Phi Electronics, Eden Prairie, MN), that included a model 10-610 Al K_α x-ray source (1486.6 eV photon energy) and a model 10-420 toroidal monochromator. A model 10-360 hemispherical analyzer with a 16-channel detector array was used, which under effective operating conditions had an analyzer resolution of 0.4 eV. Electrons were collected at an emission angle of 45° from the surface normal of the sample. High resolution data was collected for Mo3*d*, S2*p*, Se3*d*, O1*s* and C1*s*. All XPS are shifted so that the adventitious carbon C1*s* peak is at 284.8 eV to make sure the data across samples are aligned and that the samples are not experiencing differential charging effects that may convolute the data. The same setup with a UV light source of a He I discharge lamp (21.2 eV photon energy) was utilized for ultraviolet photoelectron spectroscopy (UPS). Electrons were collected at a 0° take-off angle from the surface normal with analyzer resolution of 0.09 eV. The location of the Fermi level was determined using platinum by setting the valence band maximum of platinum to zero. All data reported contain a Fermi level that has been set to 0 eV.

3.3.4 Electrochemical Characterization of Catalytic Activity Toward Hydrogen Evolution Reaction (HER).

All electrochemical measurements were performed in a three-electrode configuration using a rotating disk electrode (RDE) setup (Bioanalytical Systems, Inc.; RDE-2) with a Bio-Logic SP-200 potentiostat. 0.5 M H_2SO_4 (aq) was used as the electrolyte and continuously purged with H_2(g) (99.999%). A saturated calomel reference electrode (SCE) (CH Instruments) was used as the reference electrode and a graphite rod (National Carbon Co., AGKSP Spectroscopic Electrode) was used as the counter electrode. The graphite disks covered with catalysts were affixed to a glassy carbon RDE tip using silver paint (Ted Pella, PELCO Colloidal Silver). The SCE was calibrated against the reversible hydrogen potential (RHE) using a platinum wire (Kurt J. Lesker, 99.99%; 0.50 mm diameter) as both the working and counter electrodes to allow potentials to be referenced against RHE. Linear sweep or cyclic voltammograms were measured from +0.25 V to −0.45 V vs. RHE at a scan rate of 3 mV s^{-1} in both the forward and reverse directions at a rotating speed of 2000 RPM. After voltammetric characterization, electrochemical impedance spectroscopy (EIS) was performed at −0.24 V vs. RHE, applying a sinusoidal voltage with an amplitude of 10 mV and scanning frequency from 200 kHz to 50 mHz. The EIS spectra were modeled using a simplified Randles equivalent circuit (Figure A2.2), which consists of a resistor

(R_s) in series with a parallel arrangement of a resistor (R_{ct}) and a constant phase element (CPE).

3.3.5 Photoelectrochemical characterization.

The photoelectrochemical characteristics of MoQ_xCl_y/Si photocathodes were measured in a three-electrode configuration using a Bio-Logic SP-200 potentiostat under simulated 1 Sun irradiation (100 mW/cm^2) provided by a 1 kW Xe short arc lamp solar simulator (Newport Corp., Model 91191; AM1.5G filter). A Si photodiode (Thorlabs) was utilized to calibrate the light intensity by generating a photocurrent equal to that at 100 mW/cm^2 light intensity. 0.5 M H_2SO_4 was used as the electrolyte, a graphite rod was used as the counter electrode, and a SCE was used as the reference electrode. The electrolyte was vigorously stirred to minimize mass transport limitations and remove accumulated hydrogen gas bubbles on the electrode surface, and constantly purged with research-grade H_2 gas (99.999%) to maintain a constant Nernst potential for H^+/H_2 redox couple. The current density versus potential (J–E) data were measured with a scan rate of 10 mV/s, and were not corrected for any uncompensated resistance losses or any other extrinsic losses. EIS was performed at a constant potential of +0.40 V *vs* RHE while sweeping the frequency from 350 kHz to 1 Hz with a 10 mV AC dither and modeled using the equivalent circuit shown in Figure A2.2.

3.4 Results and Discussion

In this work, we fabricate highly efficient PEC-HER photocathodes by integrating amorphous MoQ_xCl_y (Q = S, Se) catalysts with n^+pp^+ Si MP absorber. We have previously reported MoS_xCl_y, synthesized via a low temperature chemical vapor deposition (CVD) reaction, as a standalone HER electrocatalyst,[38] exhibiting catalytic performance similar to 1T-MoS_2.[22] Here, we successfully extend this CVD synthesis method to amorphous $MoSe_xCl_y$ and demonstrate its significant HER catalytic activity. Moreover, we systematically evaluate the catalytic activity and the optical properties of MoS_xCl_y and $MoSe_xCl_y$, integrate them with planar p-Si and n^+pp^+ Si MP absorbers to fabricate photocathodes, and elucidate how the PEC performance is impacted by the choice of catalysts and light absorbers. We find that MoS_xCl_y is not only a highly active electrocatalyst for HER, but also a wide bandgap semiconductor with very low light absorption in the visible and near IR range. By integrating the MoS_xCl_y catalyst with n^+pp^+ Si MPs, we achieve the highest photocurrent density and highest solar-to-hydrogen conversion efficiency (6.2 %) ever reported for Si-based PEC-HER photocathodes using non-noble metal catalysts due to a concurrent improvement in electrocatalytic activity, optical transparency, and light-harvesting capability.

We first used a low temperature CVD method to synthesize amorphous ternary compounds MoS_xCl_y and $MoSe_xCl_y$ on graphite, fused silica and Si substrates to evaluate their catalytic and optical properties (see experimental section for details). Molybdenum chloride ($MoCl_5$) was used as the precursor to incorporate Cl into the synthesized amorphous catalyst films. The employed low reaction temperatures led to the formation of amorphous materials with high degree of structural disorder and more active sites. At low temperatures, we expect the reaction rate to be limited by kinetics, which allow Cl anions to remain in the final product due to the homogenous but partial conversion of $MoCl_5$ precursor. The structural characterization of amorphous MoS_xCl_y has been described previously,[38] here we focus the discussion on $MoSe_xCl_y$. Raman spectroscopy and X-ray diffraction (XRD) measurements confirmed that the as-synthesized $MoSe_xCl_y$ films are amorphous (Figure 3.1a inset and Figure A2.1). Energy-dispersive X-ray spectroscopy (EDS) confirmed the presence of Cl in the $MoSe_xCl_y$ film (Figure 3.1a) and showed the stoichiometry of

Mo:Se:Cl to be around 1:2.0:1.2. Scanning electron microscopy (SEM) images of amorphous MoQ_xCl_y in comparison with crystalline MoQ_2 samples grown on graphite substrates are shown in Figure 3.2. X-ray photoelectron spectroscopy (XPS) and ultraviolet photoelectron spectroscopy (UPS) were utilized to understand the chemical and structural differences between amorphous MoQ_xCl_y and crystalline MoQ_2. No Cl was present in crystalline MoQ_2, while a significant amount of Cl was observed in amorphous MoQ_xCl_y (Figure 3.3). The work functions of MoS_xCl_y and $MoSe_xCl_y$ were determined to be 5.2 eV and 4.8 eV, respectively (Figure 3.3a), which are significantly higher than those of the crystalline MoS_2 (4.4 eV)[38] and $MoSe_2$ (4.4 eV)[40], further highlighting the difference in properties between MoQ_xCl_y and MoQ_2.

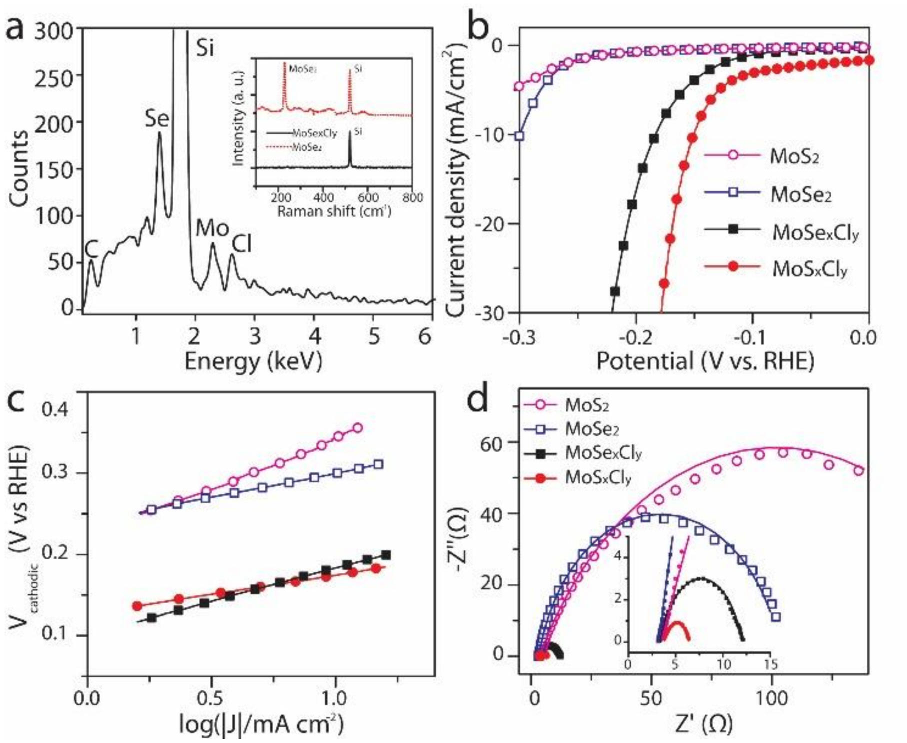

Figure 3.1. (a) EDS and Raman (inset) of amorphous MoSe$_x$Cl$_y$ deposited on Si substrate. Electrochemical characterization of amorphous MoS$_x$Cl$_y$ (red solid dots), MoSe$_x$Cl$_y$ (black solid squares) in comparison with crystalline MoS$_2$ (magenta open dots) and MoSe$_2$ (blue open squares): (b) Polarization curves, (c) Tafel analysis, (d) Nyquist impedance plots. The high frequency region of Nyquist impedance plots in 1d is magnified in 3.1d inset.

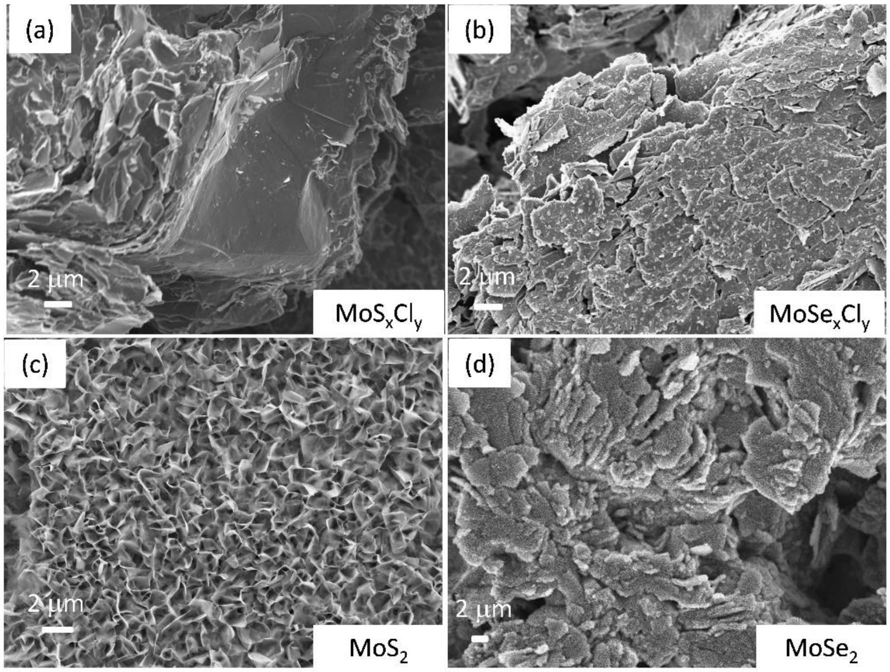

Figure 3.2. Top-down SEM images of amorphous MoS$_x$Cl$_y$ (a) and MoSe$_x$Cl$_y$ (b), in comparison with crystalline MoS$_2$ (c) and MoSe$_2$ (d) grown on graphite substrates.

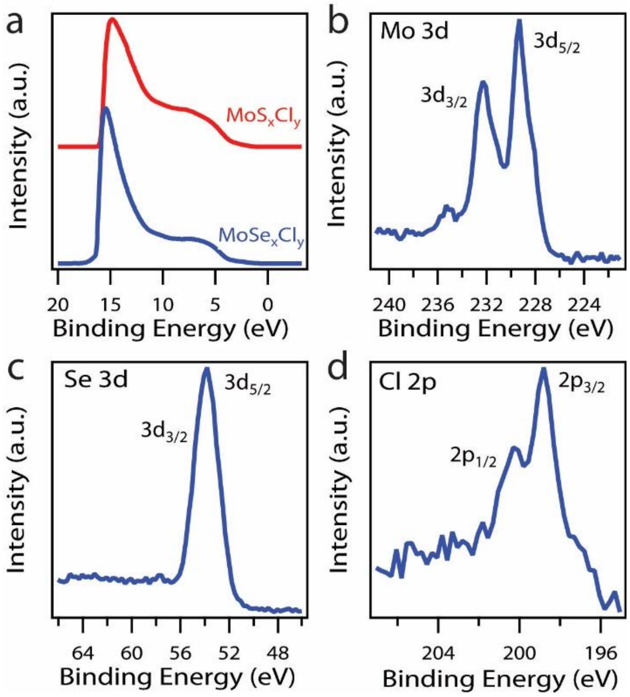

Figure 3.3. (a) Comparison of ultraviolet photoelectron spectra (UPS) of MoS_xCl_y and $MoSe_xCl_y$. (b-d) High resolution XPS of $MoSe_xCl_y$ for Mo3d (b), Se3d (c) and Cl2p (d).

The electrocatalytic activities of these amorphous MoQ_xCl_y compounds on graphite disks toward HER were then compared *via* standard rotating disk electrode (RDE) measurements in a three-electrode configuration in 0.5 M H_2SO_4 electrolyte (see experimental section for details). Different CVD growth conditions were systematically investigated to optimize the new $MoSe_xCl_y$ electrocatalyst (Figure 3.4). In general, lower reaction temperatures led to higher degree of structural disorders and higher concentration of active sites.[38] However, when the temperature was below 300 °C, the evaporation of precursors and deposition became limited, resulting in poor HER performance. The H_2 flow rate affected the catalytic performance of $MoSe_xCl_y$ (Figure 3.4); therefore a small amount of H_2 flow was chosen for optimal $MoSe_xCl_y$ growth, but it did not affect the synthesis or performance of MoS_xCl_y. Figure 3.1b summarizes the polarization curves for the best performing MoS_xCl_y (grown at 275 °C) and $MoSe_xCl_y$ (grown at 400 °C) in comparison with crystalline MoS_2 and $MoSe_2$. As summarized in Table 3.1, amorphous MoS_xCl_y and $MoSe_xCl_y$ exhibit catalytic onsets and significant H_2 evolution ($J_{cathodic} = -10$ mA cm^{-2}) at much lower overpotentials than crystalline MoQ_2, demonstrating a dramatic improvement in catalytic activity. We also observed significant differences in the Tafel slopes for MoQ_xCl_y and MQ_2, which reflects the differences in hydrogen adsorption energy and HER reaction mechanisms, which can be ultimately attributed to their electronic and structural differences. As shown in Figure 3.1c, MoS_xCl_y showed a Tafel slope of 48 mV decade^{-1}, suggesting a Volmer–Heyrovsky HER mechanism, in contrast to crystalline MoS_2, which showed Volmer–Tafel HER mechanism with a Tafel slope of 122 mV decade^{-1}. From $MoSe_2$ to $MoSe_xCl_y$, the Tafel slope changed from 60 to 82 mV decade^{-1}, suggesting a transition of the rate-determining step from electrochemical desorption to discharge. We also carried out electrochemical impedance spectroscopy (EIS) and fitted them using a simplified Randles equivalent circuit (Figure A2.2) to investigate the electrode kinetics

(Figure 3.1d). Amorphous MoS_xCl_y showed a smaller charge transfer resistance (R_{ct} = 2.7 Ω) than $MoSe_xCl_y$ (8.6 Ω), and both amorphous MoQ_xCl_y compounds exhibited an R_{ct} that was orders of magnitude smaller than crystalline MoS_2 (181 Ω) and $MoSe_2$ (101 Ω).

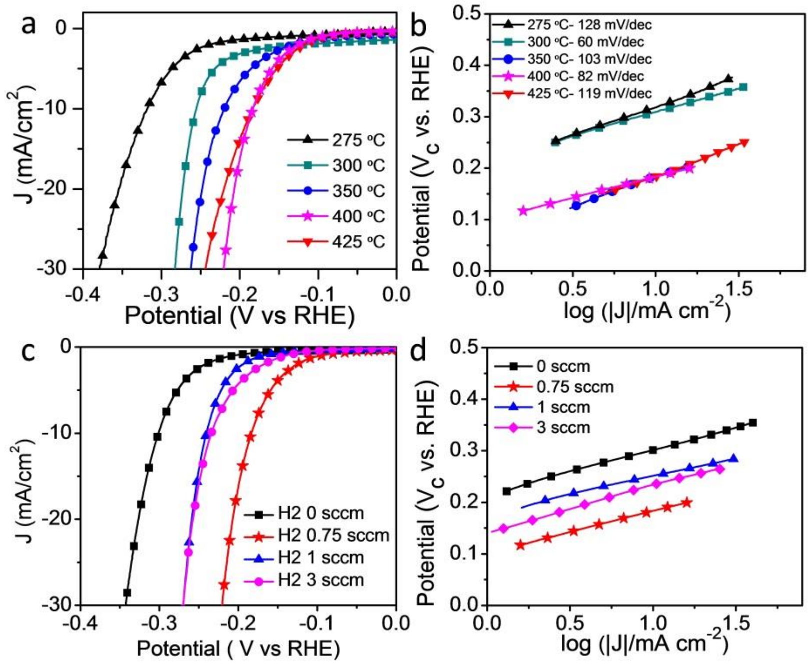

Figure 3.4. Electrochemical characterization of $MoSe_xCl_y$ electrocatalysts synthesized under different conditions on graphite substrates. Polarization curves (a) and Tafel analysis (b) of $MoSe_xCl_y$ synthesized at different CVD temperatures with 0.75 sccm H_2 flow rate. Polarization curves (c) and Tafel analysis (d) of $MoSe_xCl_y$ synthesized at different H_2 flow rates at 400 °C.

Table 3.1. Summary of the electrocatalytic properties of MoS_xCl_y and $MoSe_xCl_y$ electrodes in comparison with crystalline MoS_2 and $MoSe_2$.

Samples	Onset potential [mV *vs* RHE]	η for *J* = −10 mA cm^{-2} [mV *vs* RHE]	Tafel slope [mV/decade]	R_{ct} [Ω]	J_0 [mA cm^{-2}]
MoS_xCl_y	-60	-150	48	2.7	2.14
$MoSe_xCl_y$	-85	-183	82	8.6	58.7
MoS_2	-251	-344	122	180.8	14.5
$MoSe_2$	-246	-300	60	100.8	0.095

In addition to high electrocatalytic activity, high transparency with low optical losses is also highly desirable for an ideal catalyst in an integrated PEC system. To examine the optical properties with minimum interference from substrates, we purposely grew MoQ_xCl_y films on transparent fused silica substrates. The UV-Vis absorbance spectra of MoS_xCl_y and $MoSe_xCl_y$ (Figure 3.5a) clearly show that MoS_xCl_y has little absorption in the 500-1200 nm wavelength region, where Si most strongly absorbs solar light; whereas $MoSe_xCl_y$ shows much stronger absorption in this range. In fact, the difference between the two samples can be directly compared in their photographs (Figure 3.5a inset): MoS_xCl_y is highly transparent and hardly different from bare fused silica, whereas $MoSe_xCl_y$ exhibits a much darker color and less transparency. To better understand the origin of such difference, we used Tauc plots (Figure 3.5b) to estimate the optical bandgaps of MoS_xCl_y and $MoSe_xCl_y$ to be 2.8 eV and 2.2 eV, respectively. Both values are much larger than those of crystalline MoS_2 (1.3 eV) and $MoSe_2$ (1.1 eV).[41] The large optical gap of MoS_xCl_y is in agreement with its onset in the absorbance spectrum and well explains its low absorption in the visible and near-IR range. This suggests that MoQ_xCl_y, especially MoS_xCl_y, unlike most other electrocatalysts, will transmit the majority of the visible light important for solar energy harvesting. This rather unusual characteristic, combined with its high electrocatalytic activity, make MoS_xCl_y a unique and highly competitive catalyst material for PEC-HER.

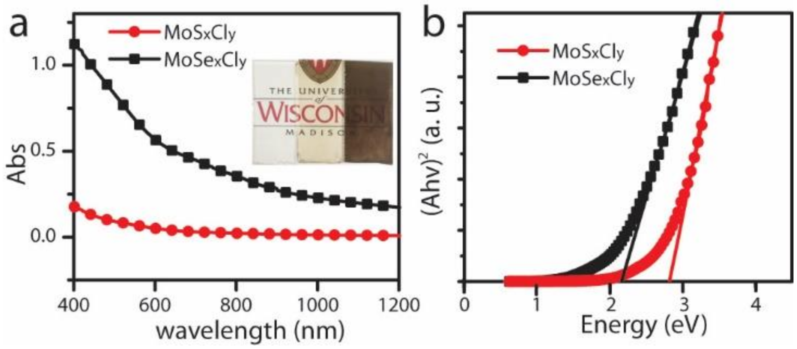

Figure 3.5. Optical characteristics of MoQ_xCl_y catalysts. (a) Absorbance spectra of MoS_xCl_y (red dots) and $MoSe_xCl_y$ (black squares) grown on fused silica. Inset shows the digital images of bare fused silica (left), MoS_xCl_y on fused silica (middle) and $MoSe_xCl_y$ on fused silica (right). (b) Tauc plots that allow the extraction of the optical gaps of MoS_xCl_y (red dots) and $MoSe_xCl_y$ (black squares) to be 2.8 eV and 2.2 eV, respectively.

Effective catalyst-semiconductor coupling is another key consideration for superior PEC performance. As demonstrated in our previous work,[39] direct CVD growth of a catalyst on Si provides higher quality interfaces with smaller charge transfer resistances, leading to much better PEC performance than samples made by dropcasting. Therefore, here we utilized low temperature CVD growth to directly integrate MoQ_xCl_y with Si to achieve high performance PEC devices. Simple p-type planar Si was first employed as the light absorber for a control experiment. A three-electrode configuration was used to measure the photocurrent density–potential (J−E) data in 0.5 M H_2SO_4 under simulated 1 Sun irradiation (see experimental section for details). As shown in the J−E curves in Figure 3.6, the onset potential (defined as the potential required to reach a photocurrent density of 0.5 mA/cm^2) shifted from −0.14 V vs. RHE for bare planar p-Si to +0.27 V vs. RHE for MoS_xCl_y/Si planar, and the photocurrent density at 0 V vs. RHE increased from 0 to 20.6 mA/cm^2, which is comparable to a Pt/p-Si photocathode measured in the same condition.[36] The PEC performance of $MoSe_xCl_y$ on planar p-Si was also significantly improved compared to that of bare p-Si, but the improvement was not as much as with MoS_xCl_y. This difference could be attributed to multiple factors, including inferior HER catalytic activity, unfavorable band bending, not optimal growth conditions for $MoSe_xCl_y$, and potential presence of native silicon oxide at the interface.

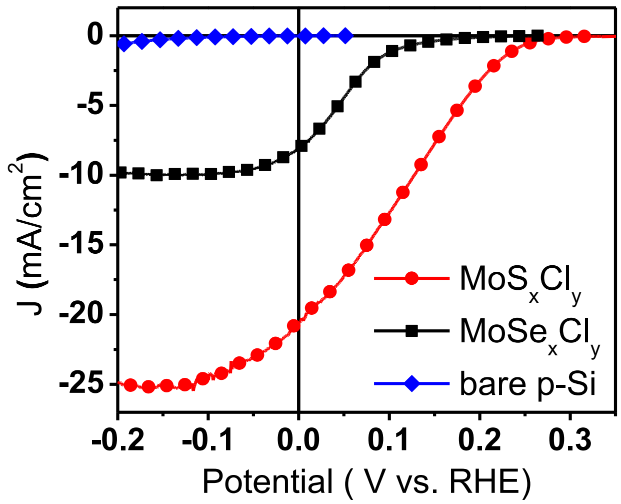

Figure 3.6. J-E curves of MoS_xCl_y/planar p-Si (red dots), $MoSe_xCl_y$/planar p-Si (black squares) and bare planar p-Si (blue diamonds) photocathodes measured under 1 Sun illumination in 0.5 M H_2SO_4.

The promising results achieved using simple planar p-Si photocathodes demonstrate the great potential of MoQ_xCl_y catalysts in PEC-HER. To further boost the performance and design more efficient PEC-HER systems, we utilized Si MPs with an n^+pp^+ junction as a more effective light absorber. The multiple scattering effect of MP structures allows more photons to enter the device hence significantly improves the omnidirectional light-harvesting ability[19] (Figure 3.7a). Moreover, the Si MPs could generate a much larger photovoltage owing to its built-in p-n junction. With the additional p^+ layer on the back of n^+p Si, the majority carrier collection could be further facilitated, reducing overall series resistance and improving the fill factor and device performance.[11] Figure 3.7b inset and Figure 3.7d show the top-down and cross-sectional SEM images of the bare n^+pp^+ Si MP substrate. Prior to MoQ_xCl_y growth, a complete solid-state photovoltaic cell was fabricated to verify the solar performance of bare Si MPs. As shown in Figure 3.7b, a solar to electricity conversion efficiency of 17.6% was achieved with an open circuit voltage (V_{oc}) of 0.56 V, a short circuit current (J_{sc}) of 42.0 mA/cm^2 and a fill factor (FF) of 0.75. Notably, the J_{sc} achieved here is much higher than what has been previously reported for planar Si solar cells, due to the improved light-harvesting ability of Si MPs. High V_{oc} and FF were also achieved, reflecting the large band bending and low charge recombination in the n^+pp^+ junction. After CVD growth, a conformal thin film of MoQ_xCl_y catalyst completely covers the Si MPs surface as illustrated in Figure 3.7a. MoS_xCl_y forms a smooth film with a thickness between 40-60 nm (Figure 3.7e and Figure A2.3) and $MoSe_xCl_y$ also yields a film around 40-60 nm but composed of dense nanoflakes and nanoparticles (Figure 3.7f and Figure A2.3). UV-Vis spectra were measured to compare the reflectance between planar Si, Si MPs, and MoQ_xCl_y covered Si MPs. Much lower reflectance and higher absorption were recorded for Si MPs relative to planar p-Si (Figure 3.7c), which demonstrates the improved light-harvesting properties of Si MPs.

Moreover, comparing MoS_xCl_y/Si MPs with bare Si MPs, we do not see significant change in their reflectance spectra, especially in the 500-1200 nm region where Si strongly absorbs solar light. This is attributed to the large bandgap and semi-transparent nature of MoS_xCl_y catalyst film, and is consistent with the absorbance spectrum collected on MoS_xCl_y on fused silica (Figure 3.5a). In comparison, because of the larger absorbance of $MoSe_xCl_y$, a much darker color is seen in the photograph of $MoSe_xCl_y$ coated Si MPs (Figure 3.7c inset), which is also confirmed in the suppressed reflectance of $MoSe_xCl_y$/Si (Figure 3.7c).

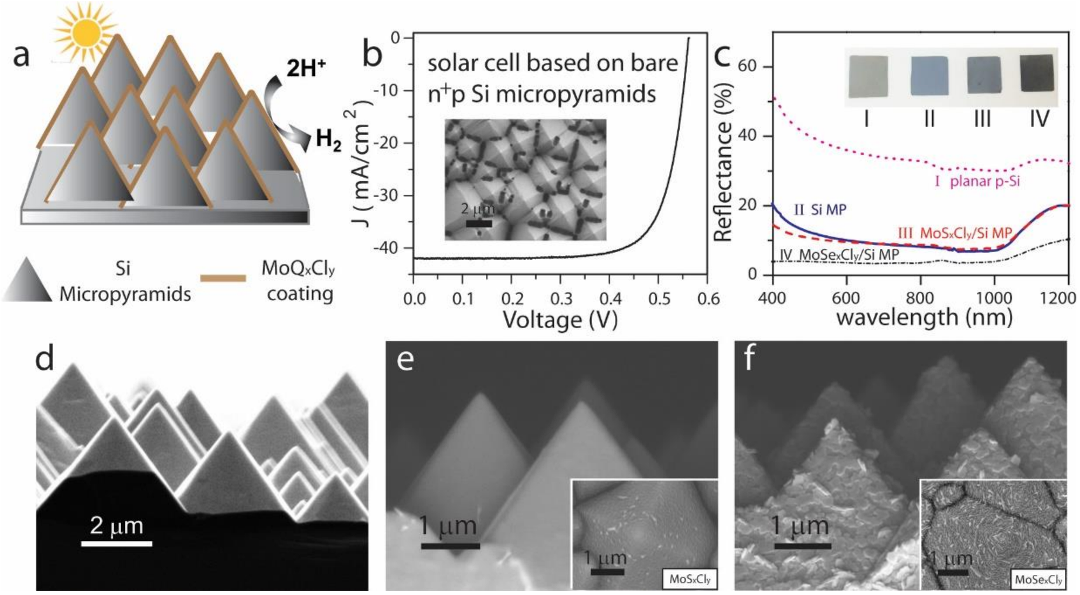

Figure 3.7. (a) Schematic of MoQ_xCl_y catalysts coated on n^+pp^+ Si MPs for PEC hydrogen generation. (b) J-V characteristics of a solar photovoltaic cell based on bare n^+pp^+ Si MPs. Inset shows a top-down SEM image of a bare Si MP substrate. (c) Reflectance spectra of bare planar Si (I), Si MPs (II), MoS_xCl_y on Si MPs (III), and $MoSe_xCl_y$ on Si MPs (IV). Inset shows the corresponding photographs. Cross-sectional SEM images of (d) bare Si MPs substrate, (e) MoS_xCl_y/Si MPs and (f) $MoSe_xCl_y$/Si MPs. Insets in (e, f) show the corresponding top-down SEM images of MoQ_xCl_y/Si.

To examine the advantage of n^+pp^+ Si MPs over planar p-Si and the influence of other parameters in PEC-HER systems, we fabricated different MoQ_xCl_y coated photocathodes and compared their PEC performance under simulated 1 Sun irradiation. The use of n^+pp^+ Si MPs results in a dramatic improvement in both the onset potential and photocurrent of the photocathodes. Specifically, as shown in Figure 3.8a and summarized in Table 3.2, the onset potential increased from 0.27 V vs. RHE for MoS_xCl_y on planar p-Si to 0.41 V vs. RHE for MoS_xCl_y on n^+pp^+ Si MPs, owing to the favorable band bending in the n^+pp^+ design. Similarly, the onset of $MoSe_xCl_y$ coated photocathodes also improved significantly from 0.18 V vs. RHE to 0.35 V vs. RHE. Moreover, the photocurrent density at 0 V vs. RHE increased dramatically from 10-20 mA/cm^2 for planar Si photocathodes to 35-43 mA/cm^2 for Si MPs photocathodes, further demonstrating the effect of improved light harvesting by Si MPs. For comparison, Pt, the benchmark catalyst for HER, was also e-beam evaporated (5 nm) on Si MPs. Figure 3.8a highlights the difference among various catalysts and clearly shows the trend of decreasing onset potential with increasing HER overpotential. Pt/Si MP photocathode still exhibits the smallest catalytic overpotential and the highest onset potential at 0.53 V, closest to the V_{oc} of the Si MP solar cell. MoS_xCl_y shows better catalytic activity and smaller catalytic overpotential than $MoSe_xCl_y$, which results in the more positive onset potential for MoS_xCl_y on Si MPs in the PEC test. The difference in photocurrent density, on the other hand, is mostly caused by the difference in the optical transparency of the various catalysts. Even though Pt is the most active electrocatalyst, compared to MoS_xCl_y, Pt has less optical transparency, resulting in a smaller photocurrent density. Due to the large optical gap and minimum light absorption of MoS_xCl_y, the MoS_xCl_y/Si MP photocathode achieves a photocurrent density as high as 43 mA/cm^2 at 0 V vs. RHE, which is the highest current density ever reported for Si based photocathodes and even surpasses that achieved by Pt/n^+pp^+ Si MPs. In addition, this high current density is close to the J_{sc} achieved for Si MP solar cells, suggesting minimal optical loss due to the catalyst coating, and is because of the synergistic effects of the efficient light-trapping property of the Si micropyramid structure and the high-transparency of the catalyst. To confirm the high photocurrent is indeed due to hydrogen generation, we used gas chromatography-mass spectrometer (GCMS) to measure the amount of generated H_2 in comparison with the theoretical H_2 amount calculated from the measured photocurrent of the device integrated over time (Figure 3.9). The Faradaic efficiency, which is defined as the experimental detected H2 amount divided by the theoretical H_2 amount, is close to 100% for both MoS_xCl_y/Si MP and $MoSe_xCl_y$/Si MP photocathodes. As a result of the high current density and good photovoltage, excellent overall performance is achieved for all MoQ_xCl_y/n^+pp^+Si MP photocathode systems (Table 3.2), with MoS_xCl_y/n^+pp^+Si MPs representing one of the most efficient Si photocathode systems with non-noble metal catalysts.

Table 3.2 Summary of J at 0 V vs. RHE, onset potential, and fill factor for various photocathodes: MoS_xCl_y on planar p-Si, MoS_xCl_y, $MoSe_xCl_y$, and Pt on n^+pp^+ Si MPs.

Photocathodes	J at 0 V vs. RHE [mA cm^{-2}]	Onset Potential [V]	Fill Factor
MoS_xCl_y/Si planar	20.6	0.27	0.23
MoS_xCl_y/Si MPs	43.0	0.41	0.35
$MoSe_xCl_y$/Si MPs	38.8	0.35	0.34
Pt/Si MPs	36.7	0.53	0.47

Besides the high PEC performance, excellent stability is also demonstrated for these MoQ_xCl_y/Si MP photocathodes. Both MoS_xCl_y/Si MPs and $MoSe_xCl_y$/Si MP photocathodes were tested under illumination at 0 V vs. RHE for more than 2 hours with negligible decreases in current density and PEC performance (Figure 3.8b). Compared with the 20% decrease in 1T-MoS_2/p-Si over the course of 2 h,[39] the stability of these MoQ_xCl_y/Si MPs has been greatly enhanced. This is due to the effective protection by the compact MoQ_xCl_y films conformally coated on the Si surface (Figure A2.3). While other protective layers for Si have been reported, they could potentially block light absorption and lead to decreased photocurrent.[13, 32] Therefore, the utilization of semi-transparent catalysts like MoS_xCl_y to serve as both the catalytic and protective layer could enable high current density while maintaining good stability at the same time.

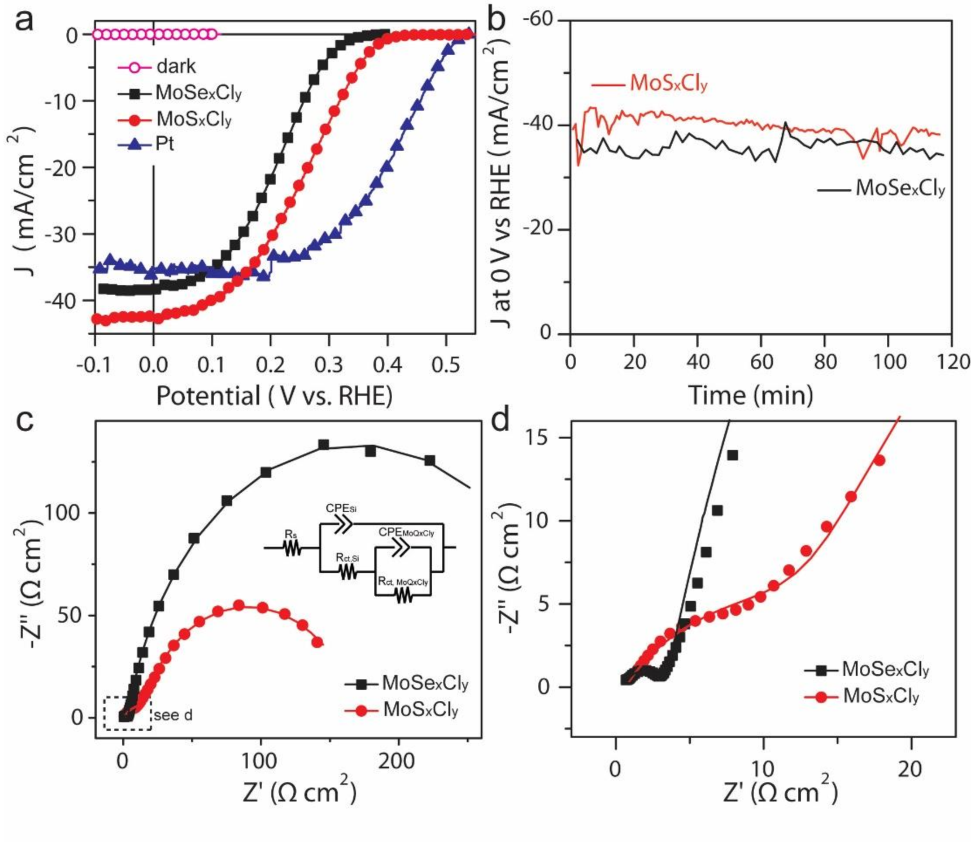

Figure 3.8. (a) J-E curves for MoS_xCl_y/Si MPs (red dots), $MoSe_xCl_y$/Si MPs (black squares) and Pt/Si MPs (blue triangles) photocathodes measured in 0.5 M H_2SO_4 under simulated 1 Sun irradiation. (b) Chronoamperometry measurement of MoQ_xCl_y/Si MPs photocathodes measured at 0 V vs RHE under illumination over 2 h. (c) Nyquist impedance plots of MoS_xCl_y/Si MP (red dots) and $MoSe_xCl_y$/Si MP (black squares) measured under illumination. The dashed box in panel c is magnified in d. The solid line traces correspond to the fitting using the equivalent circuit in the inset of panel c.

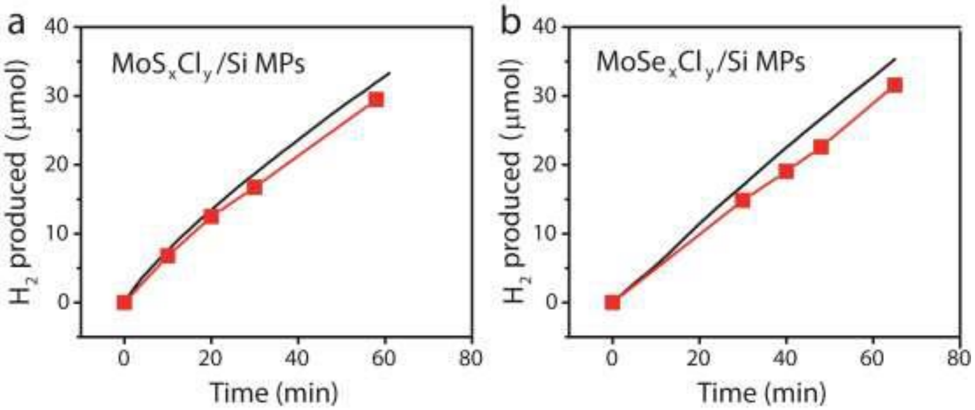

Figure 3.9. Theoretical (black curve) and experimental (red data points) amount of generated H_2 for MoS_xCl_y/Si MP photocathode (a) and $MoSe_xCl_y$/Si MP photocathode (b), showing Faradaic efficiencies close to 100%. Faradaic efficiency is defined as the experimental detected H_2 amount (measured using GC-MS) divided by the theoretical H_2 amount (calculated from the measured photocurrent of the device integrated over time). The total amount of H_2 detected by GC-MS after continuous illumination at 0 V vs. RHE for 1 h is close for the MoS_xCl_y and $MoSe_xCl_y$ photocathodes, despite the fact that higher photocurrent density and efficiency was shown for the MoS_xCl_y photocathode in Figure 3.8a. The reason for this is that the *specific* MoS_xCl_y photoelectrode we used was an old photoelectrode that has already gone through a 2 h stability test, so the generated photocurrent was decreasing over the 1 h measurement period. This could also be revealed from the decreasing slope of H_2 generation in Figure 3.9a, indicating the decreasing H_2 generation rate due to the gradual decreasing photocurrent. In contrast, the photocurrent of the $MoSe_xCl_y$ photoelectrode kept constant during the 1 h measurement period, which is confirmed by the constant slope of H_2 generation in Figure 3.9b. Therefore, although the MoS_xCl_y photoelectrode has better performance and higher current density than the $MoSe_xCl_y$ photoelectrode in general, due to the inferior stability of the specific MoS_xCl_y photoelectrode, the overall amount of hydrogen generated over the 1 h time period observed in Figure 3.9 is close for

the two photoelectrodes. If we compare the generated H_2 for the first 20 or 30 min instead of 1 h, the MoS_xCl_y photoelectrode produced more H_2 than the $MoSe_xCl_y$ photoelectrode, consistent with its higher performance.

To provide more insights into the PEC performance, we conducted electrochemical impedance spectroscopy (EIS) measurements under illumination to elucidate the charge transfer resistances (R_{ct}) in MoQ_xCl_y/Si MP photocathodes. Two semicircles were observed in the Nyquist impedance plots for both photocathodes (Figure 3.8c and 3.8d), which were fitted using an equivalent circuit (Figure 3.8c inset) following reported examples of catalyst-semiconductor systems.[39, 42] The charge transfer resistance across the absorber-catalyst interface ($R_{ct, Si}$) is a good indicator of the coupling between the light absorber and the catalyst. As reflected in the first semicircle, the $R_{ct, Si}$ is quite small for both MoS_xCl_y (18.6 Ω cm^2) and $MoSe_xCl_y$ (3.1 Ω cm^2), suggesting the benefits of the direct CVD growth in achieving high-quality interfaces between the absorber and catalyst. This fast charge transfer also lays the foundation for efficient utilization of electrons for hydrogen evolution, enabling better PEC performance. Moreover, the charge transfer resistance from the catalyst to the electrolyte ($R_{ct,MoQxCly}$), as depicted by the second semicircle, reflects the catalytic activity of the catalysts. MoS_xCl_y showed a smaller $R_{ct,MoQxCly}$ (155 Ω cm^2) compared to $MoSe_xCl_y$ (333 Ω cm^2), consistent with their electrocatalytic and photoelectrochemical performance shown in Figure 3.1 and 3.8a.

3.5 Conclusions

In summary, we have demonstrated that utilizing Si micropyramids with a designed n^+pp^+ junction significantly improves both the photocurrent and photovoltage of photocathodes. More importantly, when such a semiconductor is integrated with a direct CVD grown MoS_xCl_y thin film – a catalyst that possesses both excellent HER catalytic activity and high optical transparency – we achieve the highest photocurrent density for Si-based PEC systems with non-noble metal catalysts. Various design and optimization strategies regarding catalysts, absorbers and coupling between the two have been systematically investigated to provide helpful guidelines on how to rationally design efficient photocathodes with optimal PEC performance.

3.6 References

(1) N. S. Lewis, D. G. Nocera, *Proc. Natl. Acad. Sci. USA* **2006**, *103*, 15729.

(2) J. A. Turner, *Science* **2004**, *305*, 972.

(3) D. G. Nocera, *Accounts Chem. Res.* **2012**, *45*, 767.

(4) M. G. Walter, E. L. Warren, J. R. McKone, S. W. Boettcher, Q. X. Mi, E. A. Santori, N. S. Lewis, *Chem. Rev.* **2010**, *110*, 6446.

(5) J. R. McKone, N. S. Lewis, H. B. Gray, *Chem. Mater.* **2014**, *26*, 407.

(6) M. S. Faber, S. Jin, *Energy Environ. Sci.* **2014**, *7*, 3519.

(7) K. Sun, S. H. Shen, Y. Q. Liang, P. E. Burrows, S. S. Mao, D. L. Wang, *Chem. Rev.* **2014**, *114*, 8662.

(8) S. Y. Reece, J. A. Hamel, K. Sung, T. D. Jarvi, A. J. Esswein, J. J. H. Pijpers, D. G. Nocera, *Science* **2011**, *334*, 645.

(9) S. W. Boettcher, J. M. Spurgeon, M. C. Putnam, E. L. Warren, D. B. Turner-Evans, M. D. Kelzenberg, J. R. Maiolo, H. A. Atwater, N. S. Lewis, *Science* **2010**, *327*, 185.

(10) S. W. Boettcher, E. L. Warren, M. C. Putnam, E. A. Santori, D. Turner-Evans, M. D. Kelzenberg, M. G. Walter, J. R. McKone, B. S. Brunschwig, H. A. Atwater, N. S. Lewis, *J. Am. Chem. Soc.* **2011**, *133*, 1216.

(11) D. Bae, T. Pedersen, B. Seger, M. Malizia, A. Kuznetsov, O. Hansen, I. Chorkendorff, P. C. K. Vesborg, *Energy Environ. Sci.* **2015**, *8*, 650.

(12) H. P. Wang, K. Sun, S. Y. Noh, A. Kargar, M. L. Tsai, M. Y. Huang, D. L. Wang, J. H. He, *Nano Lett.* **2015**. ASAP. DOI: 10.1021/nl5041463

(13) J. D. Benck, S. C. Lee, K. D. Fong, J. Kibsgaard, R. Sinclair, T. F. Jaramillo, *Adv. Energy Mater.* **2014**, *4*, 1400739.

(14) M. D. Kelzenberg, S. W. Boettcher, J. A. Petykiewicz, D. B. Turner-Evans, M. C. Putnam, E. L. Warren, J. M. Spurgeon, R. M. Briggs, N. S. Lewis, H. A. Atwater, *Nat. Mater.* **2010**, *9*, 368.

(15) B. M. Kayes, H. A. Atwater, N. S. Lewis, *J. Appl. Phys.* **2005**, *97*, 114302.

(16) S. Jeong, S. Wang, Y. Cui, *J. Vac. Sci. Technol. A* **2012**, *30*, 060801.

(17) J. R. McKone, E. L. Warren, M. J. Bierman, S. W. Boettcher, B. S. Brunschwig, N. S. Lewis, H. B. Gray, *Energy Environ. Sci.* **2011**, *4*, 3573.

(18) E. L. Warren, J. R. McKone, H. A. Atwater, H. B. Gray, N. S. Lewis, *Energy Environ. Sci.* **2012**, *5*, 9653.

(19) H. P. Wang, T. Y. Lin, C. W. Hsu, M. L. Tsai, C. H. Huang, W. R. Wei, M. Y. Huang, Y. J. Chien, P. C. Yang, C. W. Liu, L. J. Chou, J. H. He, *ACS Nano* **2013**, *7*, 9325.

(20) J. D. Benck, T. R. Hellstern, J. Kibsgaard, P. Chakthranont, T. F. Jaramillo, *ACS Catal.* **2014**, *4*, 3957.

(21) C. G. Morales-Guio, X. L. Hu, *Accounts Chem. Res.* **2014**, *47*, 2671.

(22) M. A. Lukowski, A. S. Daniel, F. Meng, A. Forticaux, L. S. Li, S. Jin, *J. Am. Chem. Soc.* **2013**, *135*, 10274.

(23) M. A. Lukowski, A. S. Daniel, C. R. English, F. Meng, A. Forticaux, R. J. Hamers, S. Jin, *Energy Environ. Sci.* **2014**, 2608.

(24) M. S. Faber, R. Dziedzic, M. A. Lukowski, N. S. Kaiser, Q. Ding, S. Jin, *J. Am. Chem. Soc.* **2014**, *136*, 10053.

(25) M. S. Faber, M. A. Lukowski, Q. Ding, N. S. Kaiser, S. Jin, *J. Phys. Chem. C* **2014**, *118*, 21347.

(26) D. S. Kong, H. T. Wang, Z. Y. Lu, Y. Cui, *J. Am. Chem. Soc.* **2014**, *136*, 4897.

(27) Q. Liu, J. Q. Tian, W. Cui, P. Jiang, N. Y. Cheng, A. M. Asiri, X. P. Sun, *Angew. Chem., Int. Ed.* **2014**, *53*, 6710.

(28) D. Merki, S. Fierro, H. Vrubel, X. L. Hu, *Chem. Sci.* **2011**, *2*, 1262.

(29) D. Voiry, H. Yamaguchi, J. W. Li, R. Silva, D. C. B. Alves, T. Fujita, M. W. Chen, T. Asefa, V. B. Shenoy, G. Eda, M. Chhowalla, *Nat. Mater.* **2013**, *12*, 850.

(30) E. J. Popczun, C. G. Read, C. W. Roske, N. S. Lewis, R. E. Schaak, *Angew. Chem., Int. Ed.* **2014**, *53*, 5427.

(31) E. J. Popczun, J. R. McKone, C. G. Read, A. J. Biacchi, A. M. Wiltrout, N. S. Lewis, R. E. Schaak, *J. Am. Chem. Soc.* **2013**, *135*, 9267.

(32) B. Seger, A. B. Laursen, P. C. K. Vesborg, T. Pedersen, O. Hansen, S. Dahl, I. Chorkendorff, *Angew. Chem., Int. Ed.* **2012**, *51*, 9128.

(33) C. G. Morales-Guio, S. D. Tilley, H. Vrubel, M. Gratzel, X. L. Hu, *Nat. Comm.* **2014**, *5*, 3059.

(34) Y. D. Hou, B. L. Abrams, P. C. K. Vesborg, M. E. Bjorketun, K. Herbst, L. Bech, A. M. Setti, C. D. Damsgaard, T. Pedersen, O. Hansen, J. Rossmeisl, S. Dahl, J. K. Norskov, I. Chorkendorff, *Nat. Mater.* **2011**, *10*, 434.

(35) S. P. Berglund, H. He, W. D. Chemelewski, H. Celio, A. Dolocan, C. B. Mullins, *J. Am. Chem. Soc.* **2014**, *136*, 1535.

(36) U. Sim, T. Y. Yang, J. Moon, J. An, J. Hwang, J. H. Seo, J. Lee, K. Y. Kim, J. Lee, S. Han, B. H. Hong, K. T. Nam, *Energy Environ. Sci.* **2013**, *6*, 3658.

(37) Y. J. Sun, C. Liu, D. C. Grauer, J. K. Yano, J. R. Long, P. D. Yang, C. J. Chang, *J. Am. Chem. Soc.* **2013**, *135*, 17699.

(38) X. Zhang, F. Meng, S. Mao, Q. Ding, M. J. Shearer, M. S. Faber, J. Chen, R. J. Hamers, S. Jin, *Energy Environ. Sci.* **2015**, *8*, 862.

(39) Q. Ding, F. Meng, C. R. English, M. Caban-Acevedo, M. J. Shearer, D. Liang, A. S. Daniel, R. J. Hamers, S. Jin, *J. Am. Chem. Soc.* **2014**, *136*, 8504.

(40) T. Shimada, F. S. Ohuchi, B. A. Parkinson, *Jpn. J. Appl. Phys. 1* **1994**, *33*, 2696.

(41) S. K. Mahatha, K. D. Patel, K. S. R. Menon, *J. Phys.-Condens. Mat.* **2012**, *24*, 475504.

(42) B. Klahr, S. Gimenez, F. Fabregat-Santiago, J. Bisquert, T. W. Hamann, *J. Am. Chem. Soc.* **2012**, *134*, 16693.

Chapter 4

Basal Plane Ligand Functionalization on Semiconducting 2H-MoS_2 Monolayers[*]

4.1 Abstract

Molybdenum disulfide (MoS_2) is a two-dimensional material promising for its electronic, optical and catalytic applications. To fully harness its potential, functionalization is essential to control its properties. However, most MoS_2 functionalization has been limited to the edges of 2H-phase MoS_2 or 1T-phase MoS_2, and the potential covalent functionalization on the basal plane of 2H-MoS_2 is poorly understood. Here we report a facile approach to covalently functionalize chemical vapor deposition (CVD) grown 2H-MoS_2 monolayers (MLs), as well as mechanically exfoliated MoS_2, via thiol conjugation at sulfur vacancies on the basal plane. Thorough characterization was conducted to confirm the functionalization by thiol molecules on MoS_2 MLs and it was demonstrated that sulfur vacancies in MoS_2 MLs play a key role in the functionalization of basal planes. By controlling the amount of sulfur vacancies via sulfur annealing, the degree of MoS_2 functionalization was effectively adjusted. Because thiol conjugation partially repairs or

---

[*] This chapter was prepared for publication in collaboration with Kyle J. Czech, Jianyuan Zhai, Yuzhou Zhao, Robert J. Hamers, John C. Wright and Song Jin* before being adapted here.

passivates sulfur vacancies, enhanced photoluminescence response and decreased active sites for hydrogen evolution catalysis were observed for functionalized MoS_2. Moreover, such functionalization can be utilized for making MoS_2-based heterostructures, an example of which was demonstrated using a dithiol molecule to link MoS_2 and PbSe quantum dots. These results provide new insights on the surface chemistry of MoS_2 and open up opportunities for MoS_2 MLs with well-controlled properties and applications.

4.2 Introduction

Two-dimensional (2D) layered transition metal dichalcogenides (TMDCs) are a family of compounds that have attracted widespread attention due to their potential applications in electronics, optoelectronics, sensing, energy storage, and catalysis.[1-5] MoS_2 has been one of the most studied TMDCs and acts as an excellent model system to explore the chemistry of 2D TMDCs. It consists of individual sandwiched S−Mo−S layers held together by weak van der Waals interactions and exhibits three common polymorphs, 2H, 3R and 1T.[6] Unique optical and electronic properties emerge when bulk MoS_2 is thinned to a single layer, making MoS_2 monolayers (MLs) particularly attractive. Photoluminescence (PL) is observed in MoS_2 MLs due to quantum confinement and the associated change from indirect band gap (1.3 eV) to direct band gap (1.8 eV),[7] which generates possibilities for many optoelectronic applications such as light-emitting diodes and photodetectors.[8-11] Field effect transistors (FETs) based on MoS_2 monolayers were also demonstrated to have high mobilities and on−off current ratios.[12]

Despite these promising material properties, the lack of understanding and control over MoS_2 surface functionalization poses limitations on its properties and applications, because surface functionalization can offer convenient platform to tailor the electronic, optical and catalytic properties and fully harness the capabilities of MoS_2.[13-16] Functionalization of 2D MoS_2 materials would also facilitate their biological applications[17,18] and integration into nanocomposites.[13,14] MoS_2 is traditionally considered rather chemically inert, especially along the basal plane that form the van der Waals gaps in the 2D layered structure.[1-3,14] Intuitively, the broken bonds at the edges of the MoS_2 layers increase the reactivity. Indeed, the edge sites of 2H-MoS_2 have been shown to display different catalytic and physical properties than those of the basal plane.[19] Edge functionalization of 2H-MoS_2 (bulk or layers) has been studied since the 1980s in order to understand and control the high density of defects and high reactivity.[20-23] However, no reports have explicitly demonstrated covalent functionalization on the basal planes of 2H-MoS_2. Moreover, the few studies of 2H-MoS_2 functionalization were focused on liquid exfoliated few-layer MoS_2 nanosheets.[21-25] The complex morphology and the high defect density often seen in such colloidal nanostructures prevents definitive characterization and differentiation between the edges and the basal plane. Furthermore, the chemistry of liquid exfoliated colloidal MoS_2 nanosheets can be very different from the MoS_2 monolayers made via chemical vapor deposition (CVD) or mechanical exfoliation that are of interest for typical device applications. In contrast to 2H-MoS_2, 1T-MoS_2 possesses a very different electronic structure and surface chemistry.[4] It is a metastable phase of MoS_2 that can be obtained by converting from the thermodynamically stable 2H-MoS_2 via chemical exfoliation. Covalent functionalization on the basal planes of chemically exfoliated 1T-MoS_2 nanosheets have been demonstrated by reacting them with organohalide and other molecules,[26,27] which led to changes in the optoelectronic properties of the materials. Alternatively, chemically exfoliated 1T-MoS_2 nanosheets could also be functionalized via thiol conjugation at the edges as well as on the basal planes, as many defects are generated during the harsh chemical exfoliation treatment required for the 1T-MoS_2 preparation, which are believed to form covalent bonds with thiol-containing molecules.[16-18,28-31] In contrast to these studies, the basal plane surface chemistry of semiconducting 2H-MoS_2 monolayers has not yet been carefully explored and it is important to develop a fundamental understanding of the mechanisms and be able to control the surface functionalization.

Even though the basal plane of 2H-MoS_2 is generally believed to be too inert for functionalization, it is not perfectly coordinated. Both experimental and computational studies have shown that a wide range of defect types are present and high densities of sulfur vacancies are observed on the basal plane of 2H-MoS_2 monolayers.[16,32-37] These sulfur vacancies could be reactive centers that enable basal plane ligand conjugation on semiconducting 2H-MoS_2 monolayers, providing a useful means by which to tune the electronic, optical and catalytic properties of MoS_2. In this work, we investigate the surface chemistry of CVD grown 2H-MoS_2 monolayers, and demonstrate successful covalent functionalization of 4-fluorobenzyl mercaptan and other thiol-containing molecules on the basal plane of MoS_2 MLs via thiol conjugation (Figure 1). Using the F-containing ligand as a marker, we clearly characterized the modified products using Fourier transform infrared spectroscopy (FTIR) and X-ray photoelectron spectroscopy (XPS), and correlated the degree of functionalization to the amount of sulfur vacancies present on MoS_2 ML basal plane. An enhanced photoluminescence (PL) response and significant reduction in catalytic activity are observed for functionalized MoS_2 MLs, consistent with partial repair and/or passivation of sulfur vacancies by thiol ligand conjugation. The generality of this functionalization also permits expansion to other thiol-containing ligands with different functional groups. Additionally, heterostructures of MoS_2 and PbSe quantum dots are successfully prepared using 1,5-pentanedithiol as a linker molecule. These functionalization methods open new pathways for facile synthesis of MoS_2-based heterostructures.

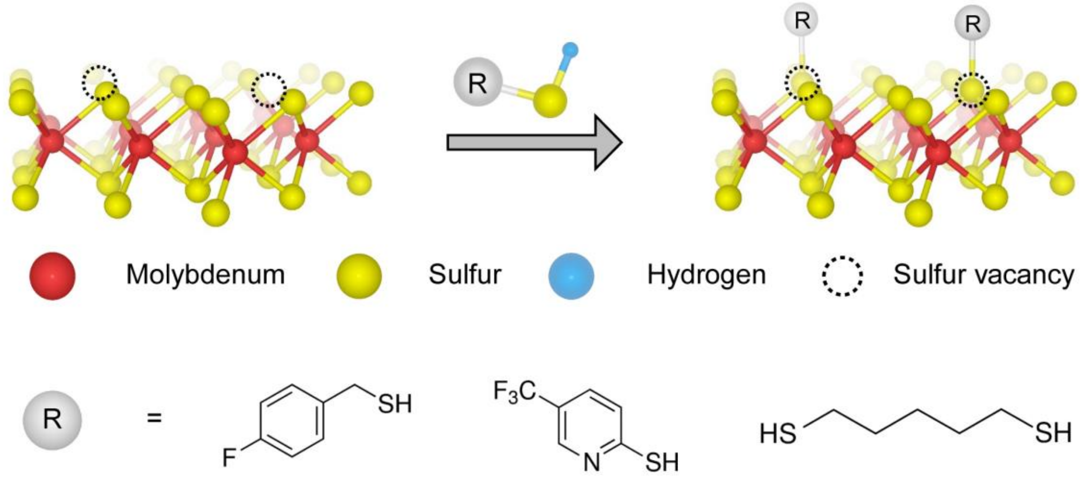

Figure 4.1. Schematic of ligand conjugation on sulfur vacancies on basal plane of 2H-MoS_2 monolayers.

4.3 Materials and Methods

All chemicals and reagents were purchased from Sigma-Aldrich and used as received unless noted otherwise.

4.3.1 Synthesis of MoS_2 monolayers via chemical vapor deposition (CVD)

MoS_2 monolayers were synthesized via a MoO_3 film sulfidation reaction similar to methods reported by Lou et al.[38] The synthesis was conducted in a home-built CVD system that consists of a quartz tube (1 inch O.D.) connected to a vacuum pump with pressure and gas flow controllers, and a tube furnace (Thermal Fisher, Lindberg Blue M). In a typical reaction, 1 nm of Mo metal (Kurt J. Lesker, 99.95%) was deposited via electron-beam evaporation onto a Si/SiO_2 or sapphire substrates at a rate of 0.05 Å/s. The Mo thin film was oxidized for 60 minutes at 400 ˚C under a pressure of 300 Torr with flow rates of 25 sccm Ar and O_2. Then the flow of O_2 was discontinued, the pressure was increased to 760 Torr and the temperature of the MoO_3 substrates increased to 750 ˚C. Upon reaching 750 ˚C, 200 mg of sulfur placed in an alumina boat was pushed to 18 cm upstream from the center of the furnace, and the reaction was allowed to proceed for 10 minutes, before the furnace was subsequently allowed to cool down naturally to room temperature. Then MoS_2 samples were collected and used without any further preparation.

4.3.2 Preparation of single- and multilayer MoS_2 via mechanical exfoliation

Single- and multilayer MoS_2 films were isolated from bulk MoS_2 (429MS-AB, small molybdenum disulfide crystal, SPI Supplies) using the scotch tape-based mechanical exfoliation method and then transferred onto the freshly cleaned Si substrates covered by a 100 nm thick SiO_2 layer.

4.3.3 Synthesis of MoS_2 nanoflowers on graphite substrates

The CVD synthesis of MoS_2 nanoflowers followed a reported procedure.[4] In a typical reaction, 50 mg of molybdenum (V) chloride ($MoCl_5$, 95%) and 200 mg elemental sulfur (99.5%) were put in alumina combustion boats and used as reaction precursors. The pressure was set to 770 Torr under a steady flow of Ar gas at 125 sccm, and the tube furnace was heated to 525 ˚C at 780 Torr for 20 min to grow MoS_2 nanoflowers directly on graphite substrates.

4.3.4 Functionalization of MoS_2 monolayers

The CVD MoS_2 ML sample on Si/SiO_2 substrate (or the mechanically exfoliated MoS_2 or CVD grown MoS_2 nanoflower samples) is soaked in neat 4-fluorobenzyl mercaptan liquid (or neat 1,5-pentanedithol liquid or 5-(trifluoromethyl) pyridine-2-thiol aqueous suspension) for 48 hours. Afterwards, the substrate is soaked in ethanol, acetone, isopropanol and water for 10 min each, and rinsed harshly with these solvents to wash off physisorbed molecules.

4.3.5 Preparation of MoS_2-PbSe quantum dot heterostructures

PbSe quantum dots were synthesized via a hot-injection approach modified from an established procedure.[50] Mechanically exfoliated single- and multilayer MoS_2 sample was first functionalized with 1,5-pentanedithiol. Then the functionalized MoS_2 sample was soaked in a suspension of PbSe quantum dots (QDs) in toluene. After 48 h, the MoS_2 sample was washed with toluene, ethanol, acetone and isopropanol to remove physisorbed PbSe QDs.

4.3.6 Structural characterizations

The optical images of all nanostructures were obtained on an Olympus BX51M optical microscope. Fourier transform infrared spectroscopy (FTIR) was conducted on Bruker Tensor 27 system which is equipped with a room temperature DTGS detector, mid-IR source (4000 to 400 cm^{-1}), and a KBr beamsplitter. High-resolution X-ray photoelectron spectroscopy (XPS) measurements were taken using a Thermo Al Kα XPS with a 180° double focusing hemispherical analyzer and 128-channel detector (60° angular acceptance). All X-ray photoelectron spectra are shifted so that the adventitious carbon C1*s* peak is at 284.8 eV to make sure the data across samples are aligned and that the samples are not experiencing differential charging effects that may complicate the data. Photoluminescence (PL) spectra were taken using a Thermo Scientific DXR confocal Raman microscope using a 532 nm excitation laser. The sample for TEM analysis was prepared by dry transfer of MoS_2-PbSe QD heterostructures onto a TEM grid (Ted Pella, lacey carbon type-A support film, 300 mesh, copper, no. 01890F). The TEM images were acquired on a FEI Titan scanning TEM at an accelerating voltage of 200 kV. Energy-dispersive X-ray spectroscopy (EDS) was performed using the same TEM equipped with an EDX detector.

4.3.7 Electron paramagnetic resonance spectroscopy measurement (EPR)

Electron paramagnetic resonance measurements were performed on a Bruker ELEXSYS E500 EPR Spectrometer at room temperature. The MoS_2 monolayers on a Si/SiO_2 substrate were loaded in a quartz tube and measured at a microwave power of 2 mW.

4.3.8 Electrochemical characterizations

All electrochemical measurements were performed in a three-electrode configuration using a rotating disk electrode (RDE) system (Bioanalytical Systems, Inc.; RDE-2) with a Bio-Logic SP-200 potentiostat. The electrolyte was 0.5 M H_2SO_4 (aq), which was continuously purged with H_2(g)

(99.999%). A saturated calomel reference electrode (SCE) (CH Instruments) was used as the reference electrode and a graphite rod (National Carbon Co., AGKSP Spectroscopic Electrode) was used as the counter electrode. Silver paint (Ted Pella, PELCO Colloidal Silver) was used to affix the graphite disks covered with MoS_2 catalysts to a RDE glassy carbon tip. The SCE was calibrated against the reversible hydrogen potential (RHE) using a platinum wire (Kurt J. Lesker, 99.99%; 0.50 mm diameter) as the working and counter electrodes to allow potentials to be referenced against a RHE. Cyclic voltammograms were measured from +0.15 V to −0.45 V vs. RHE at a scan rate of 3 mV s^{-1} at a rotating speed of 2000 RPM. The electrochemical impedance spectroscopy (EIS) was performed at −0.32 V vs RHE, applying a sinusoidal voltage with an amplitude of 10 mV and scanning frequency from 200 kHz to 50 mHz. The EIS spectra were modeled using a simplified Randles equivalent circuit to extract the series resistance (R), which was then subtracted from the polarization curves to correct for *iR* losses.

4.4 Results and Discussion

We synthesized MoS_2 monolayers on Si/SiO_2 or sapphire substrates using a CVD reaction by reacting molybdenum oxide films with sulfur precursor vapor at 750 ^{o}C (see Experimental Section for details).[38] As shown in Figure 2a, 7-15 µm, single-layer MoS_2 flakes were formed on the substrate after the reaction. We chose 4-fluorobenzyl mercaptan (Figure 1) as a representative organic molecule with a primary thiol functional group as well as a distinctive F element as a marker for MoS_2 ML functionalization detection. The MoS_2 MLs on Si/SiO_2 substrate was soaked in neat 4-fluorobenzyl mercaptan liquid for 48 hours and then soaked in ethanol, acetone, isopropanol and water for 10 min each, and rinsed harshly with these solvents to wash off any physisorbed ligands. To examine if there is any 4-fluorobenzyl mercaptan left on the MoS_2 MLs surface after the washing procedure, we first conducted FTIR on the treated MoS_2 ML sample (Figure 1b red curve) in comparison with the free 4-fluorobenzyl mercaptan ligand (Figure 1b black curve). Peaks corresponding to C-H, C=C and C-F stretches were clearly observed on the treated MoS_2 MLs sample. They match the peaks from 4-fluorobenzyl mercaptan, confirming the successful functionalization of the MoS_2 ML surface by 4-fluorobenzyl mercaptan. Notably, as highlighted in the box of Figure 2b, the S-H stretch peak at 2550 cm^{-1} that appears in the 4-fluorobenzyl mercaptan spectrum (black curve) was no longer observed in the functionalized MoS_2 ML sample. The disappearance of S-H peak has also been observed in other thiol conjugated systems, and is commonly attributed to thiol functional group successfully conjugating to MoS_2 surface with the S-H bond cleaved,[17,23,25] providing more evidence that 4-fluorobenzyl mercaptan is conjugating with the MoS_2 surface, not physisorbed on the surface. Slight changes in the FTIR spectra were observed on the functionalized MoS_2 ML sample compared to free 4-fluorobenzyl mercaptan ligand, which could be caused by the difference in measurement method (ATR vs. KBr pellet), the decreased signal-to-noise ratio, or potential changes in the ligand chemical environment. Such changes have also been observed in other thiol conjugated systems.[17,25]

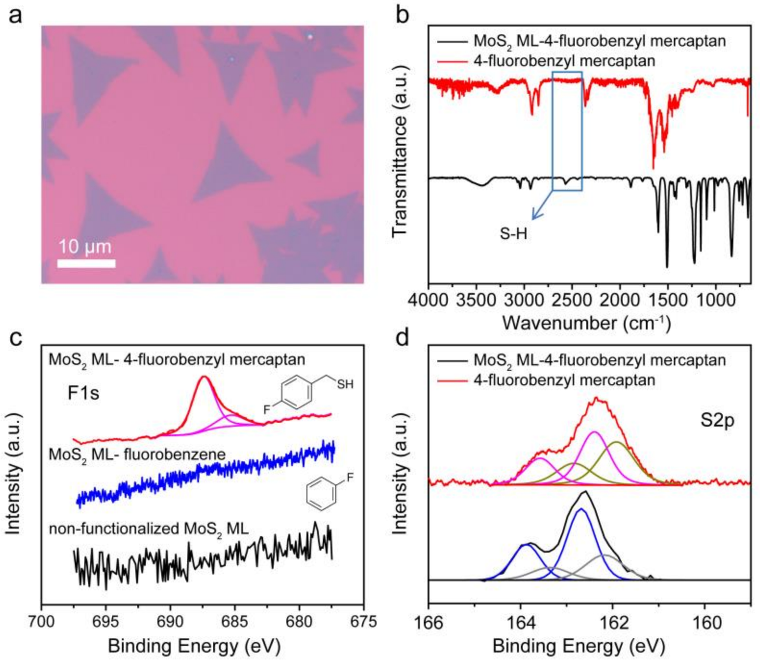

Figure 4.2. (a) A typical optical microscopy image of CVD grown MoS_2 monolayers on sapphire substrate. (b) FTIR spectra of 4-fluorobenzyl mercaptan functionalized MoS_2 MLs (red) in comparison to the free 4-fluorobenzyl mercaptan ligand (black). (c) High-resolution XPS of F1s region for 4-fluorobenzyl mercaptan functionalized MoS_2 ML (red), fluorobenzene treated MoS_2 ML (blue) and non-functionalized MoS_2 ML (black). (d) Fitted high-resolution XPS of S2p regions for 4-fluorobenzyl mercaptan functionalized MoS_2 MLs (red) and non-functionalized MoS_2 MLs (black).

To gain more insights into the functionalization, XPS was conducted to reveal potential changes in the chemical environment of MoS_2 MLs before and after functionalization. As shown in the high-resolution F1s spectra (Figure 2c), as-grown MoS_2 MLs do not show any F peak (black curve), indicating there is no F contamination on MoS_2 MLs substrate. After 4-fluorobenzyl mercaptan functionalization, a distinct F peak was clearly observed (red curve), confirming MoS_2 MLs surface has been successfully functionalized. A control experiment using fluorobenzene, a molecule with similar chemical structure with 4-fluorobenzyl mercaptan but without the thiol functional group, was also used for functionalization. However, as shown in the blue curve in Figure 2c, no F peak was observed in XPS, indicating the functionalization using fluorobenzene was not successful. This difference between 4-fluorobenzyl mercaptan and fluorobenzene strongly suggests that functionalization on MoS_2 MLs relies on thiol functional group, without which, ligands could only be physisorbed on the surface and thus can be easily washed off.

In addition to the appearance of the F peak in XPS, the S XPS peak was broadened and slightly shifted to lower binding energy after 4-fluorobenzyl mercaptan functionalization (Figure 2d). The peak deconvolution of as-synthesized MoS_2 MLs reveals the presence of two S doublets, indicating two chemical environments: a major doublet with a $S2p_{3/2}$ peak at 162.7 eV and a minor doublet with a $S2p_{3/2}$ peak at 162.1 eV. After functionalization, the intensity of the minor doublet ($S2p_{3/2}$ peak at 162.1 eV) was significantly enhanced, changing the ratio between the two S doublets. Accordingly, the overall S spectra also broadened and shifted to a lower binding energy. It is suspected that the enhancement of the minor doublet ($S2p_{3/2}$ peak at 162.1 eV) is due to the thiol-containing ligand conjugating to MoS_2 surface. It is important to note that the $S2p_{3/2}$ peak of free 4-fluorobenzyl mercaptan appears at 162.7 eV while the enhanced peak of functionalized MoS_2 MLs appears at 162.0 eV. A similar difference has been reported for thiol-containing molecules self-assembling on gold surface.[39] In that case, both physisorbed and chemisorbed thiol molecules are resolved in XPS, with physisorbed molecules covering the top of the first chemisorbed layer. The $S2p_{3/2}$ peaks near 163 eV are attributed to unbound physisorbed thiol molecules, whereas the $S2p_{3/2}$ peaks near 162 eV are assigned to chemisorbed thiol molecules forming a covalently bound film to the gold substrate. For the MoS_2 functionalization herein, because the $S2p_{3/2}$ peak in thiol molecules overlaps with $S2p_{3/2}$ peak in MoS_2 (both near 162.7 eV), it is hard to differentiate whether there are physisorbed molecules on MoS_2 surface. Nevertheless, the clear emergence of S component ($S2p_{3/2}$ peak) at 162.0 eV in the functionalized MoS_2 ML sample suggests there is a layer of 4-fluorobenzyl mercaptan molecules covalently bonding to MoS_2 surface via thiol conjugation.

With FTIR and XPS results both indicating thiol functional group conjugating to MoS_2 monolayer surface, we aim to provide a more thorough investigation regarding what enables and controls the functionalization. Theoretical calculations have suggested that sulfur vacancies could be the key to thiol conjugation.[16,36] Therefore, we designed experiments to characterize and purposely tune the amount of S vacancies in 2H-MoS_2 MLs, and examine if different amounts of S vacancies would lead to different degrees of functionalization. Annealing MoS_2 in a sulfur environment has been reported to partially compensate S vacancies.[40] We annealed the MoS_2 ML sample with sulfur vapor at 550 ˚C for 2 h in a CVD chamber, and compared the amount of S vacancies before and after annealing for the same MoS_2 MLs sample using electron paramagnetic resonance (EPR), a technique that is sensitive to unpaired electrons and has been used to reveal the concentration of MoS_2 S vacancies.[41] According to literature, the signal at $g = 2.00$ originates from S vacancies in MoS_2, with an enhanced signal suggesting increased S vacancy concentration.[41] As shown in Figure 3a, after S annealing experiment, the EPR peak at $g = 2.00$

decreased dramatically from the black curve to the red curve, demonstrating we have successfully reduced the amount of S vacancies.

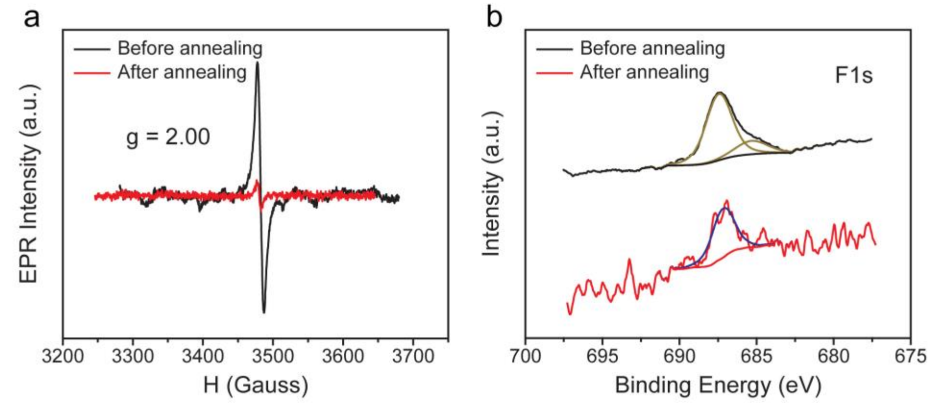

Figure 4.3. (a) EPR spectra for the same MoS_2 ML sample measured before (black) and after (red) sulfur annealing. The figure shows sulfur annealing caused a dramatic decrease in intensity. (b) High-resolution XPS of the F1s region for functionalized as-grown MoS_2 ML (black) and functionalized annealed MoS_2 ML (red) after normalizing to the same Mo peak.

To investigate how the decreased S vacancy concentration affects the degree of MoS_2 functionalization, we conducted the same 4-fluorobenzyl mercaptan functionalization experiment on annealed MoS_2 ML. Figure 3b compares the high-resolution F1s XPS spectra for functionalized MoS_2 ML (black) and functionalized annealed MoS_2 ML (red) after normalizing to the same Mo peak intensities. Thus, the area of integrated F peak reflects the degree of 4-fluorobenzyl mercaptan functionalization. The sulfur annealed MoS_2 ML indeed displays a much smaller F peak after functionalization than as-synthesized MoS_2 ML, indicating fewer ligands and a smaller degree of functionalization for annealed MoS_2. This comparison confirms our hypothesis that the degree of thiol conjugation is dependent on the S vacancies present on the basal plane of MoS_2 layers, and can be tuned effectively by adjusting the amount of S vacancies via S annealing.

We also demonstrated this functionalization approach could be readily applied to other thiol-containing molecules besides 4-fluorobenzyl mercaptan. For example, 5-(trifluoromethyl) pyridine-2-thiol contains a thiol functional group as well as characteristic F and N elements (see Figure S1). XPS spectra of MoS_2 ML functionalized with this molecule clearly reveal the presence of F peak (Figure S1), confirming the functionalization could be successfully extended to other thiol-containing molecules. For ligands like 1,5-pentanedithol (see Figure S2) that do not contain characteristic marker elements like F and N, MoS_2 ML functionalized with such molecules displayed an additional enhancement of the second S component (the $S2p_{3/2}$ peak positioned near 162 eV) in the XPS S spectra (Figure S2). It is attributed to the thiol functional group conjugating to MoS_2 surface, consistent with what was observed in 4-fluorobenzyl mercaptan functionalized MoS_2 ML (Figure 2d). Moreover, this functionalization approach can be applied to other types of MoS_2, such as monolayer or few-layer MoS_2 mechanically exfoliated from single crystals, and CVD grown MoS_2 nanoflowers.[4] Single- and multilayer MoS_2 were mechanically exfoliated onto

Si/SiO_2 substrate, where the same 4-fluorobenzyl mercaptan molecule was used for functionalization. Figure S3 displays the distinct F1s peak that confirmed the successful ligand functionalization on mechanically exfoliated MoS_2, similar to what was observed on CVD grown MoS_2 MLs. We also performed the same functionalization on MoS_2 nanoflower samples grown on graphite substrates synthesized via CVD.[4] As shown in the FTIR spectrum (Figure S4), peaks corresponding to 4-fluorobenzyl mercaptan ligand were clearly resolved, confirming the successful functionalization of MoS_2 nanoflowers.

After structural characterization and functionalization mechanism investigation, we then systematically examined the effect of ligand functionalization on the physical and chemical properties of MoS_2 MLs. Photoluminescence (PL) experiments were conducted to compare the same MoS_2 ML sample at the same spot before and after functionalization. Figure 4a reveals a significantly enhanced PL response for CVD MoS_2 ML after 4-fluorobenzyl mercaptan functionalization. Previous work has reported using thiol chemistry to repair sulfur vacancies and improve MoS_2 charge transport properties.[36] Thus, it is suspected the conjugated thiol molecules that bind to the basal plane at S vacancies can repair or passivate sulfur vacancies of MoS_2 ML, eliminating defect-mediated nonradiative recombination, thus resulting in enhanced PL response.[42,43] Importantly, this enhancement is not only seen in 4-fluorobenzyl mercaptan functionalized MoS_2 MLs, but has been consistently observed in other types of functionalized MoS_2 samples. Figure 3b compares the PL responses of 1,5-pentanedithol functionalized MoS_2 MLs before and after functionalization, and Figure 3c shows 4-fluorobenzyl mercaptan functionalized mechanically exfoliated (ME) MoS_2. In all cases, a significant PL enhancement was observed, suggesting the generality of such functionalization to improve photoluminescence response of MoS_2.

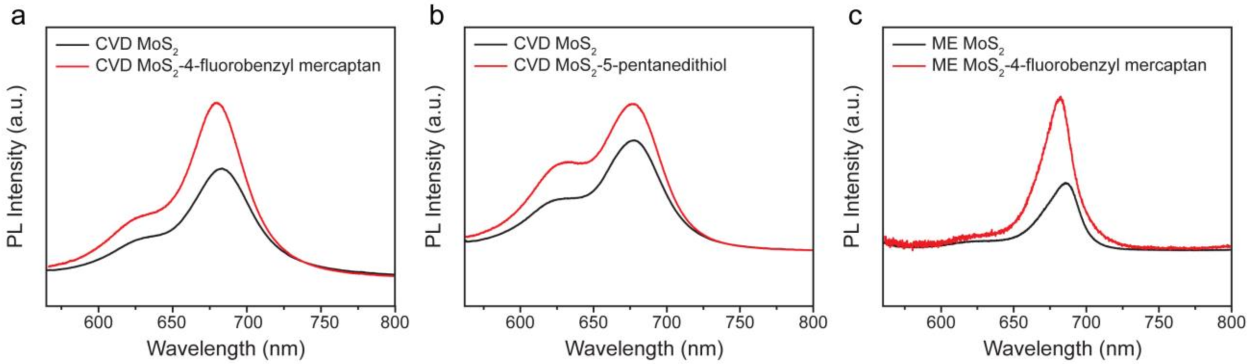

Figure 4.4. Photoluminescence spectra of as-prepared MoS_2 (black) and ligand functionalized MoS_2 (red), with functionalized MoS_2 showing a consistent enhancement in PL response.

Besides optical and electronic applications, MoS_2 is also a promising earth-abundant electrocatalyst for hydrogen evolution reaction (HER).[4,5,44,45] We synthesized MoS_2 nanoflowers on graphite electrodes using CVD,[4] then measured the electrocatalytic performance of the same electrode before and after ligand functionalization (see Experimental Section for details). Figure 5a compares the polarization curves for MoS_2 measured before (black) and after (red) 4-fluorobenzyl mercaptan functionalization. A dramatic decrease in catalytic activity was observed for functionalized MoS_2 nanoflowers sample, with the voltage required to reach 10 mA/cm^2 increased significantly from 0.33 V to 0.44 V vs. reversible hydrogen electrode (RHE). The decreased HER catalytic activity is further illustrated by comparing the Tafel slopes, a parameter that provides insights into the intrinsic activity and catalytic mechanisms of the catalyst. The Tafel slope increased from 136 mV/decade (black curve) before functionalization to 187 mV/decade (red curve) after functionalization (Figure 5b). Experimental and computational studies have shown that both the edge sites and the sulfur vacancies on MoS_2 basal plane contribute to HER catalytic activity.[19,46] Therefore, this decrease in HER performance serves as additional evidence demonstrating thiol conjugation on the edge sites and/or sulfur vacancies on MoS_2 basal plane, which results in a significant reduction in available active sites for HER catalysis.

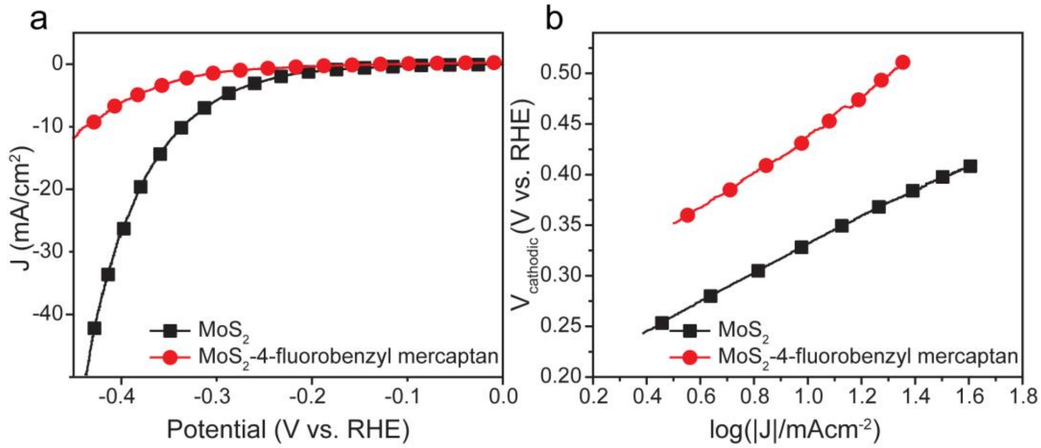

Figure 4.5. Electrochemical characterization of MoS_2 nanoflowers for HER electrocatalysis before and after functionalization. (a) Polarization curves and (b) Tafel analysis of the same MoS_2 sample measured before (black) and after (red) 4-fluorobenzyl mercaptan functionalization.

Ligand functionalization with different thiol-containing bi-functional linkers also provides new opportunities for introducing different functional groups onto the basal plane of MoS_2 MLs and enables a wider range of applications. In particular, MoS_2 functionalization provides a promising, facile approach for preparing molecularly linked MoS_2-based heterostructures that can extend the applicability of MoS_2 MLs. Utilizing a dithiol organic molecule, we demonstrate the creation of MoS_2-quantum dots (QDs) heterostructures. QDs are a class of zero-dimensional, quantum-confined materials with intriguing optical and physical properties.[47,48] The QD band gap and properties can be effectively controlled by changing the size of QDs. QD heterostructures are both promising solar energy conversion materials and interesting model systems for fundamental charge transfer investigation. MoS_2-QD heterostructures are particularly appealing because they couple 2D and 0D materials that may lead to unique optical and physical properties, and new applications in optoelectronic devices.

Here, we chose 1,5-pentanedithiol as the ligand to functionalize MoS_2 surface and link to PbSe QDs. This organic molecule has two thiol groups, one conjugates to MoS_2 surface, while the other binds to QDs due to the high affinity of QDs toward thiol moieties.[47,49] The 4 nm diameter PbSe QDs were synthesized using a hot-injection approach.[50] We immersed 1,5-pentanedithol functionalized mechanically exfoliated single- and multilayer MoS_2 sample on silicon substrates in a suspension of PbSe QDs dispersed in toluene. After 48 h, the MoS_2 substrate was washed off in toluene, ethanol, acetone and isopropanol to remove physisorbed QDs. Transmission electron microscopy (TEM) was then used to examine the MoS_2 surface (see Experimental Section for details). Selected-area electron diffraction (Figure 6a inset) confirmed the observed surface is the basal plane of single crystal 2H-MoS_2. As shown in Figure 6a, b, the entire MoS_2 basal plane has been completely covered with PbSe QDs. Note the MoS_2 sheets in Figure 6b were rolled up at the edge. From that edge, a high-resolution TEM image containing both lattice resolved MoS_2 and PbSe QDs can be acquired and the corresponding FFT pattern is shown in Figure 6b inset. The lattice spacings are determined to be 0.615 nm and 0.31 nm that match well with the MoS_2 (002) and PbSe (002) spacings, respectively. Energy-dispersive X-ray spectroscopy (EDS) also revealed the presence of Mo, S, Pb and Se elements (Figure 6c), further confirming the MoS_2-PbSe heterostructures. To prove PbSe QDs are indeed linked to MoS_2 surface through 1,5-pentanedithiol rather than physisorbed, we conducted FTIR on the MoS_2-PbSe heterostructures, and observed clear peaks that correspond very well with the peaks from the 1,5-pentanedithol molecule (Figure 6d). A control experiment that attached PbSe QDs onto a non-functionalized MoS_2 surface showed a much lower QD coverage, confirming that the functionalization plays a key role in creating MoS_2-PbSe QD heterostructures. Moreover, the high coverage of QDs everywhere on the MoS_2 sheets further demonstrates that the thiol-containing molecules are conjugating not only to the edges but also to the basal plane of MoS_2.

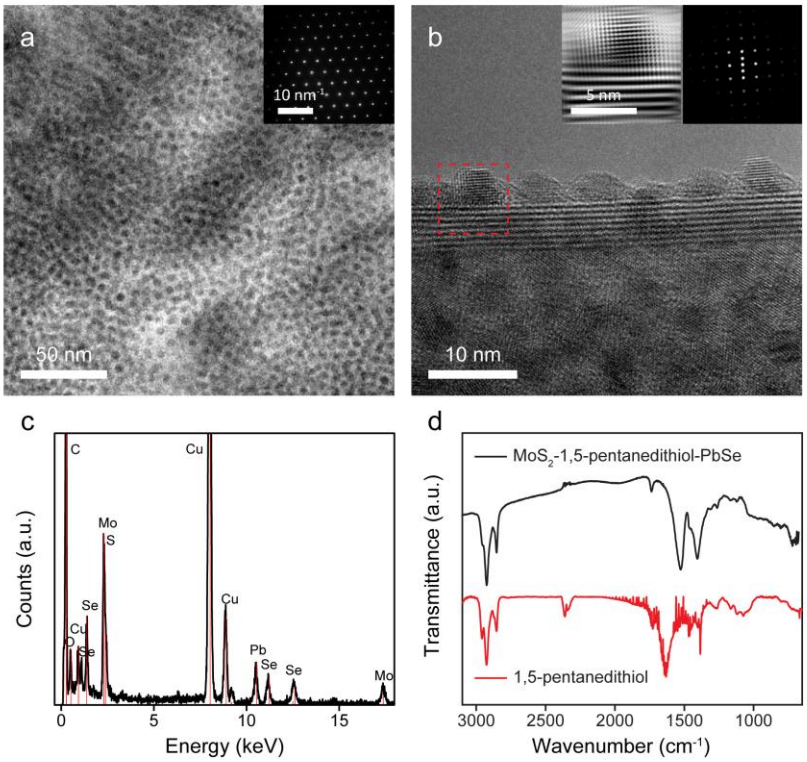

Figure 4.6. (a-b) TEM images of MoS_2-PbSe QD heterostructures at different magnifications with selected-area electron diffraction shown in Figure 6a inset. A fast Fourier transform (FFT)-filtered high-resolution TEM image and its corresponding FFT pattern are shown in Figure 6b inset. (c) EDS spectrum of the MoS_2-PbSe QD heterostructures. (d) FTIR spectra of 1,5-pentanedithiol linked MoS_2-PbSe QD heterostructure (black) in comparison with free 1,5-pentanedithiol ligand (red).

4.5 Conclusions

In conclusion, we have demonstrated a facile and effective approach to functionalize the basal plane of 2H-MoS_2 using thiol conjugation to the numerous S vacancies commonly found in MoS_2 materials. Thorough characterization using FTIR and XPS has confirmed the successful functionalization and revealed various changes in MoS_2 chemical environments. We demonstrated that S vacancies in MoS_2 play the key role in thiol conjugation on the basal plane of MoS_2, and that controlling S vacancies on MoS_2 basal plane can effectively tune the degree of thiol conjugation. Enhanced photoluminescence response and decreased catalytic activity toward HER were further observed and attributed to the passivation of sulfur vacancies. Furthermore, the successful creation of a high surface coverage of PbSe QDs on a functionalized MoS_2 basal plane surface using dithiol linker molecules serves as a proof-of-concept for creating new MoS_2-based heterostructures. This work provides new insights into the surface chemistry of MoS_2 and 2D TMDC materials, lays the foundation for further studies of MoS_2 surface chemistry on the basal plane, and facilitates the creation of MoS_2 monolayers with well controlled properties for different applications.

4.6 References

(1) Chhowalla, M.; Shin, H. S.; Eda, G.; Li, L. J.; Loh, K. P.; Zhang, H. *Nat. Chem.* **2013**, *5*, 263.

(2) Xu, M. S.; Liang, T.; Shi, M. M.; Chen, H. Z. *Chem. Rev.* **2013**, *113*, 3766.

(3) Butler, S. Z.; Hollen, S. M.; Cao, L. Y.; Cui, Y.; Gupta, J. A.; Gutierrez, H. R.; Heinz, T. F.; Hong, S. S.; Huang, J. X.; Ismach, A. F.; Johnston-Halperin, E.; Kuno, M.; Plashnitsa,

V. V.; Robinson, R. D.; Ruoff, R. S.; Salahuddin, S.; Shan, J.; Shi, L.; Spencer, M. G.; Terrones, M.; Windl, W.; Goldberger, J. E. *ACS Nano* **2013**, *7*, 2898.

(4) Lukowski, M. A.; Daniel, A. S.; Meng, F.; Forticaux, A.; Li, L. S.; Jin, S. *J. Am. Chem. Soc.* **2013**, *135*, 10274.

(5) Benck, J. D.; Hellstern, T. R.; Kibsgaard, J.; Chakthranont, P.; Jaramillo, T. F. *ACS Catal.* **2014**, *4*, 3957.

(6) Mattheis, L. F. *Phys. Rev. B* **1973**, *8*, 3719.

(7) Mak, K. F.; Lee, C.; Hone, J.; Shan, J.; Heinz, T. F. *Phys. Rev. Lett.* **2010**, *105*, 136805.

(8) Mouri, S.; Miyauchi, Y.; Matsuda, K. *Nano. Lett.* **2013**, *13*, 5944.

(9) Yin, Z. Y.; Li, H.; Li, H.; Jiang, L.; Shi, Y. M.; Sun, Y. H.; Lu, G.; Zhang, Q.; Chen, X. D.; Zhang, H. *ACS Nano* **2012**, *6*, 74.

(10) Lee, H. S.; Min, S. W.; Chang, Y. G.; Park, M. K.; Nam, T.; Kim, H.; Kim, J. H.; Ryu, S.; Im, S. *Nano. Lett.* **2012**, *12*, 3695.

(11) Wu, S. F.; Buckley, S.; Schaibley, J. R.; Feng, L. F.; Yan, J. Q.; Mandrus, D. G.; Hatami, F.; Yao, W.; Vuckovic, J.; Majumdar, A.; Xu, X. D. *Nature* **2015**, *520*, 69.

(12) Radisavljevic, B.; Radenovic, A.; Brivio, J.; Giacometti, V.; Kis, A. *Nat. Nanotechnol.* **2011**, *6*, 147.

(13) Presolski, S.; Pumera, M. *Materials Today* **2016**, *19*, 140.

(14) Chen, X.; McDonald, A. R. *Adv. Mater.* **2016**. DOI: 10.1002/adma.201505345.

(15) Ataca, C.; Ciraci, S. *J. Phys. Chem. C* **2011**, *115*, 13303.

(16) Tang, Q.; Jiang, D. E. *Chem. Mater.* **2015**, *27*, 3743.

(17) Chou, S. S.; De, M.; Kim, J.; Byun, S.; Dykstra, C.; Yu, J.; Huang, J. X.; Dravid, V. P. *J. Am. Chem. Soc.* **2013**, *135*, 4584.

(18) Liu, T.; Wang, C.; Gu, X.; Gong, H.; Cheng, L.; Shi, X. Z.; Feng, L. Z.; Sun, B. Q.; Liu, Z. *Adv. Mater.* **2014**, *26*, 3433.

(19) Jaramillo, T. F.; Jorgensen, K. P.; Bonde, J.; Nielsen, J. H.; Horch, S.; Chorkendorff, I. *Science* **2007**, *317*, 100.

(20) Canfield, D.; Parkinson, B. A. *J. Am. Chem. Soc.* **1981**, *103*, 1279.

(21) Wang, T. Y.; Zhu, R. Z.; Zhuo, J. Q.; Zhu, Z. W.; Shao, Y. H.; Li, M. X. *Anal. Chem.* **2014**, *86*, 12064.

(22) Goncalves, R. H.; Fiel, R.; Soares, M. R. S.; Schreiner, W. H.; Silva, C. M. P.; Leite, E. R. *Chem-Eur. J.* **2015**, *21*, 15583.

(23) Kim, J. S.; Yoo, H. W.; Choi, H. O.; Jung, H. T. *Nano. Lett.* **2014**, *14*, 5941.

(24) Backes, C.; Berner, N. C.; Chen, X.; Lafargue, P.; LaPlace, P.; Freeley, M.; Duesberg, G. S.; Coleman, J. N.; McDonald, A. R. *Angew. Chem. Int. Ed.* **2015**, *54*, 2638.

(25) Nguyen, E. P.; Carey, B. J.; Ou, J. Z.; van Embden, J.; Della Gaspera, E.; Chrimes, A. F.; Spencer, M. J. S.; Zhuiykov, S.; Kalantar-zadeh, K.; Daeneke, T. *Adv. Mater.* **2015**, *27*, 6225.

(26) Voiry, D.; Goswami, A.; Kappera, R.; Silva, C. D. C. E.; Kaplan, D.; Fujita, T.; Chen, M. W.; Asefa, T.; Chhowalla, M. *Nat. Chem.* **2015**, *7*, 45.

(27) Knirsch, K. C.; Berner, N. C.; Nerl, H. C.; Cucinotta, C. S.; Gholamvand, Z.; McEvoy, N.; Wang, Z. X.; Abramovic, I.; Vecera, P.; Halik, M.; Sanvito, S.; Duesberg, G. S.; Nicolosi, V.; Hauke, F.; Hirsch, A.; Colernan, J. N.; Backes, C. *ACS Nano* **2015**, *9*, 6018.

(28) Zhou, L.; He, B. Z.; Yang, Y.; He, Y. G. *RSC Adv.* **2014**, *4*, 32570.

(29) Raybaud, P.; Hafner, J.; Kresse, G.; Toulhoat, H. *Phys. Rev. Lett.* **1998**, *80*, 1481.

(30) Cheng, Z. H.; He, B. Z.; Zhou, L. *J. Mater. Chem. A* **2015**, *3*, 1042.

(31) Jiang, S. D.; Tang, G.; Bai, Z. M.; Wang, Y. Y.; Hu, Y.; Song, L. *RSC Adv.* **2014**, *4*, 3253.

(32) Hong, J. H.; Hu, Z. X.; Probert, M.; Li, K.; Lv, D. H.; Yang, X. N.; Gu, L.; Mao, N. N.; Feng, Q. L.; Xie, L. M.; Zhang, J.; Wu, D. Z.; Zhang, Z. Y.; Jin, C. H.; Ji, W.; Zhang, X. X.; Yuan, J.; Zhang, Z. *Nat. Commun.* **2015**, *6*, 6293.

(33) Qiu, H.; Xu, T.; Wang, Z. L.; Ren, W.; Nan, H. Y.; Ni, Z. H.; Chen, Q.; Yuan, S. J.; Miao, F.; Song, F. Q.; Long, G.; Shi, Y.; Sun, L. T.; Wang, J. L.; Wang, X. R. *Nat. Commun.* **2013**, *4*, 2642.

(34) Zhou, W.; Zou, X. L.; Najmaei, S.; Liu, Z.; Shi, Y. M.; Kong, J.; Lou, J.; Ajayan, P. M.; Yakobson, B. I.; Idrobo, J. C. *Nano Lett.* **2013**, *13*, 2615.

(35) Le, D.; Rawal, T. B.; Rahman, T. S. *J. Phys. Chem. C* **2014**, *118*, 5346.

(36) Yu, Z. H.; Pan, Y. M.; Shen, Y. T.; Wang, Z. L.; Ong, Z. Y.; Xu, T.; Xin, R.; Pan, L. J.; Wang, B. G.; Sun, L. T.; Wang, J. L.; Zhang, G.; Zhang, Y. W.; Shi, Y.; Wang, X. R. *Nat. Commun.* **2014**, *5*, 5290.

(37) Komsa, H. P.; Kurasch, S.; Lehtinen, O.; Kaiser, U.; Krasheninnikov, A. V. *Phys. Rev. B* **2013**, *88*, 035301.

(38) Najmaei, S.; Liu, Z.; Zhou, W.; Zou, X. L.; Shi, G.; Lei, S. D.; Yakobson, B. I.; Idrobo, J. C.; Ajayan, P. M.; Lou, J. *Nat. Mater.* **2013**, *12*, 754.

(39) Castner, D. G.; Hinds, K.; Grainger, D. W. *Langmuir* **1996**, *12*, 5083.

(40) Hsu, T. M.; Lee, J. S.; Hwang, H. L. *J Appl Phys* **1990**, *68*, 283.

(41) Cai, L.; He, J. F.; Liu, Q. H.; Yao, T.; Chen, L.; Yan, W. S.; Hu, F. C.; Jiang, Y.; Zhao, Y. D.; Hu, T. D.; Sun, Z. H.; Wei, S. Q. *J. Am. Chem. Soc.* **2015**, *137*, 2622.

(42) Han, H. V.; Lu, A. Y.; Lu, L. S.; Huang, J. K.; Li, H. N.; Hsu, C. L.; Lin, Y. C.; Chiu, M. H.; Suenaga, K.; Chu, C. W.; Kuo, H. C.; Chang, W. H.; Li, L. J.; Shi, Y. M. *ACS Nano* **2016**, *10*, 1454.

(43) Amani, M.; Lien, D. H.; Kiriya, D.; Xiao, J.; Azcatl, A.; Noh, J.; Madhvapathy, S. R.; Addou, R.; Santosh, K. C.; Dubey, M.; Cho, K.; Wallace, R. M.; Lee, S. C.; He, J. H.; Ager, J. W.; Zhang, X.; Yablonovitch, E.; Javey, A. *Science* **2015**, *350*, 1065.

(44) Ding, Q.; Meng, F.; English, C. R.; Caban-Acevedo, M.; Shearer, M. J.; Liang, D.; Daniel, A. S.; Hamers, R. J.; Jin, S. *J. Am. Chem. Soc.* **2014**, *136*, 8504.

(45) Ding, Q.; Zhai, J. Y.; Caban-Acevedo, M.; Shearer, M. J.; Li, L. S.; Chang, H. C.; Tsai, M. L.; Ma, D. W.; Zhang, X. W.; Hamers, R. J.; He, H.; Jin, S. *Adv. Mater.* **2015**, *27*, 6511.

(46) Li, H.; Tsai, C.; Koh, A. L.; Cai, L. L.; Contryman, A. W.; Fragapane, A. H.; Zhao, J. H.; Han, H. S.; Manoharan, H. C.; Abild-Pedersen, F.; Norskov, J. K.; Zheng, X. L. *Nat. Mater.* **2016**, *15*, 48.

(47) Selinsky, R. S.; Ding, Q.; Faber, M. S.; Wright, J. C.; Jin, S. *Chem. Soc. Rev.* **2013**, *42*, 2963.

(48) Watson, D. F. *J. Phys. Chem. Lett.* **2010**, *1*, 2299.

(49) Kongkanand, A.; Tvrdy, K.; Takechi, K.; Kuno, M.; Kamat, P. V. *J. Am. Chem. Soc.* **2008**, *130*, 4007.

(50) Wehrenberg, B. L.; Wang, C. J.; Guyot-Sionnest, P. *J. Phys. Chem. B* **2002**, *106*, 10634.

Chapter 5

Synthesis and Properties of Epitaxial PbSe QD–TiO_2 Nanoscale Heterostructures for Solar Energy Conversion

5.1 Abstract

In this work, we have developed a facile approach to synthesize epitaxial PbSe–TiO_2 quantum dot nanoscale heterostructures (QDH) via hot injection. High resolution Tramsmission electron microscopy (HRTEM) confirmed the direct lattice connection between PbSe QDs and TiO_2 nanomatrials. This approach could be readily extended to TiO_2 with different morphologies (nanoparticles, nanosheets, nanorods), on different substrates (FTO, titanium foil, glass), and on other metal oxide semiconductors, such as SnO_2 and Fe_2O_3. In all caes, excellent quantum dot coverage with narrow size distribution have been achieved. The growth mechanism has been investigated with approaches to effectively tune the size of grown PbSe quantum dots. Significant enhancement in TiO_2 absorption spectra was observed due to the light absorption of PbSe QDs, and faster charge transfer kinetics from the donor and acceptor materials is expected because of the direct lattice connection in the epitaxial heterostructure.

5.2 Introduction

With the rapidly increasing global energy consumption, the need for materials with high solar energy conversion efficiencies and low costs grows. In particular, quantum dot nanoscale heterostructures (QDHs) are a class of materials that are useful for both fundamental investigation of charge transfer and potentially useful for integration into solar energy conversion devices. Unlike other heterostructures, nanoscale heterostructures containing QDs have their unique advantages. First, due to the small dimensions of QDs, electrons and holes are largely quantum confined.[1] Therefore, the band gap of QDs and the band alignment of nanoscale heterostructures can be tuned by simply adjusting the relative size of the donor-acceptor materials.[2,3] Second, small dimensions allow the formation of epitaxial junctions between dissimilar materials because the effects of lattice-mismatch strains are minimized. The size scale of nanomaterials is usually far below the critical material thickness for coherent heteroepitaxy so nanoscale heterojunctions can tolerate large lattice mismatches before defects are observed.[4,5] As a result, epitaxial single crystalline nanoscale heterostructures can be synthesized using combinations of materials that would be impossible as bulk or thin film junctions. Third, multiple exciton generation (MEG) effect has been demonstrate in several QD based solar cells.[6-9] The possibility of utilizing excess photon energy rather than being lost as heat can potentially exceed the Shockley–Queisser efficiency limit. Among all kinds of quantum dots, PbS and PbSe QDs are attracting a lot of attention because of their large Bohr radius,[10-13] large ground state cross section of absorption (10–15 cm^{-2}) and long excitonic lifetime (200–800 ns).[14,15]

Given the many advantages of QDHs, they have been intensively investigated over the last few years. There are mainly three primary types of QDHs: junctions formed by proximal contact, junctions formed by molecular linkers, and linker-free epitaxial attachment. Figure 5.1[16] illustrates these different types of QDHs in comparison with a conventional epitaxial planar heterojunction (Figure 5.1a). Materials in proximally contacted heterostructures are physisorbed to each other, sometimes referred to as “direct attachment” or “direct adsorption” heterostructures, the acceptor and donor materials are synthesized separately, but are not chemically linked together (Figure 5.1b). Figure 5.2 is an example of proximally contacted QDH where PbS QDs are mixed with TiO_2 nanobelts.

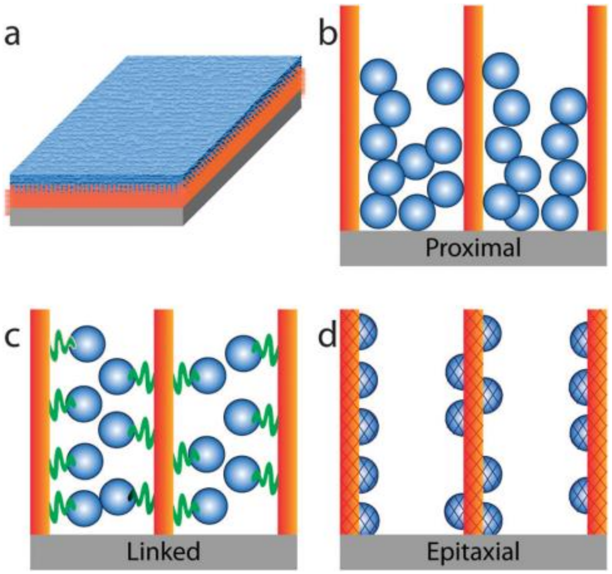

Figure 5.1. Planar heterostructure (a) and quantum dot nanoscale heterostructures (QDHs) where the donor material is shown in blue and the acceptor in red. Using a QD donor and a NW acceptor as an example structure, the QDH can be (b) proximally contacted, (c) chemically-linked, or (d) epitaxial.[16]

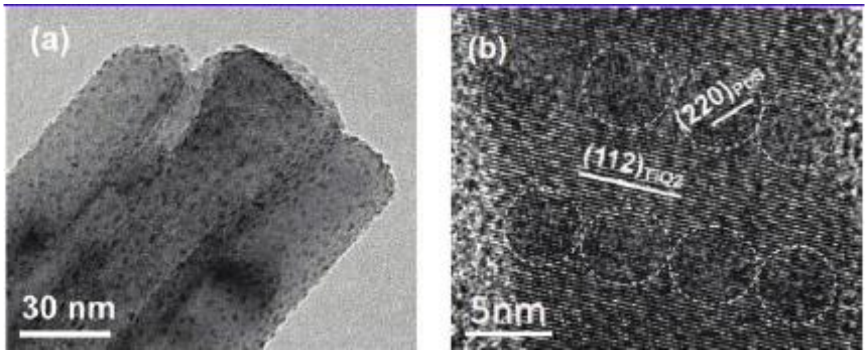

Figure 5.2. An example of PbS QDs physisorbed to TiO_2 nanobelts via proximal contact.[17]

Materials in linked heterostructures are directly connected *via* organic or inorganic linking molecules, but do not have direct lattice connection (Figure 5.1c). Charge transfer between acceptor and donor materials can be facilitated through an organic or inorganic molecular linker (see schematic Fig. 5a). As with proximal heterostructures, the acceptor and donor materials for these QDHs are synthesized separately. However, for chemically-linked or tethered junctions, the donor material is added to the acceptor in the presence of a bifunctional molecule exhibiting preferential binding of the different groups to the acceptor and donor materials, respectively. The thiol (-SH) group is a good ligand to bind to the surface of metal chacolgenide QDs and the carboxylic acid group (-COOH) is a good ligand to most metal oxide surface; therefore, the common choice of the bifunctional linker for QDHs are molecules that contain these two functional groups.[18] One commonly used linker is 3-mercaptopropionic acid (MPA), a bifunctional linker bearing carboxylate and thiol functional groups.[19-21] Several commonly used linker molecules are shown in the scheme below (Figure 5.3).

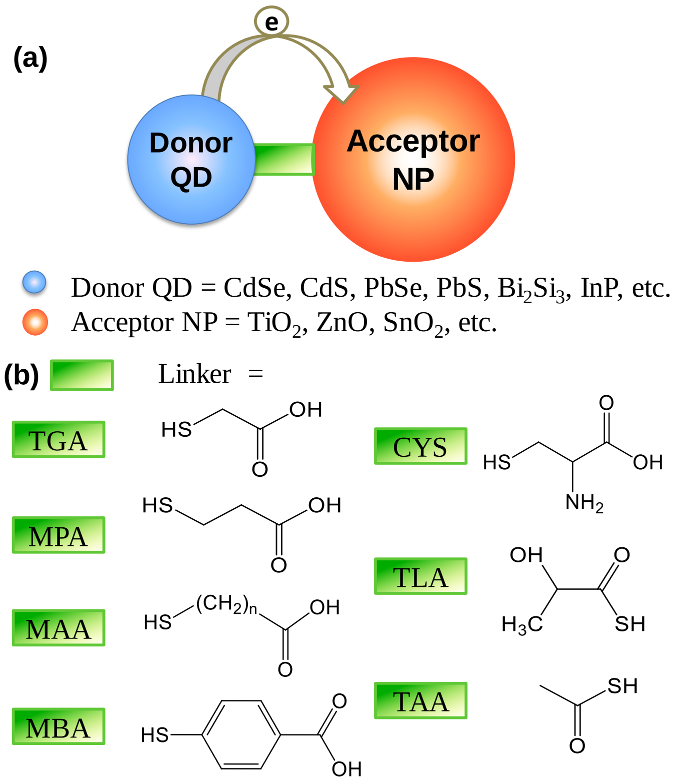

Figure 5.3. (a) Schematics of QDHs connected by chemical linkers. (b) Some common examples of the chemical linkers.[16]

Materials in linker-free heterostructures are epitaxially connected, therefore sharing a crystalline interface (Figure 5.1d). It is the most efficient configuration for charge-transfer across heterojunctions is through high-quality epitaxial interfaces. Unlike proximal or chemically linked QDHs, epitaxy promotes direct electronic communication between the donor and acceptor, and are the most technically challenging to synthesize among the heterostructures discussed. The synthesis and charge transfer properties of directly attached and linked QDHs have been widely investigated. However, although epitaxial QDHs have interface with best quality, there are still much fewer reports on the synthesis of definitive epitaxial QDHs,[2,22-24] and their charge transfer properties have not been investigated systematically. The purpose of my research is to synthesize QDHs with high-quality, epitaxial interfaces *via* a simple colloidal solution method, extend this approach to integrate QDs with a broad range of acceptor nanomaterials made by diverse synthesis routes, and investigate the fundamental coherent charge transfer dynamics in these systems using spectroscopy.

5.3 Materials and Methods

Materials. Trioctylphosphine (TOP, 90%), 90% oleic acid (OA), ≥ 99 % diphenyl ether (DiPE), ≥ 99 % lead (II) acetate $Pb(Ac)_2$, and 99.99 % selenium powder were purchased from Sigma Aldrich and used without further purification. The 1 M trioctylphosphine−selenium complex (TOP−Se) was prepared by following an established synthesis.[25]

5.3.1 Synthesis of PbSe QDs

In a typical synthesis,[25] 0.325 g lead acetate, 6 mL diphenyl ether, 4 mL trioctylphosphine are mixed together in a three-neck flask and heated to 85 °C under vacuum. After 30 min, the mixture is heated up to 125 °C under nitrogen flow, when 0.85 mL of 1 M trioctylphosphine selenide (TOP−Se) is rapidly injected into the flask. After 4 min, 12 mL ethanol is added to quench the QD growth.

5.3.2 Synthesis of PbSe-TiO_2 heterostructure

The setup of reaction follows our previous report of PbSe−Fe_2O_3 heterostructure synthesis.[24] Briefly, FTO substrate is placed into a home-built glass holder with FTO and TiO_2 nanorod (NR) side facing down. This holder is then placed in a three-necked cylindrical flask on a Schlenk line. In a typical synthesis,[25] 0.325 g lead acetate, 6 mL diphenyl ether, 4 mL trioctylphosphine are mixed together in another flask and heated to 85 °C under vacuum. After 30 min, the mixture is allowed to cool to room temperature and then transferred *via* a canular to the flask containing the dehydrated TiO_2 NR substrate. The reactant mixture in the presence of the NR substrate is then heated up to 125 °C under nitrogen, when 0.85 mL of 1 M trioctylphosphine selenide (TOP−Se) is rapidly injected into the flask. After 4 min, 12 mL ethanol is added to quench the QD growth. The substrate is then removed from the glassware and aggressively rinsed with toluene, ethanol, and acetone to remove excess reactants and any unbound PbSe QDs from the surface of the TiO_2 NRs.

5.4 Results and Discussion

5.4.1 Synthesis of PbSe-TiO_2 heterostructure

As the nature of the TiO_2 surface has a strong influence on heterostructure growth, some additional treatments of TiO_2 surface are required to enable the direct nucleation of QDs on it. Doctor-bladed TiO_2 nanoparticle films are mostly ready as-prepared; post-annealing in air at 500 °C for 1 h is adequate to remove any binders or other organics left on surface.[23] For TiO_2 nanorods grown on FTO, chemical etching using a solution containing $NH_3 \cdot H_2O:H_2O_2:H_2O$ at a molar ratio of 1:1:5 for 30 minutes prior to heterostructure growth is shown to be critical for the direct nucleation of QDs on TiO_2 surface. Long time etching following this recipe can etch away TiO_2,[26] yet 30 minutes is just sufficient to roughen the surface, making the surface more favorable for QDs to nucleate and grow. Moreover, dehydration of substrate has also been shown to play a significant role on the nucleation of QDs and the formation of high-quality, epitaxial heterointerfaces.[24] As demonstrated in our previous results,[24] longer dehydration time increases the density of QDs on the surface and decreases the QD diameter distributions. Therefore, heating the substrate-glassware setup to 350 °C in a sand bath under dynamic vacuum (< 20 mTorr) on a Schlenk line for 3–5 hours is always conducted prior to the heterostructure growth. Furthermore, treating as-synthesized TiO_2 NRs with UV light and etching them with O_2 plasma are also shown to help remove surface contamination, improve wetting by suspensions in polar solvents, improve the quality of epitaxial interface, and increase surface coverage of QDs significantly.[27,28]

The setup of reaction follows our previous-reported PbSe–Fe_2O_3 heterostructure synthesis,[24] with one representative glassware illustration shown in Figure 5.4. Briefly, FTO substrate is placed into a home-built glass holder with FTO and TiO_2 NR side facing down. This holder is then placed in a three-necked cylindrical flask on a Schlenk line, and heated to 350 °C in a sand bath under dynamic vacuum (< 20 mTorr) for up to 5 h. In another flask, 0.325 g lead oleate acetate, 6 mL diphenyl ether, 4 mL trioctylphosphine are mixed together and heated to 85 °C under vacuum. After 30 min, the mixture is allowed to cool to room temperature and then transferred *via* a canular to the flask containing the dehydrated TiO_2 NR substrate. The reactant mixture in the presence of the NR substrate is then heated up to 125 °C under nitrogen, when 0.85 mL 1 M trioctylphosphine selenide (TOP−Se) is rapidly injected into the flask. After 4 min, 12 mL ethanol is used to quench QD growth. The substrate is then removed from the glassware and aggressively rinsed with toluene, ethanol, and acetone to remove excess reactants and any unbound PbSe QDs from the surface of the TiO_2 NRs.

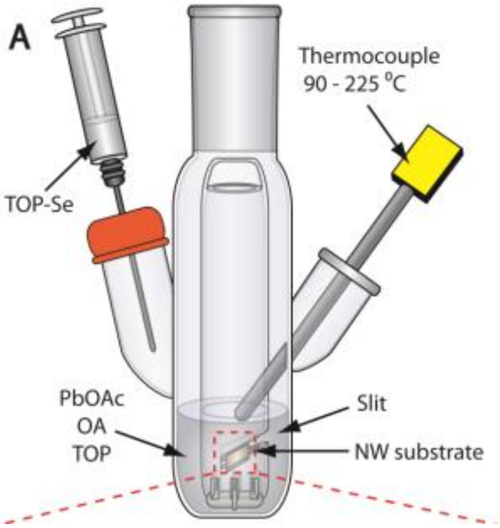

Figure 5.4. The glassware designed and utilized for this heterostructure synthesis.[24]

5.4.2 Structural Characterization

Typical transmission electron microscopy (TEM) and scanning transmission electron microscopy (STEM) images of PbSe QD–TiO_2 NR heterostructure are shown in Figure 5.5, clearly indicating the formation of PbSe QDs on TiO_2 NRs surface. Likewise, growth of PbSe QDs on other substrates (TiO_2 NPs on glass and TiO_2 NWs on titanium foil) has resulted in similar uniform QD coverage, as shown in STEM images in Figure 5.5c and 5.5d. The diameter of most PbSe QDs was in the range of 2.5 to 3 nm. All of them show a well-defined hemispherical shape, confirming these QDs are nucleated and grown directly on TiO_2 surface rather than attached onto TiO_2 after grown in solution. Figure 5.5e shows one representative EDX spectrum of one PbSe QD–TiO_2 NR heterostructure sample prepared on a TEM copper grid, further confirming the presence of both PbSe and TiO_2 component. The excess Pb to Se ratio is attributed to Se element gradually being melted in the strong electron beam during TEM focusing.[29]

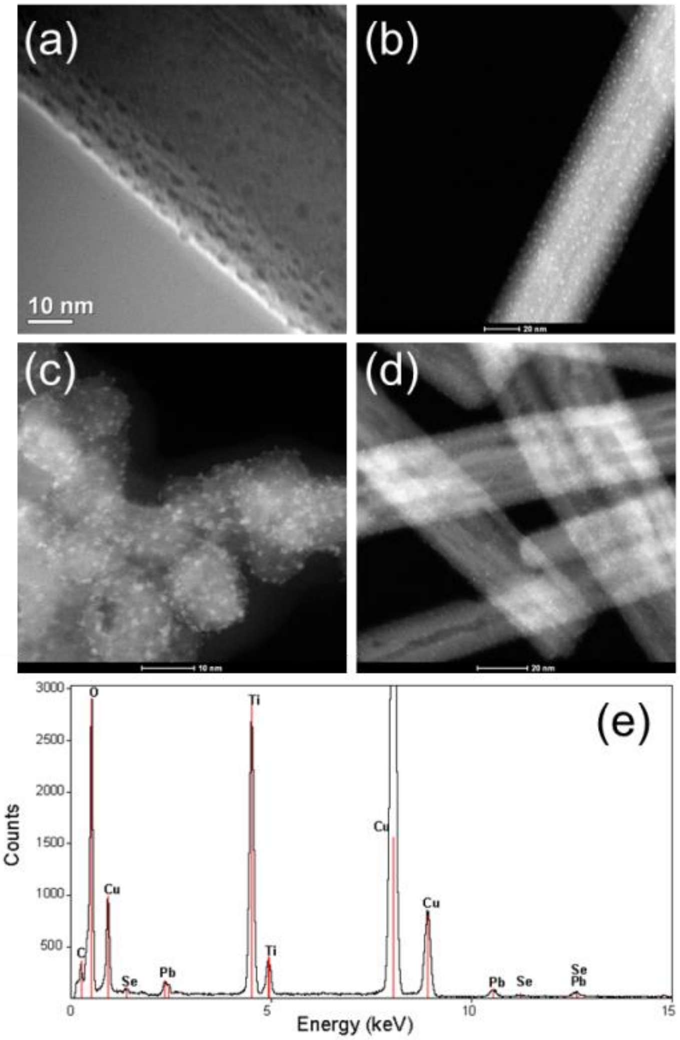

Figure 5.5. TEM and STEM images of PbSe–TiO_2 heterostructures: (a, b) PbSe QD–TiO_2 NR, (c) PbSe QD–TiO_2 NP, (d) PbSe QD–TiO_2 NW. (e) A representative EDX spectrum of PbSe QD–TiO_2 NR heterostructure.

HRTEM was carefully performed to examine the crystalline interface between the PbSe QDs and TiO_2 NRs. One representative image is shown in Figure 5.6. In the corresponding full fast Fourier transform (FFT) (Figure 5.6b), two sets of diffraction spots from PbSe and TiO_2 were revealed, respectively. FFTs of selected nonoverlapping regions of the PbSe QD and TiO_2 NR were also performed to deconvolute the individual contributions to FFT of the full image (Figure 5.6c and 5.6d), from which we can index the PbSe QD to be on the [110] zone axis, and the TiO_2 NR on the $[1\bar{1}0]$ zone axis. The simultaneous observation of the two zone axes for PbSe and TiO_2 crystal lattices means that these two crystallographic directions, [110] for PbSe and $[1\bar{1}0]$ for TiO_2, are aligned at the heterostructure interface. From the FFT of the full image, we also note that the PbSe $(\bar{1}11)$ and TiO_2 $(1\bar{1}0)$ diffraction spots are aligned collinearly from the origin, indicating these sets of lattice planes are nearly parallel and the heterointerface is formed by joining the PbSe $(\bar{1}11)$and TiO_2 $(1\bar{1}0)$ planes.

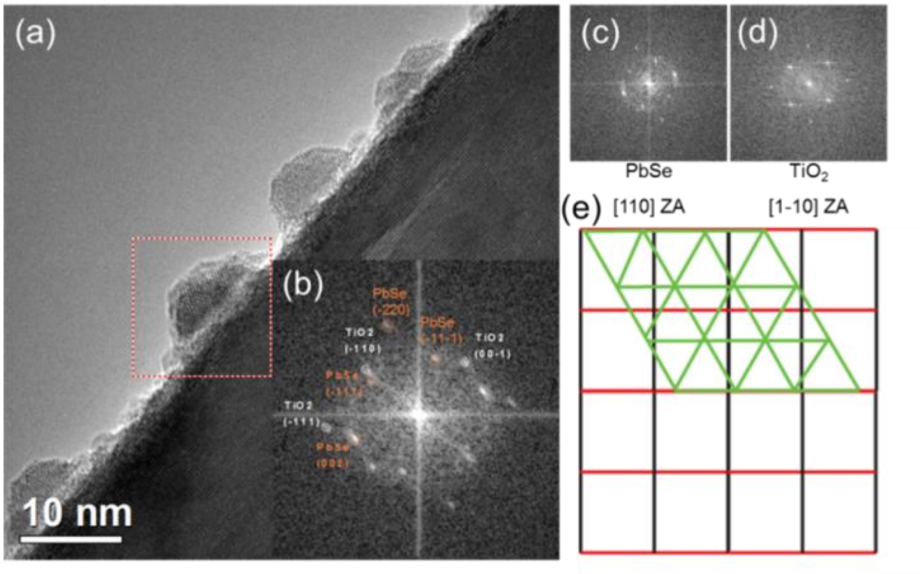

Figure 5.6. HRTEM image of PbSe QDs on the edge of a TiO_2 NR (a) with its corresponding indexed FFT (b) and FFTs for individual PbSe QD (c) and TiO_2 NR (d). (e) A schematic diagram illustrating this heteroepitaxial relationship between PbSe and TiO_2 with PbSe (220) planes shown in green, TiO_2 (110) planes in red, and TiO_2 (001) planes in black.

Table 5.1. A table summarizing the epitaxial lattice match parameters for the specific PbSe−TiO_2 heterojunction.

Lattice Planes	Lattice Spacing (nm)	Supercell (nm)	Percent Mismatch
$TiO_2\{110\}$	0.325	0.325×2=0.650	0.1%
PbSe{110}	0.217	0.217×3=0.651	
$TiO_2\{001\}$	0.296	0.296×5=1.480	1.3%
$PbSe\{1\bar{1}0\}$	0.250	0.250×5=1.500	

In order to calculate the mismatch between PbSe and TiO_2, a large supercell that satisfies the translational symmetry for both materials needs to be defined. The supercell at the epitaxial interface is shown in Figure 5.6d with the PbSe (220) planes shown in green, TiO_2 (110) planes in red and TiO_2 (001) planes in black. In the vertical direction, two (110) lattice spacings of TiO_2 only have a mismatch of 0.1% with three (110) lattice spacings of PbSe, forming the *a* direction of the supercell. In the horizontal direction, five (001) lattice spacings of TiO_2 and six $(1\bar{1}0)$ lattice spacings of PbSe have a mismatch of 1.3%. This will be the *b* direction of the supercell. The total supercell area is 0.962 nm^2 for PbSe and 0.976 nm^2 for TiO_2, with only a 1.5% mismatch. The supercell at the epitaxial interface is shown in Figure 5.6d with PbSe (220) planes shown in green, TiO_2 (110) planes in red, and TiO_2 (001) planes in black.

Interestingly, despite some other HRTEM images showing the same epitaxy, this is not the only heteroepitaxial relationship we found on this heterostructure sample. Two other possible epitaxial relationships have been confirmed with their HRTEM images and corresponding FFTs shown in Figure 5.7, demonstrating the ease of forming high-quality, epitaxial interfaces in these heterostructures prepared using this approach.

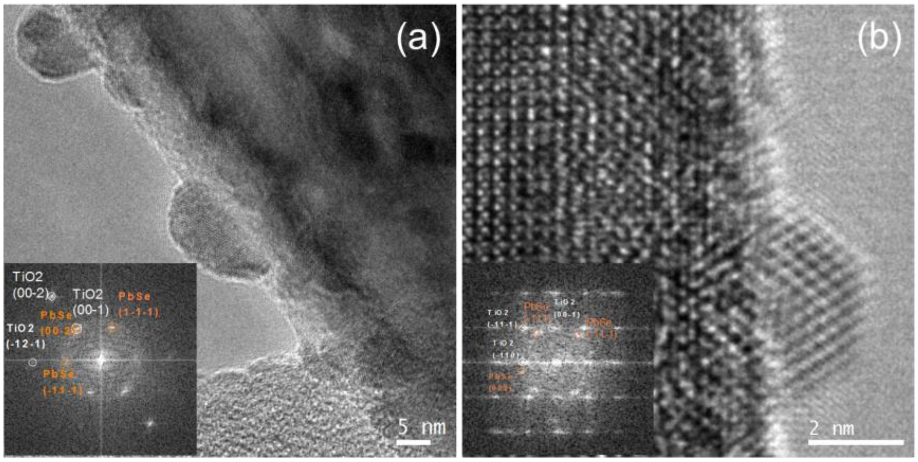

Figure 5.7. HRTEM images of PbSe QD-TiO_2 NR heterostructure.

5.4.3 Applicability on TiO_2 nanosheets

As demonstrated above, we have already synthesized epitaxial QDHs on TiO_2 rutile nanorods and TiO_2 anatase nanoparticles. With this ground work laid, we want to further improve the QDH system by replacing TiO_2 nanorod and nanoparticle with TiO_2 nanosheet. Based on theoretical studies, the {001} facets of anatase TiO_2 is much more reactive than the {101} facets, which is the thermodynamically more stable surface and the dominant surface in most synthetic and natural anatase crystals. There have been many reports recently synthesizing TiO_2 nanosheet with high percentage of (001) facets using a simple hydrothermal reaction.[15,30-34] They have shown such TiO_2 nanosheets demonstrate superior photocatalytic efficiency, far exceeding that of Degussa P25.[33] Also, based on one Brunauer–Emmett–Teller (BET) measurement,[15] 30-nm sized nanosheets showed a surface area of 122 m^2 g^{-1}, substantially higher than the 75 m^2 g^{-1} of 18-nm TiO_2 NPs. It is anticipated that higher surface area will leave more room for the grown of QDs, and the absorption of such QDHs will increase significantly as a result of the more QDs loading. Furthermore, the exposed (001) facets have higher ionic charge compared to the (101) facets,[35] which can help strengthen the attachment of QD, improve the quality of interface, and screen the electrons injected in the conduction band of the oxide,[34] all of which have led to better photovoltaic performance in solar energy conversion on several demonstrated heterostructure systems.[15,34]

We synthesized the TiO_2 anatase nanosheets using a simple hydrothermal reaction reported previously.[33] In a typical synthesis, 10 mL $Ti(OBu)_4$ (98%) and 0.8 mL hydrofluoric acid (47%) were mixed in a 150 mL Teflon autoclave, which was then kept at 180 °C for 24 h. The white powder obtained after reaction was separated by high-speed centrifugation and washed with ethanol and distilled water afterwards. TEM images showed these TiO_2 nanosheets have side length of 30–80 nm, and thickness of 6–8 nm, depending on specific reaction parameters (Figure

5.8). These as-prepared TiO_2 nanosheets can be deposited by spin coating (4000 rpm for 10 s) from a dilute aqueous solution to form a nanosheet TiO_2 layer on FTO or glass substrates, resulting in a nanosheet titania film with 300 ± 50 nm thickness[15], which can be further used for device fabrication or spectroscopy studies. While PbS quantum dot heterojunction solar cell has been fabricated using TiO_2 nanosheet,[15] to date there has been no work reporting epitaxial QD–TiO_2 nanosheet heterostructures.

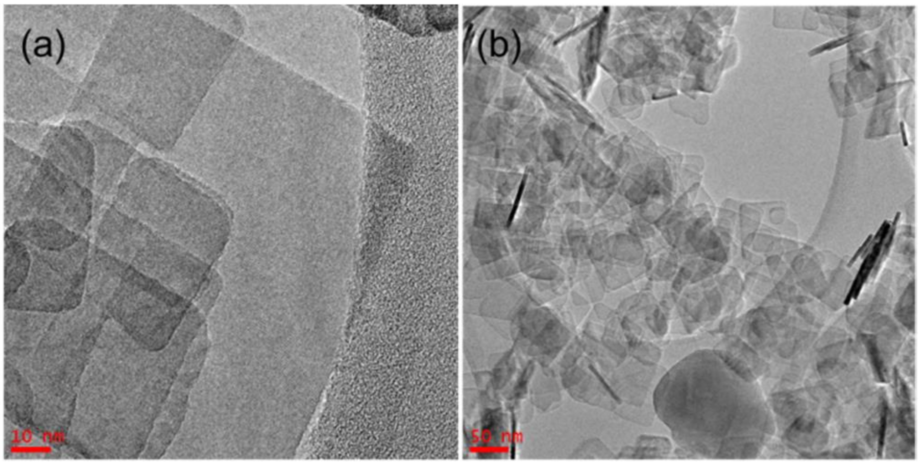

Figure 5.8. (A) High-magnification TEM image of an individual TiO_2 nanosheet synthesized at 180 °C using 5 mL of $Ti(OBu)_4$ and 0.6 mL of HF; the inset shows the corresponding SAED pattern (B) low-magnification TEM image of TiO_2 nanosheets.

Following the same dehydration pretreatment and synthesis procedure, we successfully extended this colloidal approach to TiO_2 nanosheets. The TiO_2 surface has been completely covered with epitaxial PbSe QDs. The high surface area, well-defined lattice planes, superior photocatalytic and photovoltaic performances of such materials should make them promising candidates for both spectroscopy characterization and device fabrication.

5.4.4 Investigation of growth mechanism

It is of great significance to tune PbSe QD sizes and their band gaps correspondingly in order to form a desired type II heterojunction and produce efficient charge transfer from PbSe QDs to TiO_2 materials. Thus, it is critical to understand how reaction parameters affect the size of PbSe QDs, and investigate the mechanism for the nucleation and growth of these heterostructures.

In the formation of heterogeneous systems, the total change in Gibbs free interface energy of adding a second material to a first material follows equation 1.[36]

$$\Delta \mathrm{G}_s = \gamma_1 - \gamma_2 + \gamma_{1,2}$$

γ_1 and γ_2 are the surface energies of material 1 and 2, and $\gamma_{1,2}$ is the interfacial energy of the two materials. The sign of Gibbs free energy change will dictate the tendency of the system to adopt a certain growth mode.[36,37] For PbSe–TiO_2 system, due to the large lattice-mismatch and significant strain between the two materials, it is expected it will follow a Vollmer-Weber growth mechanism, in which PbSe adopt the habit of a discontinuous islandlike domain as a means of minimizing of the overall interfacial area shared with TiO_2,[23] forming discrete quantum dots as shown in previous TEM and SEM images.

Based on this mechanism, we suspect the sizes of QD islands formed on surface should also be limited by the total change in Gibbs free energy, thus careful control of surface energy is critical in controlling the sizes of QDs. This can be verified in two aspects. First, the presence of organic ligands is known to be able to alter the surface energy of corresponding materials, thus we anticipate ligands play a significant role in controlling QD sizes.[23] Efforts are underway to verify this effect of ligands by utilizing different surfactants for QD synthesis, using ligands at different concentration and varying the ratio between different ligands. On the contrary, factors like precursor concentration, injection temperature, growth time do not have a big effect on surface energy.[23] Our results of varying these factors using PbSe QD−TiO_2 NR as an example have confirmed these parameters indeed do not have a great influence on the sizes of QDs. Based on our experiment, secondary injection also shows a dramatic increase on QD sizes and can effectively tune the size of QDs from 2.5 nm to 7 nm. Two representative SEM images before and after secondary injection were shown in Figure 5.9.

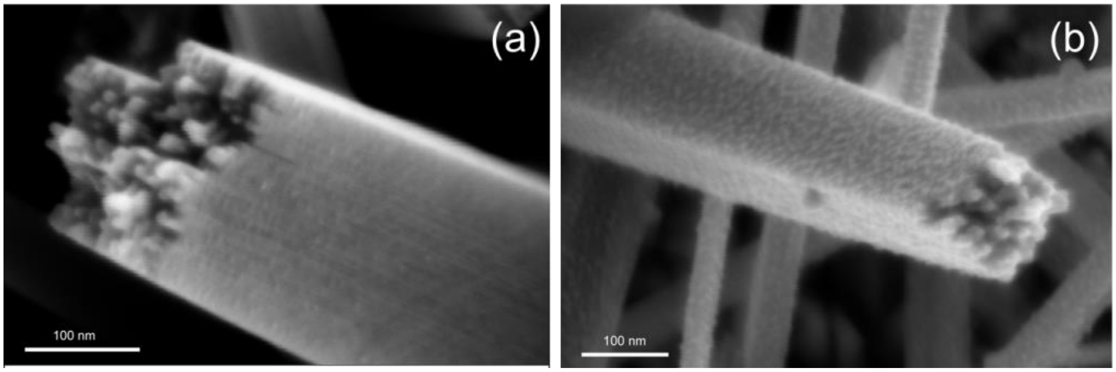

Figure 5.9. SEM images of PbSe QD-TiO_2 NR heterostructure prepared from single injection (left) and secondary injection (right).

Interestingly, when we try to extend our approach to cadmium chalcogenide, the synthesis did not work as well and easy as PbSe and PbS. Instead of growing QDs on TiO_2 surface, CdX precursors tend to homonucleate in solution to form CdX QDs. Additionally, despite several articles reporting epitaxial PbX−TiO_2 heterostructures,[2,22,23] there have been no reports on definitive epitaxial CdX−TiO_2 heterostructures to date. This difference between CdX and PbX has lead us to further investigate the mechanism controlling the competition between homonucleation of QDs in solution and heteronucleation of QDs onto TiO_2 surface. It is noted that heteronucleation requires less energy to initiate and thus lower injection temperature, while homonucleation usually takes place at higher temperature.[37] For CdX, the homonucleation process is very fast. Thus, at high injection temperature, the nucleation is suspected to be kinetically driven. Hence, the kinetically preferred homonucleation is dominant and few precursor monomers have the chance to diffuse onto substrate and nucleate on surface. In this case, it is anticipated that a lower injection temperature that suppresses homonucleation but sufficient for heteronuelcation is preferred for heterogeneous growth of QDs onto substrate. Whereas for PbX, the homonucleation process is not as fast, therefore the growth is more under thermodynamic control. Thus, even at high injection temperature, some precursors still have time to diffuse onto substrate and choose the thermodynamically favorable heteronucleation. Therefore, in this situation, we see a large quantity of PbX QDs nucleated on surface as well as PbX QDs nucleated in solution.

Two factors can be adjusted in future experiments to verify this hypothesis: injection temperature and growth rate of QDs. When adjusting injection temperature, it is expected that homonucleation dominates at high injection temperature, both heteronucleation and homonucleation contribute at medium temperature, and homonucleation is suppressed while heteronucleation is preferred at low temperature (temperature needs to be sufficient for heteronucleation). The preference of either heteronuelcation or homonucleation can be determined by checking the coverage of QDs on substrate surface. On the other side, we can also change the growth rate of QDs by using different synthetic approaches, as a means to control the competition between kinetically driven process and thermodynamically driven process. Based on our assumption, systems with fast growth rate of QDs will lead to more homonucleation at the same injection temperature compared to systems with slow growth rate. Assuming our hypothesis is correct, then careful adjustment and control of injection temperature and growth rate should make the synthesis of definitive epitaxial CdX-TiO_2 heterostructure possible.

5.4.5 Investigation of the charge transfer dynamics

With the successful synthesis of epitaxial quantum dot heterostructures on various substrates already demonstrated, we then focus on characterizing such heterostructures to study their charge transfer properties.

There are three primary types of charge-transfer mechanisms: quantum mechanical tunneling, where phase coherence is preserved during the transfer; tunneling between multiple potential wells, where coherence is lost in each well (when the charge resides in the potential well); and thermally activated incoherent hopping without phase coherence.[16,38,39]

Many factors could affect the mechanism and rate of charge transfer. Band energy alignment determines the driving force of transfer. Quality of interface and distance between the donor and acceptor materials also have a significant effect. It is worth noting that for coherent tunneling, charge transfer rate is exponentially dependent on separation distance. Therefore, it is expected that heterostructures with proper band energy alignment and high-quality, epitaxial interfaces have best charge separation.[37,40-42]

Optical properties of these epitaxial QDHs have been analyzed using PbSe QDs on TiO_2 NPs on glass substrate as an example (Figure 5.10). Due to the scattering of TiO_2 NPs, there is an inhomogeneous offset of the absorption curve in visible region as shown in the red curve in Figure 3. The increase in absorption (Figure 5.10a) for QDH compared to bare TiO_2 in the 400–800 nm region is attributed to the absorption of PbSe QDs (3 nm diameter). Interestingly, the 1S(e)–1S(h) excitonic peak could not be distinguished in the absorption spectra as commonly seen in the spectra of heterostructures containing QDs. Since our QDs have relatively narrow size distribution, this should be attributed to the ultrafast charge transfer from PbSe QDs to TiO_2, which has also been observed for some other QDH systems.[23,43] In order to compare epitaxial QDHs with QDHs made using other techniques, PbSe QD–TiO_2 QDHs prepared using mercaptopropionic acid (MPA) as a linker molecule and *via* direct QD adsorption were also fabricated on glass substrate. The STEM images revealed these linked and direct attached QDHs have slightly higher QD coverage. However, more QD clusters were observed in these QDHs in contrast to the uniformly distributed QDs in epitaxial QDHs. Because of the higher overall QD loading, these linked and direct adsorbed samples showed darker color and hence higher absorption (Figure 5.10b). Interestingly, excitonic peaks were clearly seen in these samples (Figure 5.10b, inset). Assuming the QD size distributions for linked, directly attached and epitaxial QDHs are all similar, this difference in excitonic peak suggests that difference in charge transfer rates for different QDHs: epitaxial QDHs have fastest charge transfer and hence suppressed excitonic peak. However, more conclusive evidence is needed, and the investigation using ultrafast transient spectroscopy and coherent multidimensional spectroscopy are underway to confirm epitaxial QDHs’ advantage in charge separation and charge transfer properties.

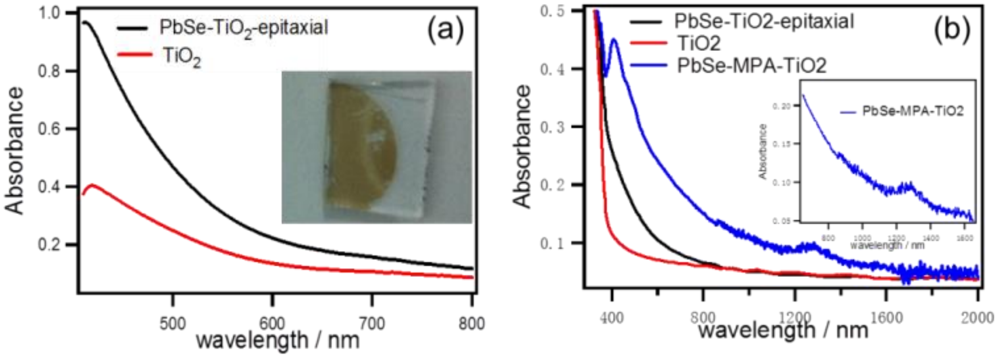

Figure 5.10. Absorption spectra of epitaxial and linked PbSe QD−TiO$_2$ quantum dot heterostructures.

5.5 Conclusion

In conclusion, epitaxial PbSe quantum dots–TiO_2 nanoscale heterostructures have been synthesized *via* a hot injection approach. QDHs synthesized using this approach showed good QD coverage and narrow QD size distribution. The heteroepitaxial interface has been characterized by HRTEM. The increase in absorption spectra is attributed to the absorption of QDs, and the direct lattice connection between the donor and acceptor materials is expected to allow faster charge transfer compared to QDHs connected *via* linker molecules.

5.6 References

(1) Brus, L. *J Phys Chem-Us* **1986**, *90*, 2555.

(2) Acharya, K. P.; Alabi, T. R.; Schmall, N.; Hewa-Kasakarage, N. N.; Kirsanova, M.; Nemchinov, A.; Khon, E.; Zamkov, M. *J Phys Chem C* **2009**, *113*, 19531.

(3) Kamat, P. V. *J Phys Chem C* **2008**, *112*, 18737.

(4) Matthews, J. W.; Blakeslee, A. E. *J Cryst Growth* **1974**, *27*, 118.

(5) Bierman, M. J.; Jin, S. *Energ Environ Sci* **2009**, *2*, 1050.

(6) Beard, M. C.; Midgett, A. G.; Law, M.; Semonin, O. E.; Ellingson, R. J.; Nozik, A. J. *Nano Lett* **2009**, *9*, 836.

(7) Luther, J. M.; Beard, M. C.; Song, Q.; Law, M.; Ellingson, R. J.; Nozik, A. J. *Nano Lett* **2007**, *7*, 1779.

(8) Sambur, J. B.; Novet, T.; Parkinson, B. A. *Science* **2010**, *330*, 63.

(9) Semonin, O. E.; Luther, J. M.; Choi, S.; Chen, H. Y.; Gao, J. B.; Nozik, A. J.; Beard, M. C. *Science* **2011**, *334*, 1530.

(10) Evans, C. M.; Guo, L.; Peterson, J. J.; Maccagnano-Zacher, S.; Krauss, T. D. *Nano Lett* **2008**, *8*, 2896.

(11) Kovalenko, M. V.; Talapin, D. V.; Loi, M. A.; Cordella, F.; Hesser, G.; Bodnarchuk, M. I.; Heiss, W. *Angew Chem Int Edit* **2008**, *47*, 3029.

(12) Du, H.; Chen, C. L.; Krishnan, R.; Krauss, T. D.; Harbold, J. M.; Wise, F. W.; Thomas, M. G.; Silcox, J. *Nano Lett* **2002**, *2*, 1321.

(13) Wise, F. W. *Accounts Chem Res* **2000**, *33*, 773.

(14) Lazzeri, M.; Vittadini, A.; Selloni, A. *Physical Review B* **2001**, *63*.

(15) Etgar, L.; Zhang, W.; Gabriel, S.; Hickey, S. G.; Nazeeruddin, M. K.; Eychmüller, A.; Liu, B.; Grätzel, M. *Advanced Materials* **2012**, *24*, 2202.

(16) Selinsky, R. S.; Ding, Q.; Faber, M. S.; Wright, J. C.; Jin, S. *Chem Soc Rev* **2012**.

(17) Wang, D. F.; Zhao, H. G.; Wu, N. Q.; El Khakani, M. A.; Ma, D. L. *J Phys Chem Lett* **2010**, *1*, 1030.

(18) Lawless, D.; Kapoor, S.; Meisel, D. *J. Phys. Chem.* **1995**, *99*, 10329.

(19) Robel, I.; Subramanian, V.; Kuno, M.; Kamat, P. V. *J Am Chem Soc* **2006**, *128*, 2385.

(20) Watson, D. F. *J Phys Chem Lett* **2010**, *1*, 2299.

(21) Sambur, J. B.; Riha, S. C.; Choi, D.; Parkinson, B. A. *Langmuir* **2010**, *26*, 4839.

(22) Acharya, K. P.; Hewa-Kasakarage, N. N.; Alabi, T. R.; Nemitz, I.; Khon, E.; Ullrich, B.; Anzenbacher, P.; Zamkov, M. *J Phys Chem C* **2010**, *114*, 12496.

(23) Acharya, K. P.; Khon, E.; O'Connor, T.; Nemitz, I.; Klinkova, A.; Khnayzer, R. S.; Anzenbacher, P.; Zamkov, M. *Acs Nano* **2011**, *5*, 9299.

(24) Selinsky, R. S.; Shin, S.; Lukowski, M. A.; Jin, S. *J. Phys. Chem. Lett* **2012**, *3*, 1649.

(25) Wehrenberg, B. L.; Wang, C. J.; Guyot-Sionnest, P. *J Phys Chem B* **2002**, *106*, 10634.

(26) Park, S.-H.; Kim, S.; Lee, D.-J.; Yun, S.; Khim, Z. G.; Kim, K.-B. *Journal of The Electrochemical Society* **2009**, *156*, K181.

(27) Leschkies, K. S.; Divakar, R.; Basu, J.; Enache-Pommer, E.; Boercker, J. E.; Carter, C. B.; Kortshagen, U. R.; Norris, D. J.; Aydil, E. S. *Nano Lett* **2007**, *7*, 1793.

(28) Yates Jr, J. T. *Surf. Sci.* **2009**, *603*, 1605.

(29) Lee, H.; Leventis, H. C.; Moon, S. J.; Chen, P.; Ito, S.; Haque, S. A.; Torres, T.; Nuesch, F.; Geiger, T.; Zakeeruddin, S. M.; Gratzel, M.; Nazeeruddin, M. K. *Adv Funct Mater* **2009**, *19*, 2735.

(30) Yang, H. G.; Sun, C. H.; Qiao, S. Z.; Zou, J.; Liu, G.; Smith, S. C.; Cheng, H. M.; Lu, G. Q. *Nature* **2008**, *453*, 638.

(31) Wang, X.; Liu, G.; Wang, L.; Pan, J.; Lu, G. Q.; Cheng, H.-M. *Journal of Materials Chemistry* **2011**, *21*, 869.

(32) Qi, L.; Yu, J.; Jaroniec, M. *Physical Chemistry Chemical Physics* **2011**, *13*, 8915.

(33) Han X; Kuang Q; Jin M; Xie Z; L, Z. *J Am Chem Soc* **2009**, *131*, 3152.

(34) Etgar, L.; Gao, P.; Xue, Z.; Peng, Q.; Chandiran, A. K.; Liu, B.; Nazeeruddin, M. K.; Gratzel, M. *J Am Chem Soc* **2012**, *134*, 17396.

(35) Kavan, L.; Gratzel, M.; Gilbert, S. E.; Klemenz, C.; Scheel, H. J. *J Am Chem Soc* **1996**, *118*, 6716.

(36) Markov, I. V. *World Scientific, Singapore* **2003**.

(37) Carbone, L.; Cozzoli, P. D. *Nano Today* **2010**, *5*, 449.

(38) Adams, D. M.; Brus, L.; Chidsey, C. E. D.; Creager, S.; Creutz, C.; Kagan, C. R.; Kamat, P. V.; Lieberman, M.; Lindsay, S.; Marcus, R. A.; Metzger, R. M.; Michel-Beyerle, M. E.; Miller, J. R.; Newton, M. D.; Rolison, D. R.; Sankey, O.; Schanze, K. S.; Yardley, J.; Zhu, X. Y. *J Phys Chem B* **2003**, *107*, 6668.

(39) McCreery, R. L. *Chem Mater* **2004**, *16*, 4477.

(40) Mieszawska, A. J.; Jalilian, R.; Sumanasekera, G. U.; Zamborini, F. P. *Small* **2007**, *3*, 722.

(41) Zur, A.; Mcgill, T. C. *J Appl Phys* **1984**, *55*, 378.

(42) Cozzoli, P. D.; Pellegrino, T.; Manna, L. *Chem Soc Rev* **2006**, *35*, 1195.

(43) Yang, Y.; Rodriguez-Cordoba, W.; Xiang, X.; Lian, T. Q. *Nano Lett* **2012**, *12*, 303.

(44) Kongkanand, A.; Tvrdy, K.; Takechi, K.; Kuno, M.; Kamat, P. V. *J Am Chem Soc* **2008**, *130*, 4007.

(45) Robel, I.; Subramanian, V.; Kuno, M.; Kamat, P. V. *J Am Chem Soc* **2006**, *128*, 2385.

(46) Harel, E.; Engel, G. S. *P Natl Acad Sci USA* **2012**, *109*, 706.

(47) Yurs, L. A.; Block, S. B.; Pakoulev, A. V.; Selinsky, R. S.; Jin, S.; Wright, J. *J Phys Chem C* **2012**, *116*, 5546.

(48) Kronik, L.; Shapira, Y. *Surf Sci Rep* **1999**, *37*, 1.

Appendix 1

Supporting Information for

Chapter 2

Efficient Photoelectrochemical Hydrogen Generation Using Heterostructures of Si and Chemically Exfoliated Metallic MoS_2*

A1.1 Fabrication of photoelectrodes.

Photoelectrodes of both bare and MoS_2-covered Si were fabricated following procedures reported. Briefly, the back side of the Si substrates with a resistivity of 1-2.5 Ω-cm (p-type, B doped, (100) orientation, prime grade, 525 µm thickness) was first scratched with a diamond scribe, then an ohmic back contact was formed by embedding a coiled Cu wire in a Ga/In eutectic mixture (Aldrich) onto the scratched Si surface. Silver paint (Ted Pella) was then used to affix the Cu wire. After drying, the Cu lead was passed into a glass tube (diameter 2 mm), and the Si electrode and Cu wire were encased in Hysol 9460 epoxy. The final exposed electrode area was defined by the epoxy and the geometrical area was determined using a calibrated digital image and ImageJ. All photoelectrodes were etched in aqueous buffered HF solution (Buffer HF Improved, Transene Inc.) for 30 seconds to remove the native silicon oxide on the surface prior to measurement.

---

* This chapter was originally published as the supporting information in *J. Am. Chem. Soc.* **2014**, *136*, 8504. It was prepared in collaboration with Fei Meng, Caroline R. English, Miguel Cabán-Acevedo, Melinda J. Shearer, Dong Liang, Andrew S. Daniel, Robert J. Hamers, and Song Jin* before being adapted here.

A1.2 Fabrication of MoS_2/Si solid-state diode.

A solid-state diode was fabricated on the CVD grown MoS_2/Si heterostructure. Two front contacts on MoS_2 were made using e-beam-evaporated 100 nm Ni, and then annealed at 400 °C in 100 sccm Ar, 10 sccm H_2 for 1 h. Two back contacts on Si were made using silver paste. I-V measurements were made with a home-built transport setup on a Cascade probe station. I-V curves were taken between the two front Ni contacts, between the two back Ag contacts, and then between the front and back contact with or without illumination (using the light from the microscope light source).

A1.3 Hydrogen measurements.

To determine the Faradaic efficiency of the photoelectrochemical cell, we measured the amount of generated H_2 using gas chromatography (GC). A chronoampometry test was conducted on a CVD grown 1T-MoS_2/Si photocathode at −0.1 V vs RHE under simulated 1 sun irradiation for 1 h with no H_2 bubbling. In the sealed cell, a syringe was used to transfer 500 μL gas from the headspace to a gas chromatography instrument (SRI Instruments) every 20 minutes. The detected H2 concentration was then used to calculate the total amount of H2 generated in the cell. The total amount of charge Q(C) passed through the cell was calculated by integrating the measured current over time. Faradaic efficiency was then calculated by comparing the theoretical H2 amount with GC-detected H2 amount.

A1.4 Time resolved surface photoresponse measurements (TR-SPR).

The TR-SPR measurements was conducted in 0.5 M sulfuric acid using a capacitor-like setup, in which the sample and a platinum mesh sense electrode separated using Teflon spacers

(127 μm thick) were assembled into a home-made cell holder. In this apparatus, the transient charge separation resulting for pulsed optical excitation induces a capacitive displacement current that is dropped across the 50 ohm input impedance of an amplifier. Optical excitation was achieve using 3 ns pulses with 0.1 mJ/pulse generated by a tunable laser (NT340, EKSPLA, Inc., Vilnius, Lithuania), which illuminated the samples through the sense electrode. A preamplifier (Model TA2000B-1, FAST ComTec GmbH, Oberhaching/München, Germany) with 50-Ω input and output impedances, 1.5 GHz bandwidth, and 10x voltage gain was used to amplify the response, which was then recorded using a digital oscilloscope (Model DSO9404A, Agilent, Inc., Santa Clara, CA). A photocurrent is produced from this capacitive measurement, and the photocurrent is then integrated over time to calculate the total charge. In the biexponential fitting equation $SPR(t) = y_0 + A_1e^{-\frac{1}{\tau_1}t} + A_2e^{-\frac{1}{\tau_2}t}$), y_0 = y offset, A_1 = amplitude 1, A_2 = amplitude 2, τ_1 = decay constant 1 for the carrier lifetime, τ_2 = decay constant 2 for the carrier lifetime.

A1.5 Time resolved microwave conductivity measurements (TRMC).

The TRMC measurements were conducted by illuminating the samples at 340 nm using a 3 ns pulse tunable laser (NT340, EKSPLA, Inc., Vilnius, Lithuania) at < 1 mW power while microwaves were passed through the back of the sample located at the open end of a waveguide via a gunn diode (Ducommun Inc., Carson, CA) at +5.5 V bias and 24 GHz frequency. The reflected signal is directed onto an HP K422C microwave detector and measured after passing through an 80x operational amplifier (TA2000B-3, ComTec GmbH, Oberhaching/Munchen, Germany) by a digital oscilloscope (Model DSO9404A, Agilent, Inc., Santa Clara, CA). Microwaves are reflected proportionally based on the number of charge carriers produced within the sample, and thus a simple exponential fit is applied to determine carrier lifetime. The fit equation is $TRMC (t) = y0 + Ae-1/\tau \times t$, where yo = y offset, A = amplitude, and τ = decay constant for carrier lifetime.

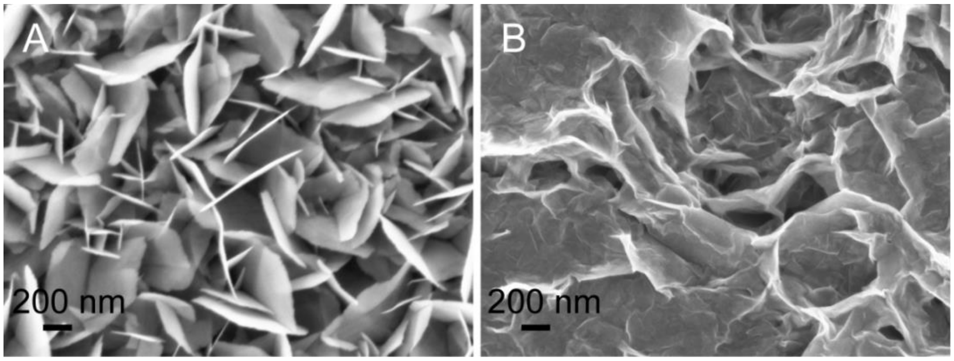

Figure A1.1. Top-down SEM images of (A) as-grown 2H-MoS$_2$ and (B) chemically exfoliated 1T-MoS$_2$ nanostructures used for dropcasting experiments.

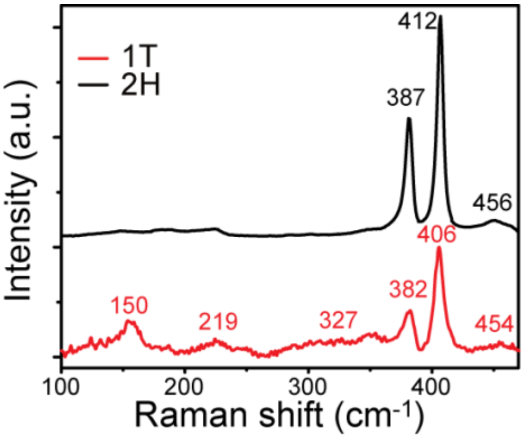

Figure A1.2. Raman spectra of as-grown 2H-MoS$_2$ (black curve) and chemically exfoliated 1T-MoS$_2$ (red curve) used for dropcasting experiments. The Raman shifts agree well with our previous observation.

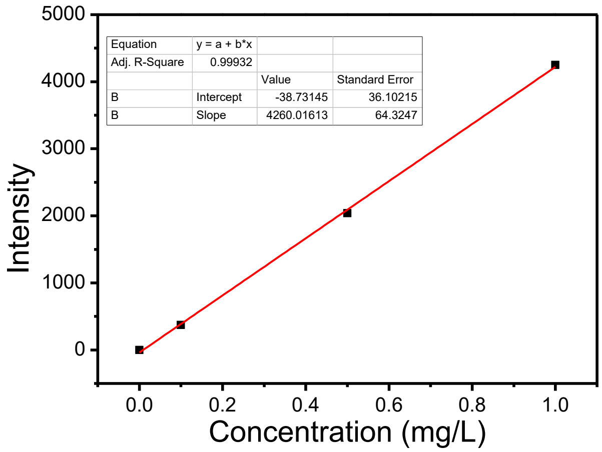

$$Intensity = 4260 \times Concentration\ (mg/L) - 38.73$$

Figure A1.3. Calibration curve of emission intensity as a function of the concentration of Mo standard solutions measured by ICP-AES.

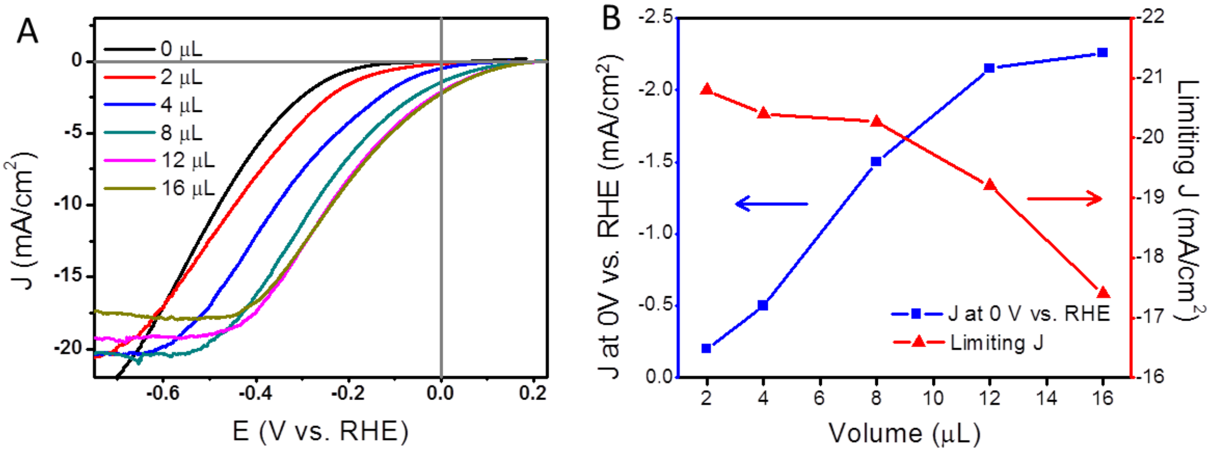

Figure A1.4. Photoelectrochemical characterization of *p*-Si photocathodes with dropcasted 2H-MoS_2 suspensions. (A) J−E curve of a Si photocathode with different volume of 2H-MoS_2 suspensions measured under simulated 1 sun irradiation in 0.5 M sulfuric acid. (B) The relationship of the current density at 0 V *vs* RHE and the limiting current density as a function of different volume of 2H-MoS_2 suspensions applied.

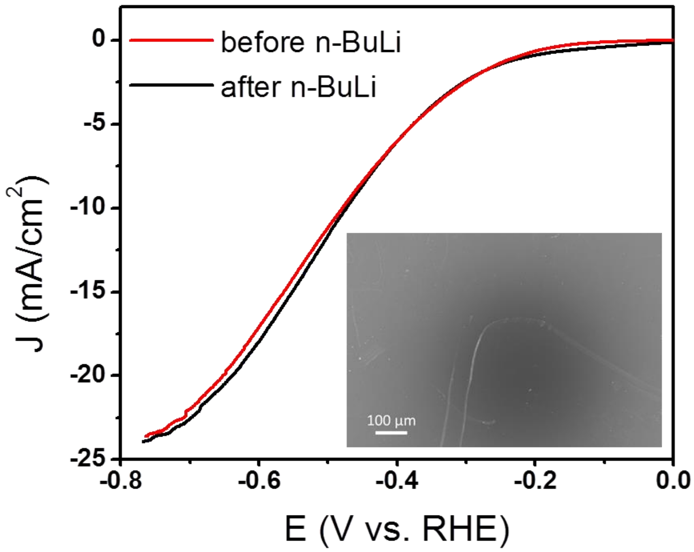

Figure A1.5. J−E curve of a Si photocathode before (red) and after (black) *n*-butyl lithium treatment showing that this treatment causes no effect to the photoelectrochemical properties of silicon. SEM image of a silicon piece after *n*-butyl lithium treatment is shown in the inset.

Appendix 2

Supporting Information for

Chapter 3

Designing Efficient Solar-Driven Hydrogen Evolution Photocathodes Using Semi-Transparent MoQ_xCl_y (Q=S, Se) Catalysts on Si Micropyramids[*]

A2.1 Fabrication of photocathodes.

Si photocathodes were fabricated following reported procedures. Briefly, the back side of the Si substrates was first scratched with a diamond scribe, and then a coiled Cu wire was embedded in a Ga/In eutectic mixture (Aldrich) onto the scratched Si surface, forming an ohmic back contact. Silver paint (Ted Pella) was then used to affix the Cu wire. After drying, the Cu lead was passed into a 2 mm diameter glass tube, and the Si electrode and Cu wire were then encased in Hysol 9460 epoxy. Calibrated digital images and ImageJ were used to determine the geometrical area of the exposed electrode surface defined by epoxy. Planar p-type Si photocathodes were etched in aqueous buffered HF solution (Buffer HF Improved, Transene Inc.) for 30 seconds and n^+pp^+ Si MPs photocathodes were etched for 1-5 seconds to remove the native silicon oxide on the

---

[*] This chapter was originally published as the supporting information in *Advanced Materials* **2015**, *27*, 6511. It was prepared in collaboration with Jianyuan Zhai, Miguel Cabán-Acevedo, Melinda J. Shearer, Linsen Li, Hung-Chih Chang, Meng-Lin Tsai, Dewei Ma, Xingwang Zhang, Robert J. Hamers, Jr-Hau He, Song Jin* before being adapted here.

surface prior to measurements.

A2.2 Hydrogen Measurement.

The amount of generated H_2 was detected using gas chromatography-mass spectrometer (GC-MS). Both MoS_xCl_y/Si MP and $MoSe_xCl_y$/Si MP photocathodes were illuminated at 0 V versus RHE under simulated 1 Sun irradiation for more than 1 h with no H_2 bubbling. A syringe was used to periodically remove 500 μL from the headspace of a sealed cell, and then injected into a gas chromatography-mass spectrometer (GCMS-QP2010 Ultra, Shimadzu Scientific Instruments). The total amount of H_2 generated in the cell was then calculated based on the detected H_2 amount in the GCMS measurement. The total amount of charge Q(C) passed through the cell was calculated by integrating the measured current over time.

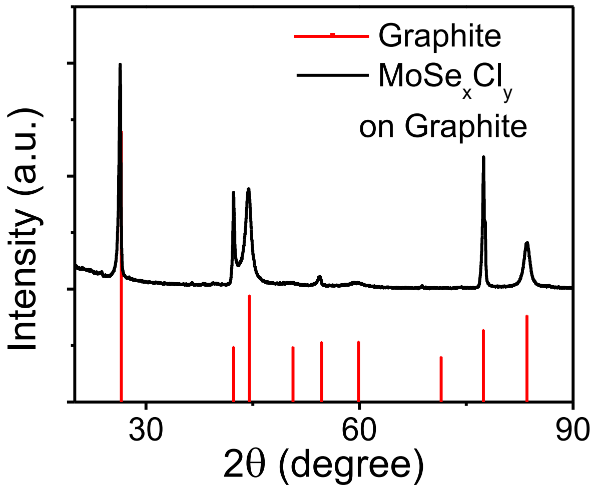

Figure A2.1. X-ray diffraction pattern of MoSe$_x$Cl$_y$ film on graphite substrate, in comparison with the reference diffraction pattern for graphite. Only diffraction peaks from graphite were observed, showing the deposited MoSe$_x$Cl$_y$ is amorphous.

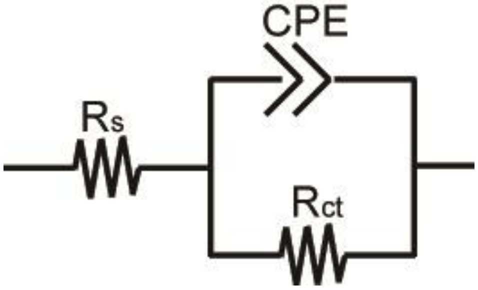

Figure A2.2. The simplified Randles equivalent circuit used to fit the arc in EIS spectra (Figure 1d in the main text), which consists of a resistor (R_s) in series with a parallel arrangement of a resistor (R_{ct}) and a constant phase element (CPE).

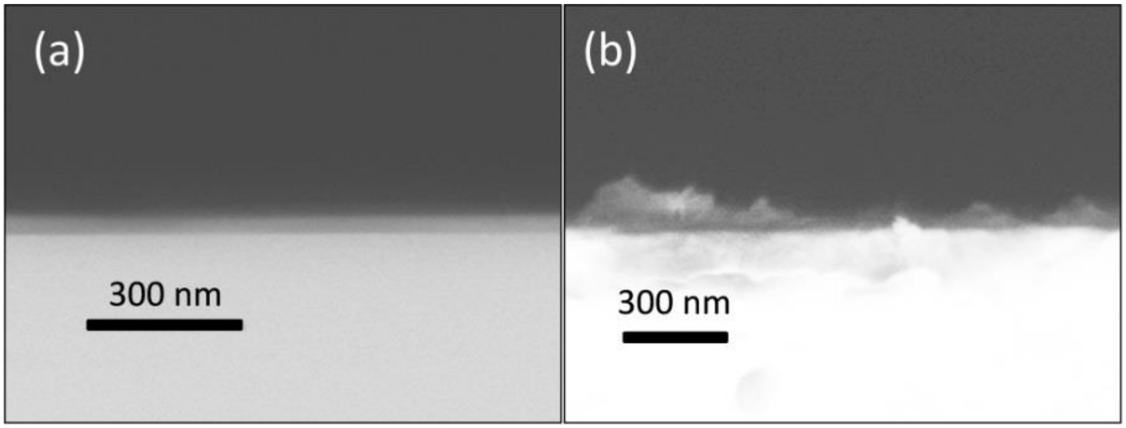

Figure A2.3. Cross-sectional SEM images of MoS_xCl_y (a) and $MoSe_xCl_y$ (b) deposited on planar p-type Si substrates.

Appendix 3

Supporting Information for

Chapter 4

Basal Plane Ligand Functionalization on Semiconducting 2H-MoS_2 Monolayers[*]

A3.1 Synthesis of PbSe quantum dots

The synthesis of PbSe quantum dots is modified from an established synthesis. Trioctylphosphine (TOP, 90%), 90 % oleic acid (OA), ≥ 99 % diphenyl ether (DiPE), ≥ 99 % lead (II) acetate PbOAc, and 99.99 % selenium powder were purchased from Sigma Aldrich and used without further purification. The 1 M trioctylphosphine-selenium complex (TOP-Se) was prepared in advance.

In a three-necked flask equipped with a septa and a thermocouple, 0.325 g PbOAc, 0.85 mL OA, 6 mL DiPE, and 4 mL TOP were heated to 85 °C under vacuum for 30 min to form the lead oleate precursor solution. This solution was heated to the desired injection temperature (125-130 °C) under nitrogen. When the solution reaches the desired temperature, 0.85 mL of 1 M TOP-Se solution (prepared in a glove box under nitrogen) was rapidly injected into the reaction mixture and the temperature was maintained for 2 min. Approximately 20 mL of anhydrous ethanol was then injected to rapidly cool the reaction. The PbSe QD solution was purified four times by

---

[*] This appendix was prepared as the supporting information for publication in collaboration with Kyle J. Czech, Jianyuan Zhai, Yuzhou Zhao, Robert J. Hamers, John C. Wright and Song Jin* before being adapted here.

precipitation and centrifugation with ethanol, and then kept in carbon tetrachloride in glove box till further use.

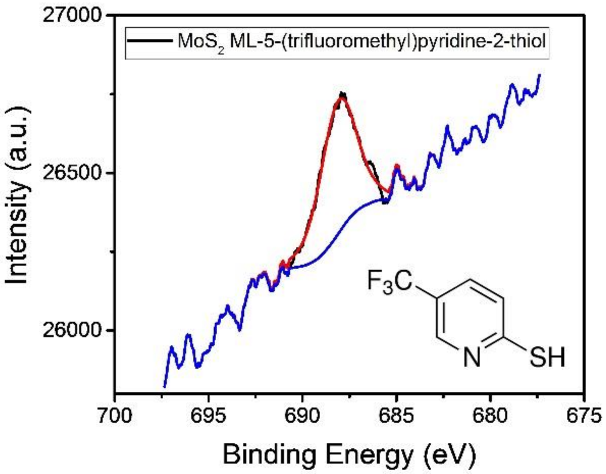

Figure A3.1. High-resolution XPS of F1s region for 5-(trifluoromethyl)pyridine-2-thiol functionalized CVD grown MoS$_2$ monolayer.

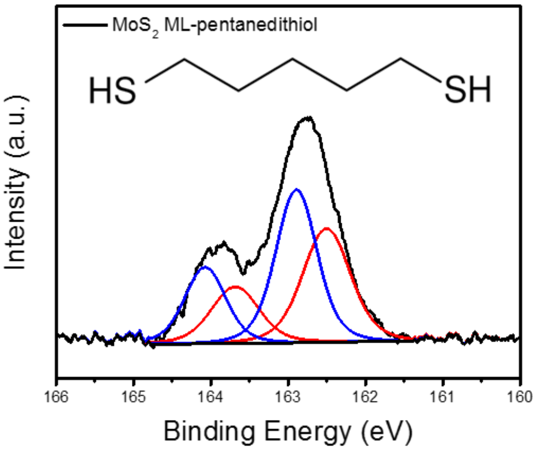

Figure A3.2. High-resolution XPS of S2p region for 1,5-pentanedithiol functionalized CVD grown MoS$_2$ monolayer.

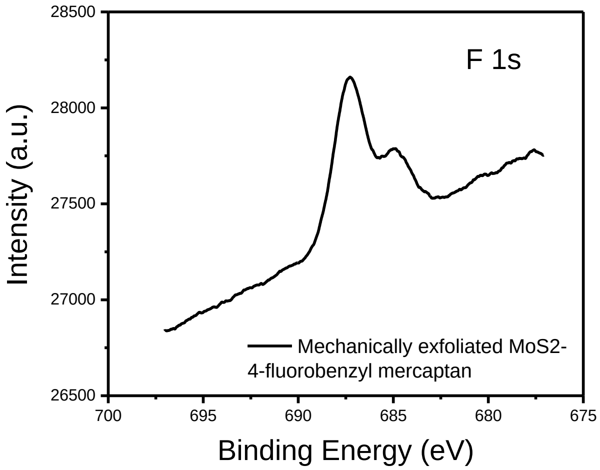

Figure A3.3. High-resolution XPS of F1s region for 4-fluorobenzyl mercaptan functionalized mechanically exfoliated single- and multilayer MoS_2.

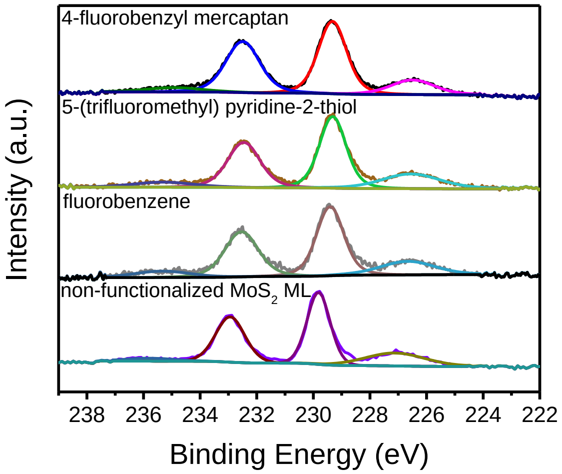

Figure A3.4. High-resolution XPS of Mo3d region for 4-fluorobenzyl mercaptan, 5-(trifluoromethyl)pyridine-2-thiol and fluorobenzene functionalized CVD grown MoS_2 monolayer, in comparison with non-functionalized MoS_2 monolayer.

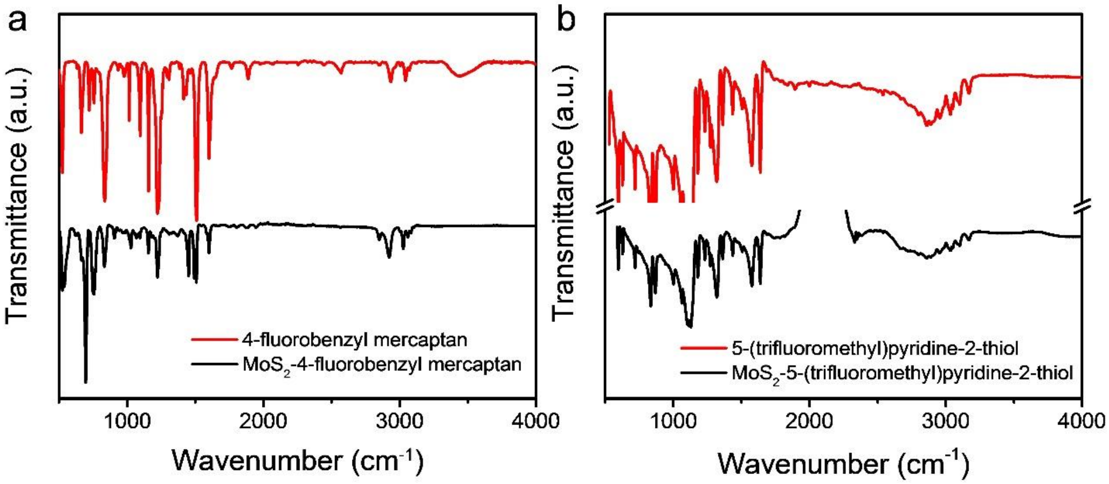

Figure A3.5. FTIR spectra of (a) 4-fluorobenzyl mercaptan and (b) 5-(trifluoromethyl)pyridine-2-thiol functionalized CVD grown MoS_2 nanoflowers grown on graphite substrate (black). The free 4-fluorobenzyl mercaptan and 5-(trifluoromethyl)pyridine-2-thiol ligands are shown in the red curves.